2017-12-06

Study on Ultra Wideband Spectral Response and Efficient Hot Electron Detection using Plasmon Field Effect Transistor

Seongman Cho
University of Miami, choseongman0422@hotmail.com

UNIVERSITY OF MIAMI

STUDY ON ULTRA WIDEBAND SPECTRAL RESPONSE AND EFFICIENT HOT ELECTRON DETECTION USING PLASMON FIELD EFFECT TRANSISTOR

By

Seongman Cho

A DISSERTATION

Submitted to the Faculty
of the University of Miami
in partial fulfillment of the requirements for
the degree of Doctor of Philosophy

Coral Gables, Florida

December 2017

UNIVERSITY OF MIAMI

A dissertation submitted in partial fulfillment of
the requirements for the degree of
Doctor of Philosophy

STUDY ON ULTRA WIDEBAND SPECTRAL RESPONSE AND EFFICIENT HOT ELECTRON DETECTION USING PLASMON FIELD EFFECT TRANSISTOR

Seongman Cho

Approved:

_____ Sung Jin Kim, Ph.D. Associate Professor of Electrical and Computer Engineering	_____ Mei-Ling Shyu, Ph.D. Professor of Electrical and Computer Engineering
_____ Michael Wang, Ph.D. Professor of Electrical and Computer Engineering	_____ Weizhao Zhao, Ph.D. Professor of Biomedical Engineering
_____ Ashutosh Agarwal, Ph.D. Assistant Professor of Biomedical Engineering	_____ Guillermo Prado, Ph.D. Dean of the Graduate School

CHO, SEONGMAN (Ph.D., Electrical and Computer Engineering)

Study on Ultra Wideband Spectral Response and Efficient Hot Electron Detection using Plasmon Field Effect Transistor. (December 2017)

Abstract of a dissertation at the University of Miami.

Dissertation supervised by Professor Sung Jin Kim.
No. of pages in text. (136)

Surface plasmons, collective charge density oscillation of conduction electrons in a nanostructured metal, has attracted considerable attention due to their unique optical properties in the past decade. Plasmonics is the study of the interactions between light and metals, specifically between the electromagnetic field and free electrons in metals. Plasmonics devices possess the advantages of both electronic devices and optical devices for tackling important issues such as operating speed and integration capability. Thus, plasmonics has been an important research area rapidly impacting every facet of optics and photonics.

We reported a new device structure named the plasmon field effect transistor based on a thin film transistor with metal nanostructures incorporated in it. Plasmon-induced hot electrons can overcome the Schottky barrier between the thin film and the metal because they have enough kinetic energy. The plasmon-induced hot electrons transferred from the nanostructured metal to the semiconductor improve drain current due to the increased conductivity of the electron channel generated at the bottom of the semiconductor or the hot electrons transported to the electron channel. We have observed a promising quantum tunneling based hot electron detection and an internal field (gate bias) assisted hot electron

collection. These are the key working principles to extend the detection wavelength up to far IR frequency using the plasmon field effect transistor.

The objective of this research is to explore the physics that enables the efficient collection of plasmonically induced hot electrons and study the ultra-wideband spectral response through quantum tunneling for low energy hot electrons from a variety of metal nanostructures using the plasmon field effect transistor. We investigated the efficiency of the plasmon field effect transistor with different positions of plasmonic nanostructured metal on the semiconductor, which either fabricates the nanostructures close to the Source or fabricates them close to the Drain. When the nanostructures are positioned near the source they exhibit more spectral response than when positioned close to the drain. Device design should therefore look to increase the efficiency of hot electron collection due to the gradient of the electric field seen by induced hot electrons depending on the distance between the drain and the source.

We studied how the gold nanoparticles are self-assembled and how different gold film thicknesses, annealing time, and temperature for a thermal reflow method affect self-assembly. The scanning electron microscope images of the gold nanostructure show that the size distribution and density of the gold NPs varied depending on the gold film thickness. Self-assembled gold nanostructures using the thermal reflow method and their spectral response including the efficiency are influenced by the temperature, the annealing time, the film thickness and the surface profile of the substrate. We also found that the shape and size of gold nanostructures are strongly related with the surface roughness.

Our study provided important information about the optimized device structure that enables maximized use of the generated hot electrons through plasmonic absorption. For

detection of IR wavelengths, plasmonic nanostructures of only a few hundred nanometers are needed. To fabricate gold nanostructures for a tailored plasmonic absorption, we used an electron beam lithography (EBL) method. We changed the metal, surrounding material, metal thickness, metal size, and metal shape to increase the plasmonic absorption peak. Also, the fabrication process was optimized to convert optical signals to electrical signals for an ultra-wide spectral response (400nm - 1.6μm). The research will facilitate the successful development of next-generation plasmonic electronics and will lead to the development of low-cost imaging devices with a detection limit up to THz frequency, useful for many military and security applications.

Thanks to Almighty God for giving me strength and wisdom

to understand, learn, and complete this study.

To my loving wife Yeonghui
and
my sons Wanhui and Unghui

ACKNOWLEDGEMENTS

I would like to express my deepest gratitude to my advisor, Dr. Sung Jin Kim, for his meticulous guidance, support, and help in every aspect of my doctorate studies. His professionalism, diligence, and mentoring skills are exceptional. I would also like to thank my committee members: Dr. Michael Wang, Dr. Weizhao Zhao, Dr. Mei-Ling Shyu, and Dr. Ashutosh Agarwal. Their professional knowledge, thoughtful feedback, and sincere advice were influential and essential for the completion of this study.

My sincere appreciation goes to Dr. Jaesun Lee, Dr. Joe Nabity, Dr. Neal Ricks, and Dr. Kevin Luongo who kindly taught me the fabrication techniques. In addition, my special expression of gratitude extends to my friends and colleagues in the program, Mark Andrew Ciappesoni, Dr. Young Hun Paik, Dr. Hossein Shokri, Dr. Hui Lu, Dr. Kai Shen, Dr. Guo Min Jiang, Dr. Alperen Toprak, Dr. Sukru Senveli, Sarfaraz Beig, Randil Gajasinghe, Yilin Yan, Yagmur Yildirim, Da Zhang for their help over the years.

This dissertation would not have been possible without the dedication of my family and relatives. They were always supporting me and encouraging me with their best wishes. Especially, my parents' unconditional support and love during this entire journey were unwavering. I wish to express my utmost gratitude and love to my wife, Yeonghui Lee, for her tremendous support, trust and prayer. She was always there to cheer me up and stood by me through the good and bad times. I would also like to thank my father-in-law and mother-in-law from the bottom of my heart for giving me their beautiful daughter.

I am very thankful to all the members in Miami Onnuri Church and Areumdown Church for their endless prayers and encouragement. A very special thanks to Kyung-min Na, Sang-un Joo and their families.

TABLE OF CONTENTS

LIST OF FIGURES

Chapter 1: INTRODUCTION

Gold and Silver have been important materials throughout history [1]. The interest in the Coinage metals was attributable to their ability to reflect light in the past. However, the noble metals exhibit high absorption characteristic because of the electrons' transition between electronic bands at higher frequencies [2, 3]. Also, with recent advances in optical technology and nanotechnology, these metals have been widely used in plasmonics due to their unique optical properties as nanoscale structures [4]. Plasmonics is the study of the interactions between light and metals, specifically between electromagnetic fields and free electrons in metals. Free electrons in metals are excited by the electric component of light [5]. There is a specific photon energy, corresponding to a specific wavelength, which is absorbed, excitng the electrons in the metal causing them to resonate. The absorbance is also highly sensitive to the refractive indices of the host matrix and the metal nanostructure. The plasmon-induced free electrons are referred to as hot carriers that are not in thermal equilibrium, and have larger energies than electrons thermal excited at ambient temperatures [6]. The plasmon effect can be manipulated and controlled through the careful design of metallic nanostructures [7-10].

Thus, plasmonics has been an important research area rapidly impacting every facet of optics and photonics. Recent improvements on fabrication techniques to create well-controlled nanostructures also contributed to a rapid development of plasmonic applications, such as meta-materials [11, 12], nonlinear optics [11], photovoltaic devices [13, 14], biomedical sensors [15, 16], medical therapies [17] and spectroscopy [18]. For plasmonic device technology, it is important to convert optical signals to electrical signals or vice versa. Recently, there have been demonstrations of plasmon resonance detection

using a graphene based device [19, 20] and Schottky junction detector structures in visible and near infrared spectra [21-23]. While there were successful demonstrations of plasmonic energy conversion to electric signals, those approaches face challenges due to low quantum efficiency and immature device technology.

We reported a new efficient device structure named a plasmon field effect transistor (plasmon FET) based on a thin film transistor with metal nanostructures incorporated on it. Plasmon-induced hot electrons can overcome the Schottky barrier between the thin film and the metal because they have enough kinetic energy. The plasmon-induced hot electrons transferred from the nanostructured metal to the semiconductor improve the drain current due to the increased conductivity of the electron channel generated at the bottom of the semiconductor or the hot electrons transported through the electron channel. Using the plasmon field effect transistor, we can detect visible wavelength from 510 to 560 nm. One of the fascinating properties of the plasmonic device is tailored optical property of the plasmonic absorber. There have been numerous demonstrations of optical response from UV to IR spectrum using metallic nanostructures and semiconducting nanostructures. Therefore, it is feasible to demonstrate a plasmon field effect transistor that has an ultra-wide spectral response from visible to IR using engineered plasmonic structures.

Current IR Detector Technology and Problem

Current photodetector technology relies on the optical properties of the semiconducting materials. Semiconductor based photodetectors detect the incident light by converting the optical power to an electrical current. The semiconducting materials used in most of these detectors have limited optical properties due to the bandgap of the materials. For example,

to detect from visible to IR, up to 2μm wavelength range, at least 3 sensors are required such as silicon, indium gallium arsenide and lead sulfide. Therefore, there is a need for a detector device that has a wider spectral response from visible to IR within a single sensor.

Another issue of the photodetector is the thermal noise. When the photodetector detects low energy photons (i.e. infrared), it requires lower operating temperature to suppress the noise. Current semiconductor based detection technology cannot solve this issue due to fundamental material properties. One of the most popular IR detector materials is $Hg_{1-x}CdxTe$ (HgCdTe). This material provides a wide range of tailored detection spectra (1-30μm) with a controlled ternary alloy structures [24]. HgCdTe based detector development has been furthered primarily for military applications. There have also been lots of efforts to develop other alternative IR detector technologies such as InSb-based III–V materials, AlGaAs multiple quantum wells, InAs/GaInSb strain layer superlattice structure, pyroelectric detectors and silicon bolometers [25-29]. These alternate technologies may promise to be more manufacturable, but the HgCdTe has been the most successful IR detector technology up to now. Even though HgCdTe technology has been used for many decades, it still suffers from a bulk, surface and interface instability due to a weak Hg-Te bond. Separate sensors or materials are required for different sub-bands within the UV to MIR wavelength range. For example, AlGaN, Si, InGaAs and PbS based PDs are used for the four important sub-bands, 0.25 μm-0.4 μm (UV), 0.45 μm-0.8 μm (visible), 0.9 μm-1.7 μm (NIR), and 1.5 μm-2.6 μm (MIR), respectively. In addition, the operating temperature of most of the IR sensors shown in Figure 1.1 is not the room temperature. To suppress the noise, these detectors need to be operated at low temperature.

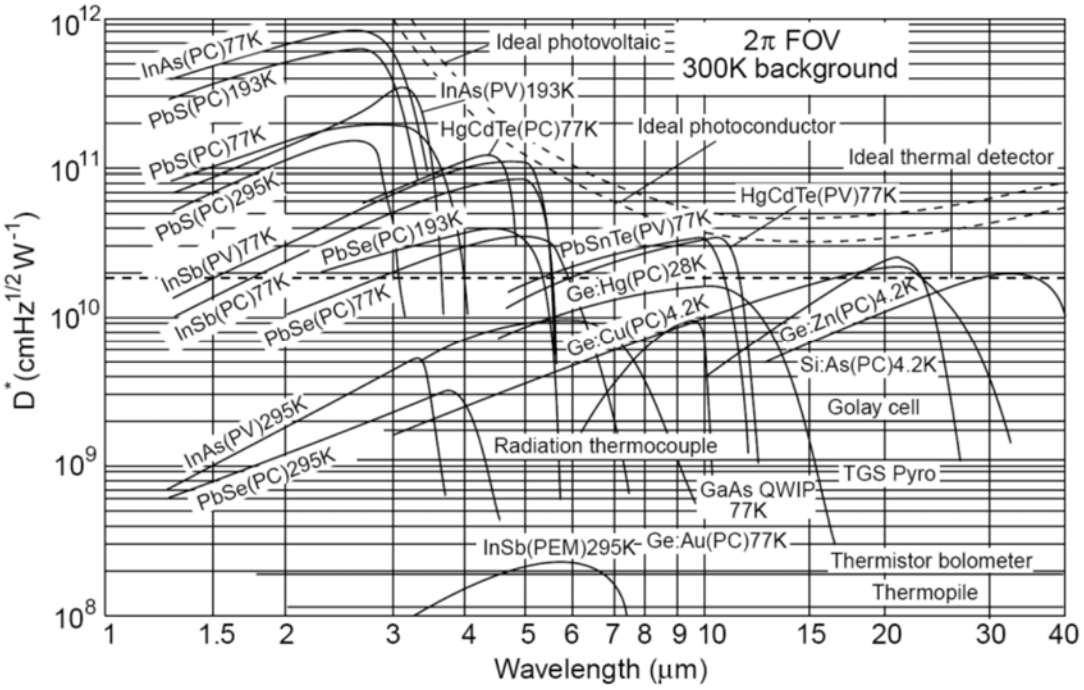

Figure 1.1 Comparison of the D of various commercially available infrared PDs when operated at the indicated temperature [30, 31].

In summary, current visible to IR detectors have two critical defects that are neccessary to solve: separate materials are required for different sub-bands within the visible to IR range and the operating temperature of most IR sensors is not at room temperature. To suppress the noise, these detectors need to be operated in low temperatures. To solve this problem, we propose a plasmonic hybrid device. Plasmonic nanostructures offer several advantages over the current photodetector technology. Plasmonic nanostructures can extend a detection spectrum beyond the IR wavelength. Also, localized surface plasmon resonance is very stable to temperature variations.

Plasmon FET and IR detection using Nanometer Pattern

It is well-known that the metal based localized surface plasmon resonance is very stable to temperature variations. Therefore, we expect that the plasmonic absorption and following hot electron injection based device operation can be effectively performed at room temperature. One of the plasmon FET's advantages will be to provide stable room temperature operation in the IR wavelength.

The plasmon FET is a very efficient device for the conversion of plasmon energy into electric currents [32]. The plasmon FET consistes of thin film transistor and incorporated gold nanoparticles (NPs) on top of the semiconductor as shown in Figure 1.2. A wide band gap material such as ZnO or IGZO, which doesn't have any overlap in optical absorption with the plasmonic absorption of the gold NPs, is used as a transistor channel. This device amplifies and detects the localized surface plasmon energy. In other words, this device efficiently transfers plasmon-induced hot electrons from the Gold NPs to the semiconductor.

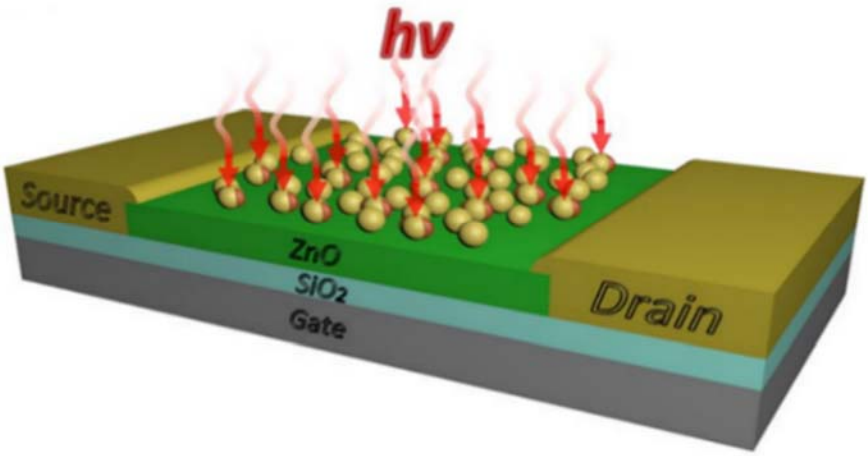

Figure 1.2 Illustration of plasmon FET structure [33]. Copyright (2016) Hossein Shokri Kojori.

The plasmon effect is tunable by the shape, material, size and environment of the nanostructures [7-10]. Gold NPs are incorporated onto the active layers using a thermal reflow method. The 5nm-thick gold film is deposited on top of the semiconductor using an electron beam evaporation process followed by a 300°C heat treatment for 10 minutes, which creates self-assembled gold NPs with broad size distribution from 5nm to 30nm in diameter as shown in Figure 1.3 (a). Figure 1.3 (b~d) show the results when the reflow condition and the thickness of gold film change.

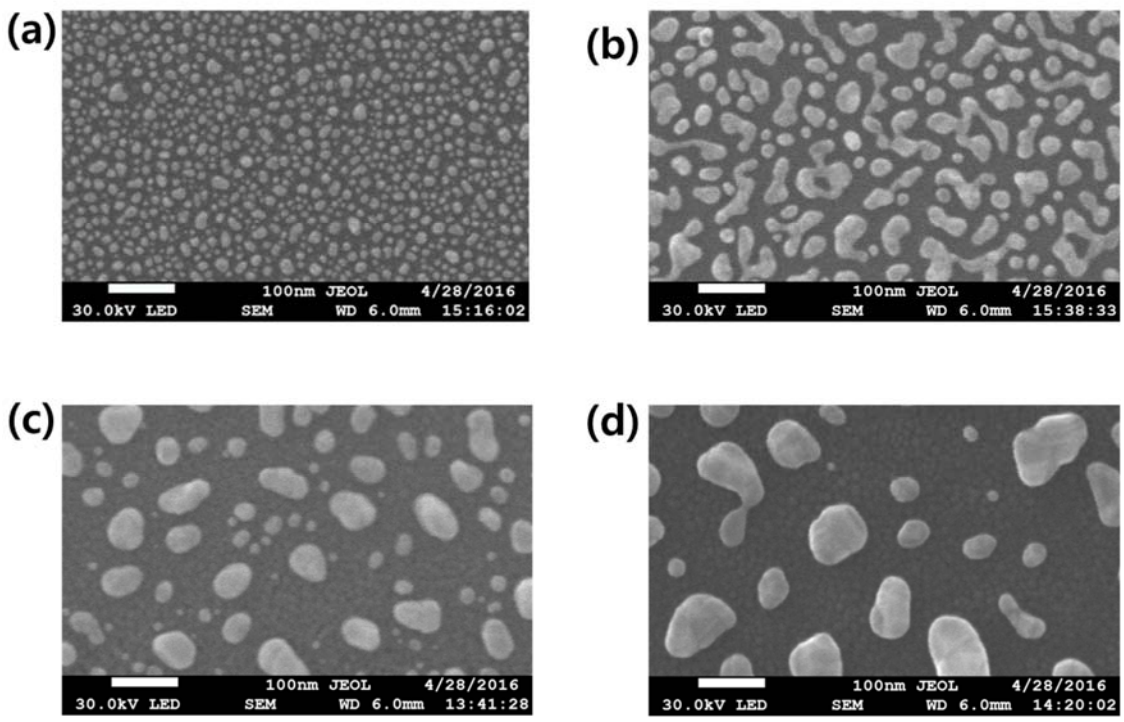

Figure 1.3 SEM pictures of gold NPs obtained with a 5nm gold film after heat treatment at 300°C for 10minutes (a), gold NPs achieved with a 5nm gold film at 300°C heat treatment for 12minutes (b), gold NPs with a 3nm gold film at 300°C heat treatment for 10minutes, and gold NPs with a 7nm gold film at 300°C heat treatment for 10minutes.

Spin-coating and drop-casting with solution based nanorods were tested on the plasmon FET. With these methods, gold nanostructures were too difficult to be incorporated on top of the plasmon FET and failed to generate an IR plasmon peak. Therefore, the gold nanostructures for IR absorption in the plasmon FET is fabricated using an electron beam lithography (EBL) process. We succeeded in combining the plasmon FET with different sizes and shapes of metal nanostructures and controlling the size distribution by using Nanometer Pattern Generation System (NPGS) as shown in Figure 1.4. NPGS is a system for doing advanced electron beam lithography with a Scanning Electron Microscope (SEM). A principal goal of controlling the size and shape of metal nanostructures is to develop a general understanding of how plasmon resonances are determined by nanostructures' size and shape. Moreover, this work offers an ultra-wide spectral range because plasmon resonances can be tuned over a wide range by changing the nanostructure size, shape, metal and host refractive index.

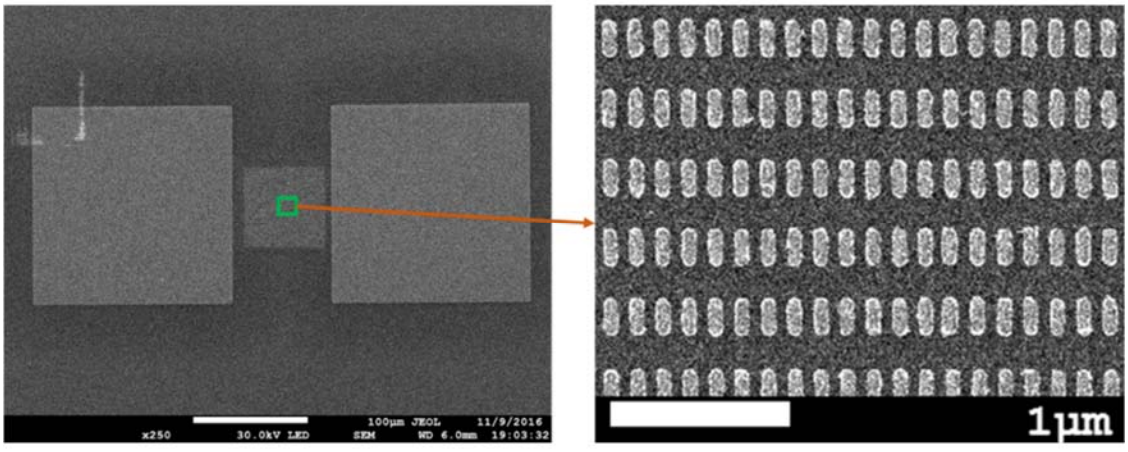

Figure 1.4 SEM images of fabricated Plasmon field effect transistor (left) and the gold nanorods which are made by NPGS (right) on top of the plasmon FET semiconductor.

Resonant Frequency that Depends on the Composition, Size, Geometry, Dielectric Environment and Separation Distance of Nanostructures

We will use the plasmon FET as an efficient visible to IR detector device by using NPGS to control the metal nanostructure. There have been various materials and nanostructures studied to explore their plasmonic properties. In this section, we discuss and review metal plasmonic nanostructures and their plasmon resonance peak wavelength up to IR.

Nanoshells: 10nm thick Au and Ag nanoshells with 100nm diameter silica core were prepared and the theoretical plasmon response of them in water directly compared as shown in Figure 1.5. The plasmon resonance peak of silver nanoshell appears at a shorter wavelength than the corresponding gold nanoshell peak [34].

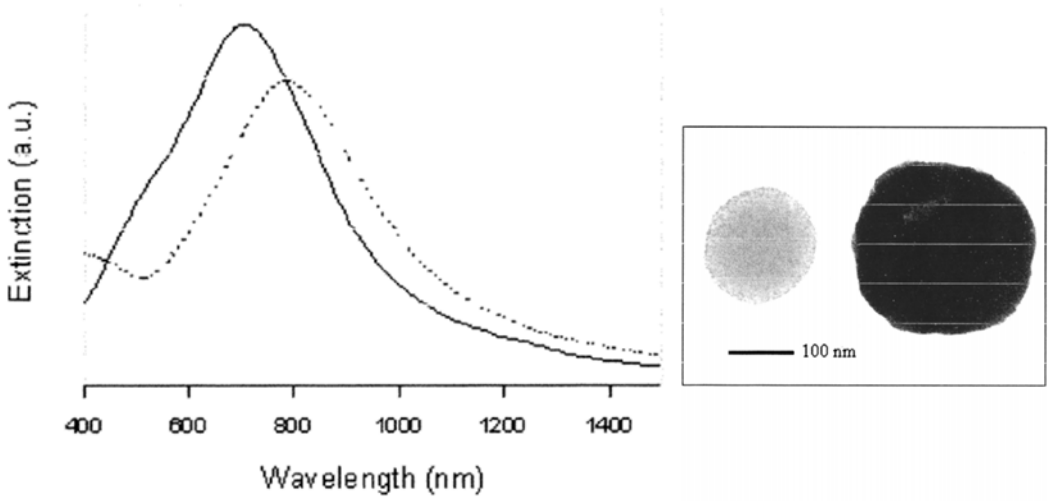

Figure 1.5 Comparison of the theoretically predicted extinction spectrum in water of a silver nanoshell with a core radius of 50 nm and shell thickness of 10 nm (solid line) with that of a gold nanoshell of the same dimensions (dashed line) (left). TEM image of decorated silica particle before (center) and after (right) silver deposition [34]. Copyright (2001) American Chemical Society.

Plasmonic Antenna: 1 nm of Ti covered by 30 nm of Au array was fabricated onto a lightly doped (1-10 Ω-cm) n-type silicon with a width of 50 nm, and different lengths from 110 to 116, 122, 128, 134, 140, 146, 152, and 158 nm. Also 50 nm thick layer indium tin oxide (ITO) was deposited onto the top surface and indium-tin blend was added on the back side of the device to be electrically connected as shown in Figure 1.6 (left). The structure is surrounded by an insulating SiO2 region. Figure 1.6 (right) shows photocurrent spectra for nine different Au antenna lengths. The spectral response peaks exhibit a linear redshift with increasing the nanorod length [35].

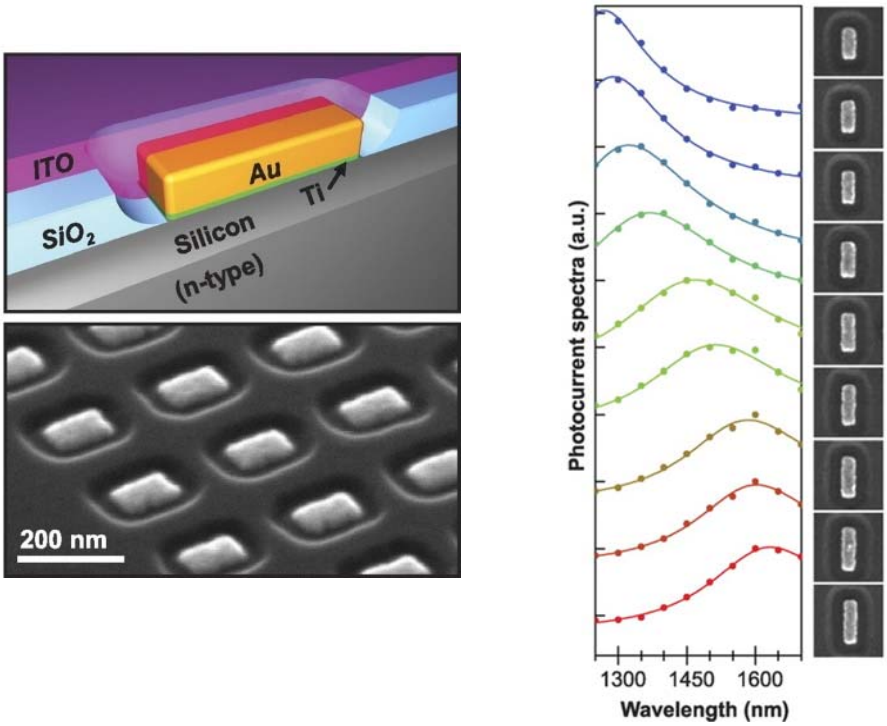

Figure 1.6 Representation of a single Au resonant antenna on an n-type silicon substrate (left top). Scanning electron micrograph of a representative device array prior to ITO coating (left bottom). Photocurrent spectra for nine different Au antenna lengths with 50 nm wide and 30 nm thick: 110, 116, 122, 128, 134, 140, 146, 152, and 158 nm [35]. Copyright (2011) American Association for the Advancement of Science.

Au-Nanorods: Au-NRs were fabricated on TiO2 (block size: 125 x 125 x 40 nm, and inter block distance: 275 nm, 175 nm, and 75nm respectively) as shown in Figure 1.10 (a-c). Figure 1.7 (d) shows the extinction spectrum of Au-NRs. The spectral response peaks exhibit redshift with increasing the inter block distance [36].

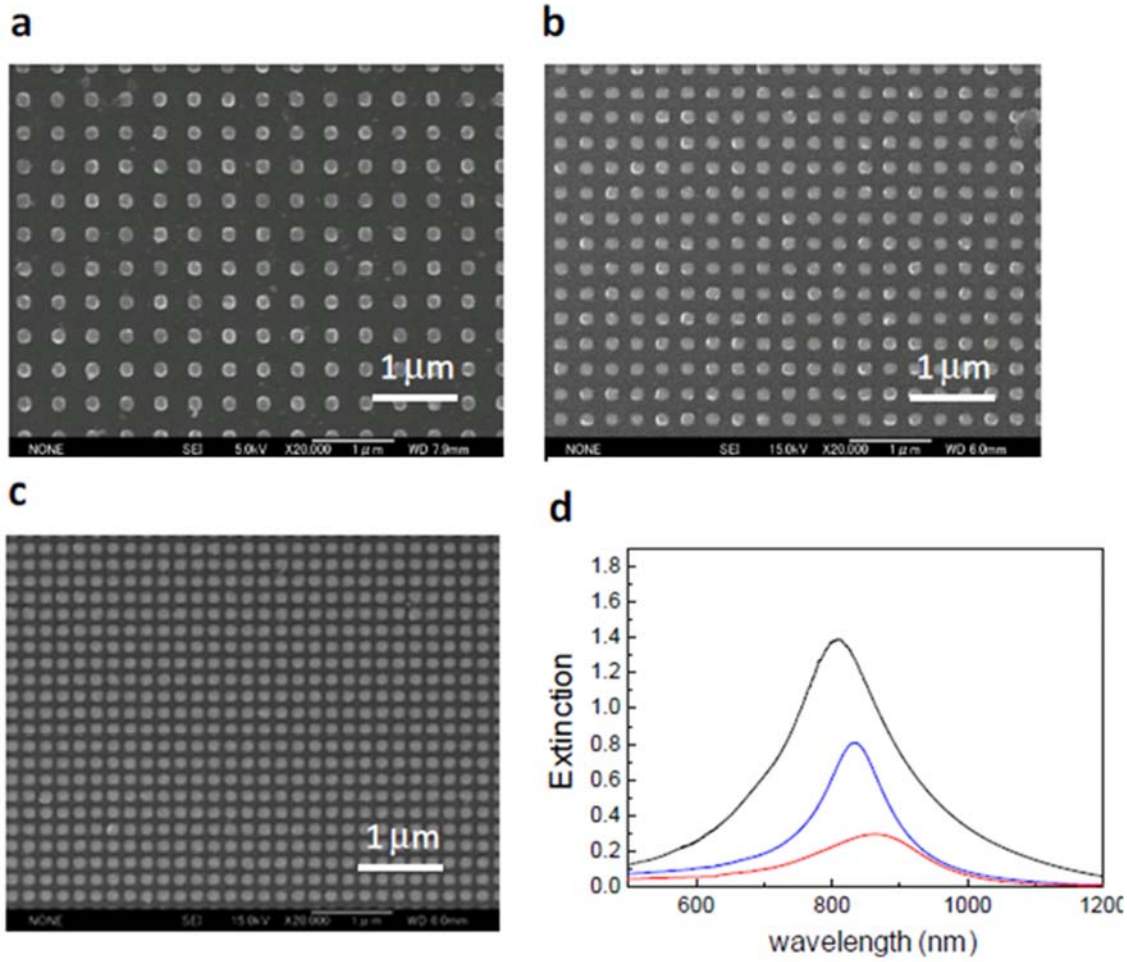

Figure 1.7 SEM images of Au-NRs fabricated on the TiO2 single crystal (block size: 125 x 125 x 40 nm, and inter block distance: 275 nm (a), 175 nm (b), and 75 nm (c), respectively. Extinction spectra of gold nanoblocks (inter block distance: 75 nm black line; 175 nm blue line; 275 nm red line, respectively), (d) [36]. Copyright (2010) American Chemical Society.

Au- Nanowire: A 50nm-thick gold nanowire array with widths of 82, 112, 136, 155, 178, 209, 243 and 273 nm were fabricated onto a TiO_2 substrate as shown in Figure 1.8 (left). The plasmon resonance peaks show red shift by up to 667nm wavelength when the width is increased until 273nm as shown in Figure 1.8 (center). Figure 1.8 (right) shows the photocurrent responsivity of ohmic devices which includes interband transitions (from d-band) [5].

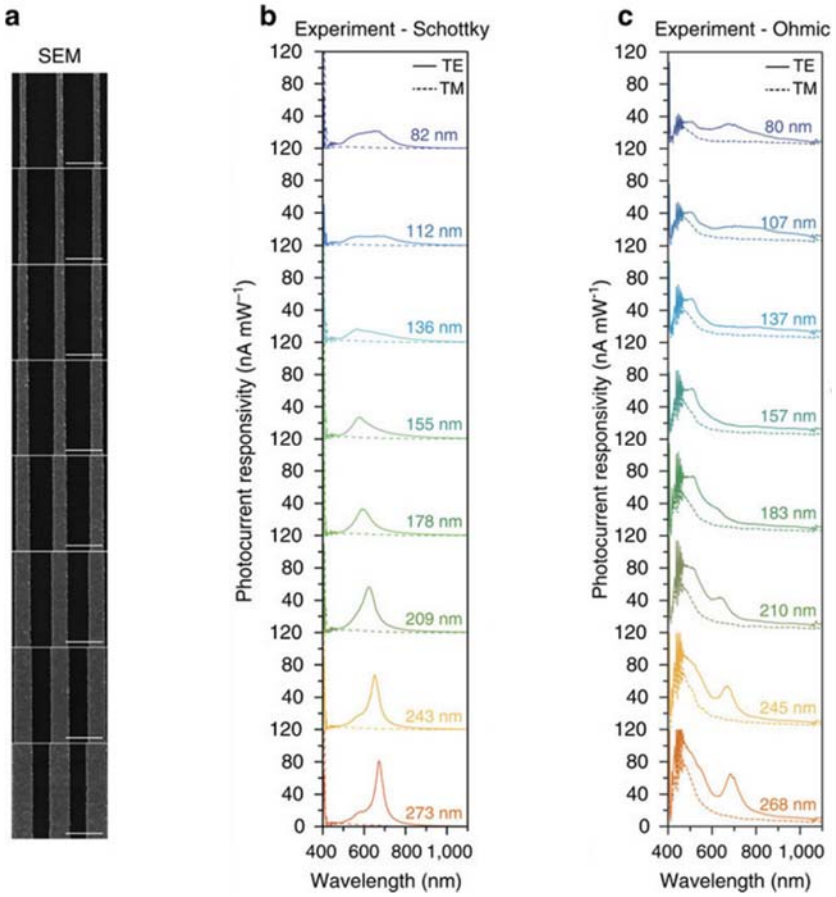

Figure 1.8 SEM images of the different nanowire widths from 82 to 273 nm with 50 nm thickness (left, scale bar is 500 nm). Experimentally measured responsivities for Schottky devices when excited with TE (solid) and TM (dashed) polarizations (center). Experimentally measured responsivities of ohmic devices (right) [5]. Copyright (2015) Rights Managed by Nature Publishing Group.

Ag- Nanocubes: Ag nanocubes were prepared with the edge lengths of 36, 58, 99, 144, and 172 nm, respectively as shown in Figure 1.9 (left). The localized surface plasmon resonance (LSPR) peak of the nanocubes displayed a continuous red-shift from 430 to 468, 497, 513, and 537 nm as the edge length of the nanocubes increases as shown in Figure 1.9 (right) [37].

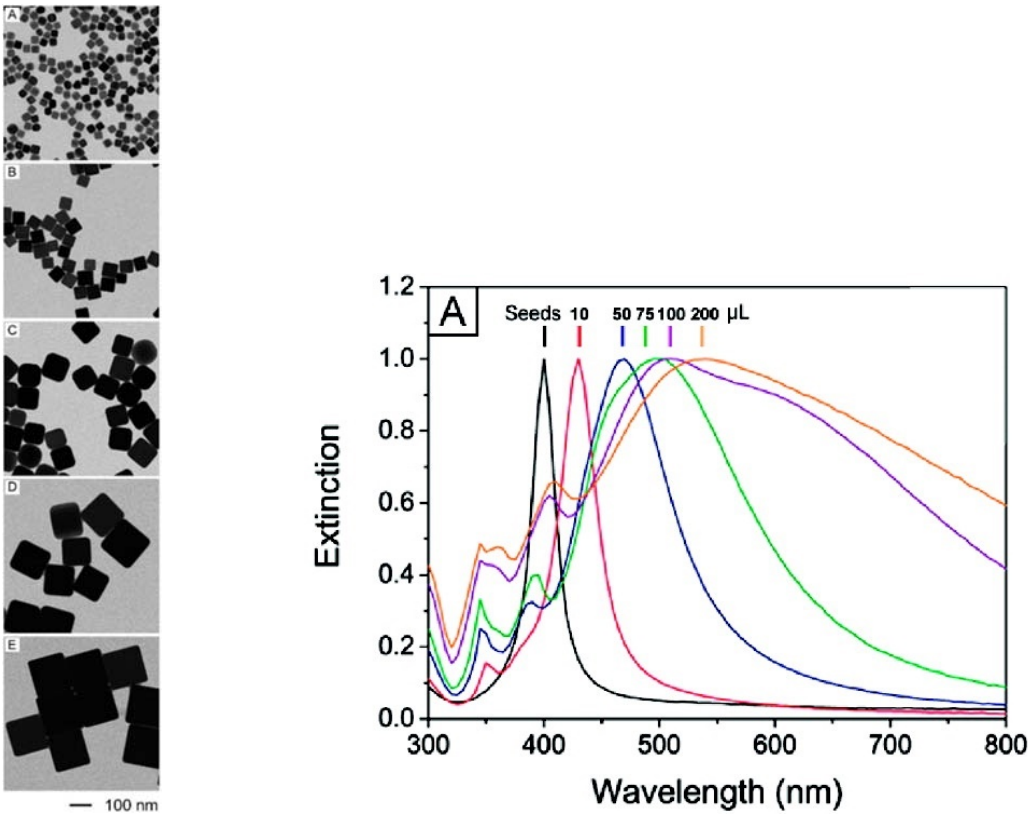

Figure 1.9 (A-E) TEM images of Ag nanocubes with edge lengths of 36, 58, 99, 144, and 172 nm, respectively (left) and the extinction spectra of the nanocubes (right) [37]. Copyright (2010) American Chemical Society.

Triangular Ag Nanoplates: The triangular Ag nanoplates were fabricated with different corner sharpness as shown in Figure 1.10 (left). During the aging process, the sharp corners of the Ag nanoplates gradually became rounded, eventually leading to the

formation of circular disks. The decreasing corner sharpness is correlated with a blue-shift in the extinction spectra of the nanoparticles in solution as shown in Figure 1.10 (right) [38]. Copyright (2010) WILEY-VCH Verlag GmbH & Co. KGaA, Weinheim.

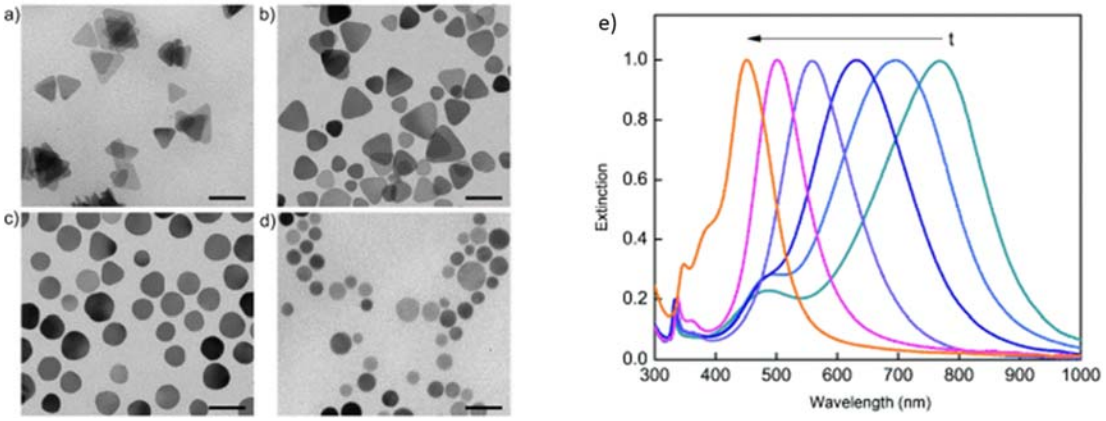

Figure 1.10 TEM images of the triangular Ag nanoplates after they had been aged at 80 °C for a) 0 h, b) 1 h, c) 4 h, and d) 9 h, respectively. The sharp corners of the Ag nanoplates were gradually rounded to generate circular disks with reduced lateral dimensions. Scale bars, 50 nm. e) UV/Vis extinction spectra taken from the corresponding samples [38]. Copyright (2010) WILEY-VCH Verlag GmbH & Co. KGaA, Weinheim.

Summary

This section reviewed the relationship between the plasmonic properties of noble metal nanostructures and their physical parameters including metal composition, size, shape, interparticle gaps and the refractive index of their environment.

The size of a nanoparticle determines the peak position of an LSPR mode. The charge separation on the nanostructures increases when the size is increased. It lowers frequency for the collective oscillation of electrons and causes the resonance peak to red-shift. The shape of a nanostructure such as a corner sharpness has a large effect on the plasmonic

properties. Nanostructures with sharp corners red-shift compared with rounded structures of same sizes because sharp features increase charge separation and reduce the restoring force for the dipole oscillation. It causes a reduction in resonance frequency and thus red-shift in wavelength. As the interparticle gap decreases and nanostructures approach one another, their properties are altered due to the strong coupling between the LSPs of the nanostructures during excitation. The refractive index of materials surrounding metal nanostructure can affect a nanoparticle's optical properties. The plasmonic nanostructures have extreme sensitivity to the refractive index. Also, LSPR peaks can be tuned by changing metal nanostructure composition. Gold has the resonance peak at a lower frequency than the peak of silver.

All these parameters play an important role in the development of LSPR peaks at visible to IR spectrum. We will change the refractive index of the nanostructure environment as it is the simplest approach to engineering the plasmonic properties effectively and then the size and shape of metal nanostructures will be manipulated using Nanometer Pattern Generation System.

Structure of Dissertation

In chapter 2, we review the essential background to understand the major results of this paper. It includes thin film transistor (TFT), surface plasmon resonance (SPR), LSPR, Schottky junction, plasmon FET. Chapter 3 provides a detailed description of the fabrication process and device characteristics, and chapter 4, 5 and 6 present the major experimental results. In chapter 7, we will discuss the future work from this research.

Chapter 2: BACKGROUND

Plasmon FET is a hybrid device that consists of a thin film transistor and metallic nanostructures. Therefore, in this chapter, we would like to go over the operation principles of the field effect transistor. A brief discussion of ZnO based thin film transistor will follow. The most important component of the plasmon FET is the plasmonic nanostructures. We will discuss the general concept of surface plasmon resonance and its underlying physics, then more specifically, we will discuss localized surface plasmon resonance which occurs when the electrons are confined in a nanostructure. Finally, we will review the working principles of the plasmon FET.

Thin Film Transistor

The thin film transistor (TFT) falls in the class of field-effect transistor (FET). The most popular FET is the metal oxide semiconductor field-effect transistor (MOSFET). TFTs and MOSFETs have similar structure, operation principles, and development histories. The active current-carrying layer in TFTs is a thin film semiconductor while MOSFETs are made on Si wafers and use bulk-silicon as the active layer as shown in Figure 2.1. The first conceptualization of the FET was done in 1925. The idea was to control the current flow and conductivity in a semiconductor triode structure by the influence of a transverse electric field. At that time, no evidence existed for the production of these devices due to limited knowledge of semiconductor materials and the inability of vacuum techniques to produce thin films [39-43]. After 37 years, Weimer demonstrated the first TFT using a vacuum technique and shadow masks. The TFT used a polycrystalline cadmium sulfide (CdS, n-type semiconductor) and a silicon monoxide insulator [44-46].

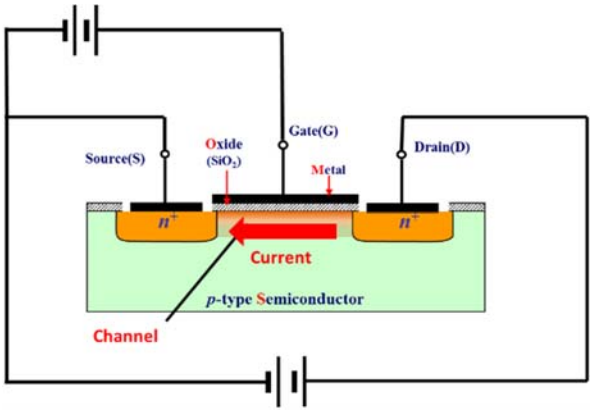

Figure 2.1 The metal oxide semiconductor field-effect transistor [47].

The first use of the silicon as the semiconductor of the TFT came from a report in 1979 in which they used hydrogenated amorphous silicon (a-Si: H) with a silicon nitride gate dielectric layer as shown in Figure 2.2. An a-Si layer, about 1μm in thickness, was deposited onto the Si-nitride again by a RF glow discharge technique such as plasma-enhanced chemical vapor deposition (PECVD) [48].

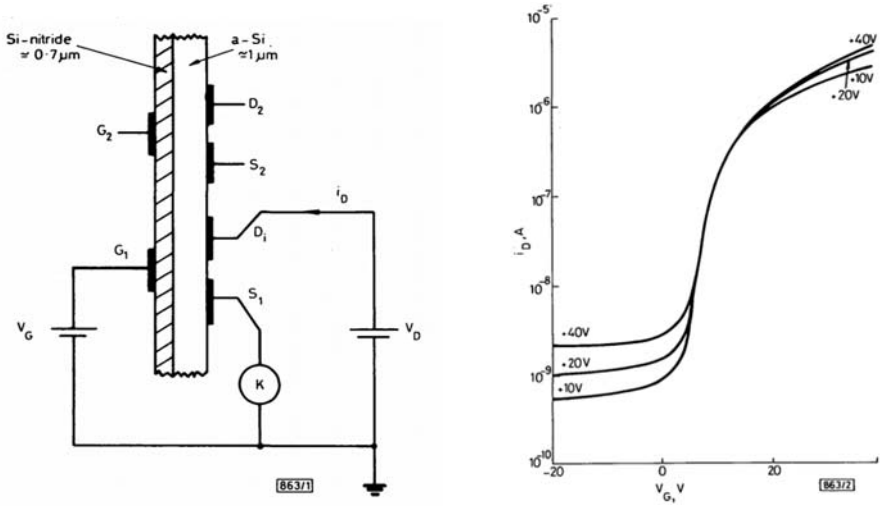

Figure 2.2 Schematic diagram illustrating the design of the first a-Si: H TFT. G, gate electrodes; S, D, source and drain electrodes; K, Keithley electrometer (left). Drain current i_D plotted logarithmically against positive and negative gate voltages V_G for the given values of drain voltage V_D (right) [48]. Copyright (2013) The Electrochemical Society.

There were constant efforts to improve the performance of TFTs because of the low carrier mobility of a-Si: H TFTs which is less than 1 cm^2 /Vs. Low-temperature polycrystalline silicon (LTPS) had attracted considerable attention as an alternative TFT material because the electron mobility in LTPS is more than 100 cm^2 /Vs. LTPS has been synthesized at relatively low temperatures that do not exceed 600 °C compared to traditional methods above 900°C [49]. Excimer-Laser Annealing (ELA) method is used to produce the LTPS TFT by melting and crystallizing a-Si material without heating the substrates [50]. LTPS films formed by position-controlled large grain growth technology using the ELA method increased the electron mobility up to 914 cm^2 /Vs because larger grains of LTPS reduce scattering from grain boundaries [51]. Figure 2.3 shows Silicon-based crystal structures using ELA method and without annealing.

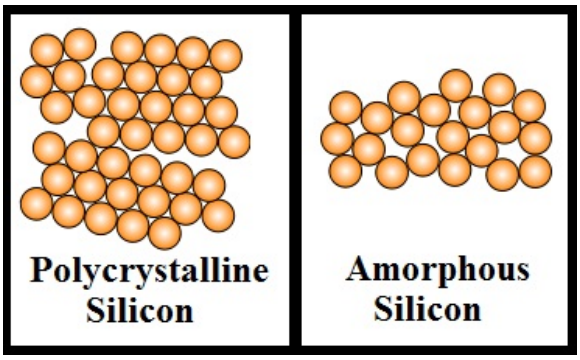

Figure 2.3 Silicon-based crystal structures using Excimer-Laser Annealing method (left) and without Annealing (right).

There are continued efforts in search of new types of TFTs that lower the cost of Si-based TFTs and improve the performance, since the fabrication cost for the laser annealing process is high [52]. Oxide TFTs, which use amorphous oxide semiconductor (AOS)

materials such as ZnO and In- and Ga-doped ZnO (IGZO), have been researched in recent years [53-55]. They are fabricated by the sputtering method and have high mobility. This type of TFT has electron mobilities exceeding 10 cm^2 /Vs which is one order of magnitude larger than that for a-Si: H TFT.

The Plasmon FET uses this n-type oxide TFT device configuration. The TFTs are used for weak-signal amplification. They can control large current by using small gate voltage. When gate to source voltage is applied, a significant density of electrons is pulled toward the gate. However, the insulator between the oxide semiconductor and the gate prevents the electrons from being delivered to the gate. Thus, the electrons are accumulated at the insulator and semiconductor interface and form a conductive channel. The channel allows the flow of electrons generated in the source electrode to the drain electrode, depending on the drain-to-source potential. As gate voltage is increased, the conductive channel is formed better. Hence, the drain-source current flows better by affecting the size and shape of the channel as shown in Figure 2.4. If a negative voltage is applied to the gate, electrons are pushed up because of the electric field. Thus, the electrons are reduced close to the insulator. In this situation, the current flowing between the source and the drain is also reduced.

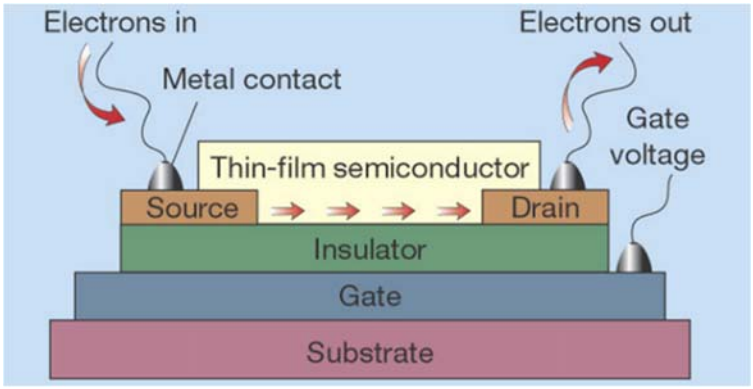

Figure 2.4 The thin film field effect transistor.

ZnO based TFT

To avoid the overlap of the absorption spectra with the plasmon absorber, wide bandgap semiconductors, i.e., ZnO and InGaZnO (IGZO), are used as the active layer of the plasmon FET. Wide bandgap semiconductors which have bandgaps between 2eV and 4eV are semiconductor materials that have higher energy electronic band gaps than conventional semiconductor materials like silicon which has a bandgap of 1 to 1.5eV [56, 57]. The bandgap is the energy difference between the bottom of the conduction band and the top of the valence band in semiconductors and determines the wavelength to operate photovoltaics most efficiently. The equivalent wavelength for light energy is obtained by dividing the constant 1240nm·eV by the energy in eV from the Planck's Equation $E = h\nu = hc/\lambda$ ($\nu = c/\lambda$) when E stands for energy, ν represents frequency, h is Planck's constant (6.625×10^{-34}J·s or 4.135×10^{-15}eV·s), c is speed of light (2.998×10^{8}m/s), λ stands for wavelength and a simplified version of hc is 1240nm·eV (4.135×10^{-15}eV·s x 2.998×10^{8}m/s = 1239.673nm·eV).

Wide bandgap materials are useful at shorter wavelengths than other semiconductor materials. For example, ZnO has a band gap energy of 3.41eV [58], and the equivalent wavelength for that energy is 360nm by dividing the constant 1240 nm·eV by the energy 3.41eV. 360nm for ZnO is the minimum optical wavelength to be transparent [59]. In other words, wide bandgap photovoltaics are difficult to convert visible light and infrared light into electricity. The TFT structure is suitable for wide bandgap semiconductors to detect wide range spectral response such as visible light and infrared light through localized surface plasmon resonance of nanostructures. Wide bandgap materials have several characteristics compared to lower bandgap materials. Wide bandgap semiconductors can

operate at high temperature on the order of 300°C [60] and switch larger voltages [61]. They can be highly useful for military applications because the high-temperature tolerance can be operated at much higher power levels under normal conditions.

Plasmonics

Plasmonics is the study of the interactions between light and metals, to be specific between electromagnetic fields and free electrons in metal nanostructures. It has been widely studied very recently, due to the rapid progress of nanofabrication technology. Plasmonic devices have the advantages of both electronic devices and optical devices such as operating speed, size and integration capability as shown in Figure 2.5. Thus, plasmonics has been an important research area rapidly impacting every facet of optics and photonics. One of the most urgent needs of plasmonic device technology is an efficient bridge device that can convert optical signals to electrical signals. My research focuses on a plasmo-electric device which can convert plasmonic signal to electrical signal. And we use this fascinating property to develop a photodetection device that can detect ultra-wideband spectrum. The details of the project will be discussed later.

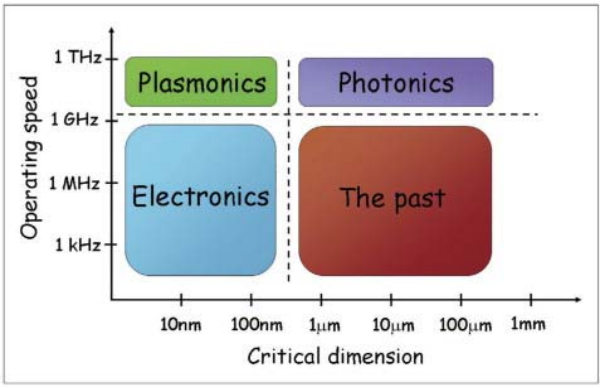

Figure 2.5 Operating speeds and critical dimensions of various chip-scale device technologies, highlighting the strengths of the different technologies [62]. Copyright (2006) Elsevier Ltd.

The history of the localized plasmonic resonance is quite long. People discovered this fascinating physical phenonmenon a great while ago. The practical use of gold nanoparticles as a pigment was to stain the Lycurgus cup in 4th century in Rome as shown in Figure 2.6. They used gold nanoparticles to make this cup. When light is shown through the cup, the gold nanoparticles reflect red light. Electrons belonging to the metal NPs vibrate and alter the color when hit with light. Following slides will explain practical use of plasmonic nanostructures in detail.

Figure 2.6 The Lycurgus cup, 4th CE. A.D. in Rome (British Museum) [63].

The nanoparticle's optical property are different from the property of its bulk material. For example, when gold is ground down to particles as small as 20 nanometers in diameter, the color of the gold is red due to the strong absorption in the sky blue region of the spectrum. Sky blue is 522nm in wavelength. This happens because the gold nanoparticle becomes a strong absorber of specific wavelength. This strong absorption is due to the plasmonic resonance.

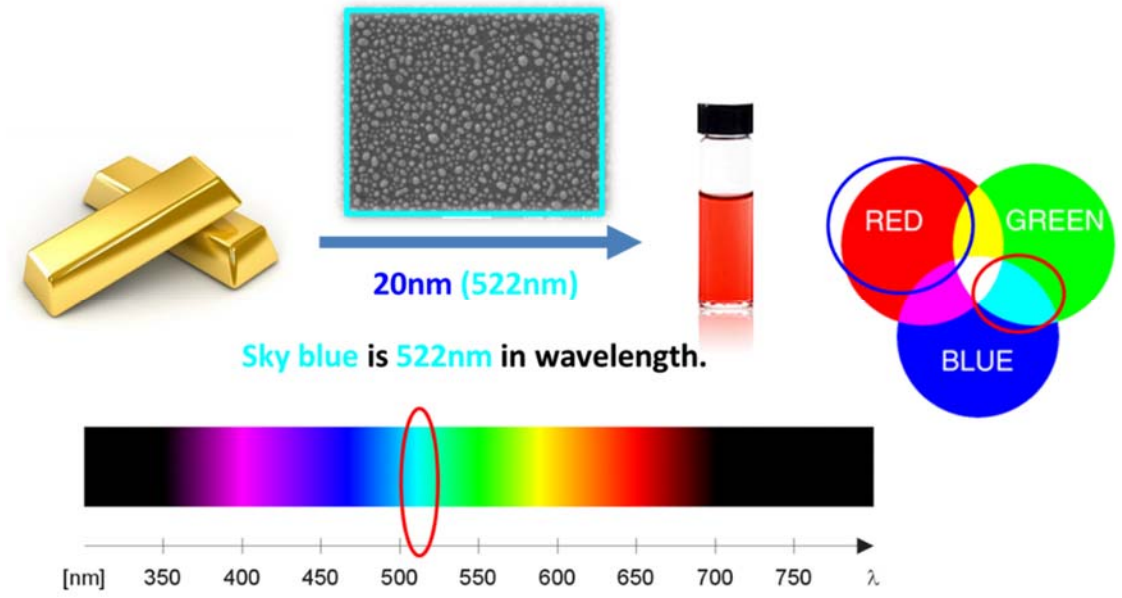

Figure 2.7 Schematic indicating absorption property at 522nm wavelength by the 20nm gold nanoparticles in diameter. The color of the gold is red, owing to their absorption property of blue color wavelength.

The plasmonic property can be tailored by changing the size of the nanostructures. If we have larger nanoparticles, the plasmonic oscillation wavelength gets longer. This is called red-shift. For example, 100nm gold nanoparticles become pink color because the larger nanoparticles absorb more red color and less blue color in the visible range. The tailored plasmonic property can be achieved by changing the surrounding host materials. Because the plasmonic resonance frequency is sensitive to the refractive index of the surrounding material. For instance, when gold nanoparticles have some material on their surface that has a higher refractive index, the plasmonic absorption spectrum red-shifts because the material increases the average bulk refractive index. Gold nanopaticles are readily conjugated to antibodies and other proteins due to the affinity of thiol (-SH) groups

for the gold surface, and gold-biomolecule conjugates have been widely incorporated into diagnostic applications. By using all these tailored properties, Gothic churches made beautiful stained glass using gold nanoparticles.

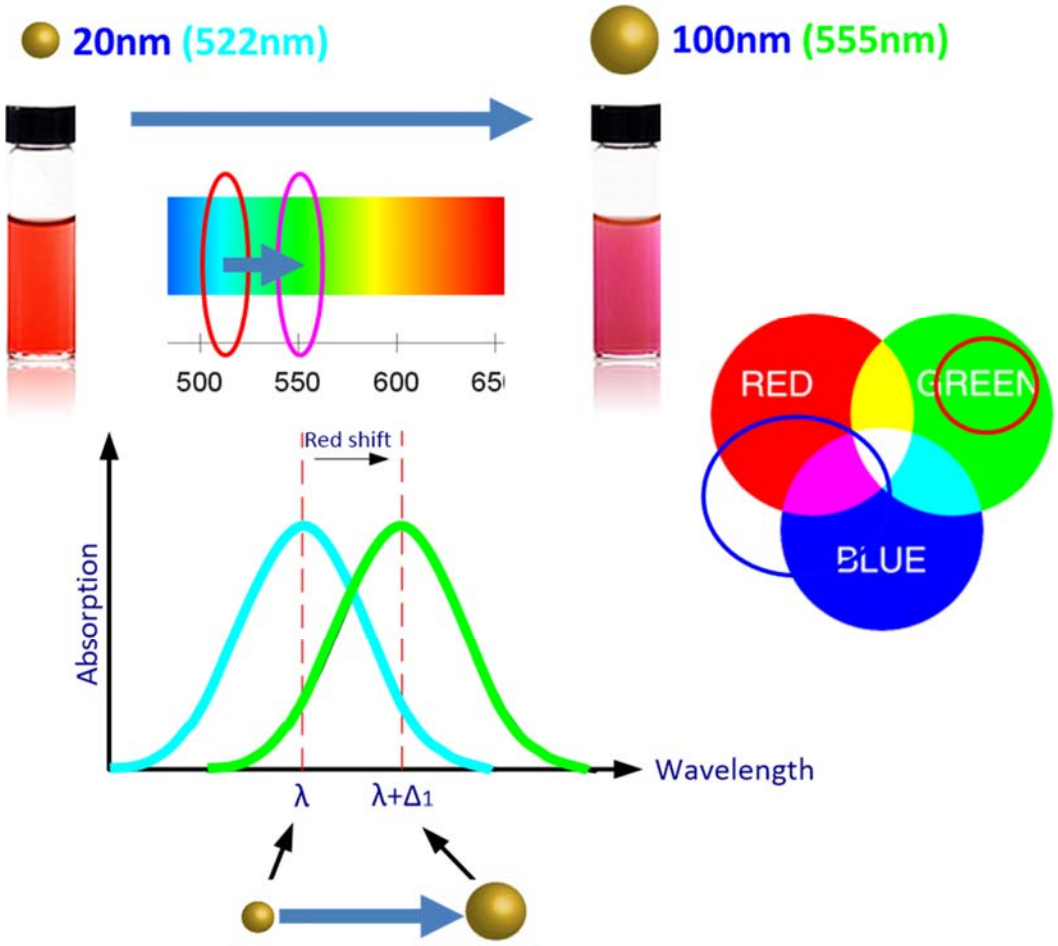

Figure 2.8 Schematic indicating absorption property changes when a gold nanoparticle diameter increases from a 20nm to a 100nm. A 100nm diameter nanoparticle absorbs green color and looks like pink color.

Surface Plasmon Resonance

Heinrich Hertz discovered the photoelectric effect which discharges electrons from metallic electrodes in 1887 [64]. Albert Einstein suggested that energy of a beam of light is proportional to its frequency v ($E = hv$, Planck's constant h) [65]. The electrical discharge process requires a minimum photon energy which is equal to the metal's work function. In other words, below a certain threshold frequency, light cannot eject an electron from a metal surface, regardless of the intensity. They set the foundation of plasmon-induced hot electrons.

The unique properties of these hot electrons provide attractive opportunities for research and applications. The photoexcitation of hot electrons in a metal can stimulate several effects. A counter-electrode can capture photo-ejected electrons from a metal and generate useful current. Hot electrons can induce photochemical reactions by interacting with molecules on a surface. The energy of hot electrons can desorb small molecules from the surface [6]. Electrons in a metal can be released into vacuum from the metal surface when the electron energy by photon energy exceeds the metal's work function [66]. A metallic nanostructure can trap photo-excited hot electrons, and the hot electrons cause local heating of the metal particle and its surroundings [67, 68]. Photo-ejected electrons can be captured by two-dimensional materials such as an ultrathin semiconductor layer and electrically dope the active layer. Photo-ejected charges in metallic nanostructures can be engineered to enhance and provide valuable control over the emission of hot carriers. The hot carrier generation in metal nanostructures is due to the non-conservation of the momentum of electrons in a confined 0-dimensional structure [32, 69]. These light-matter interactions which are called plasmon effects can be used to harvest solar energy or create

sensitive photodetectors. The plasmon effects have found broad applications in photovoltaic devices [23, 70], photothermic effect [6, 71], photocatalysis [6, 72] and spectroscopy [73, 74].

Plasmons are collective charge density oscillations of conduction electrons in metals. Surface plasmons are those plasmons that are confined to the interface between a dielectric and a conductor and that interact strongly with light resulting in a polariton [4]. The polaritons are named surface plasmon polaritons which are electromagnetic excitations propagating at the interface between a metal and the surrounding dielectric, evanescently confined in the vertical direction [75]. These surface plasmon polaritons, electromagnetic surface waves, are formed by the coupling of the electromagnetic fields to oscillations of the conductor's electron plasma which is called surface plasmon resonance [76].

Optical excitation of surface plasmons was demonstrated by the method of attenuated total reflection [77, 78]. Surface plasmon polaritons have two kinds of modes: non-radiative modes and radiative modes [77]. The plasmon energy of non-radiative modes is transferred to the conduction electrons in metals by Landau damping and create electron-hole pairs, but they cannot decay into photons because their phase velocities (ω/k) are smaller than the speed of light c. However, radiative modes with phase velocities (ω/k) larger than the light speed c can couple with photons [77, 79, 80]. The radiative mode can be excited by light, and the mode reradiates light into almost all directions with maximum intensity at the plasma frequency ω_p [81].

Surface plasmon resonance which is a kind of the non-radiative modes can be excited when the wave vector along with the interface between the metal and the air is matched

with the wave vector of light. Typically, light cannot match the wave vector of metal without some intermediate dielectric of index n as shown in Figure 2.9.

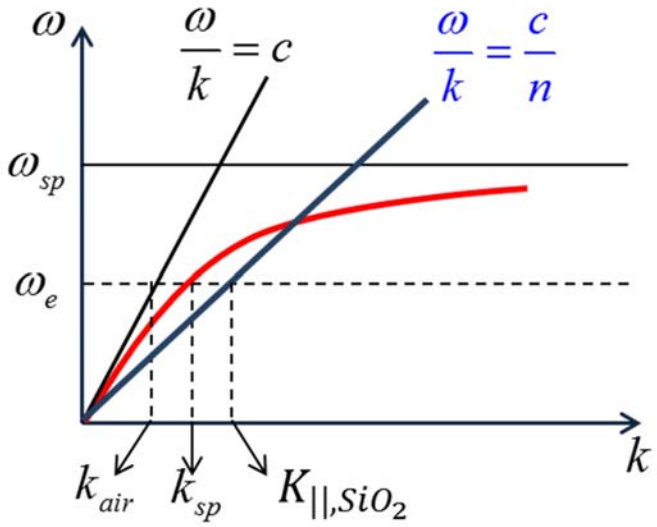

Figure 2.9 Dispersion relations of the non-radiative surface oscillations in the air (black), the prism(blue) and at the boundary gold and air (red) calculated from the optical constants.

A surface plasmon on the gold and air boundary can be excited when incident photons illuminate a prism at an angle greater than the critical angle of total internal reflection by the Kretschmann method as shown in Figure 2.10. To be specific, the incident light from a prism has larger wave vector than the wave vector of the metal and air interface. The size of the wave vector from the prism can be maintained until it passes through the metal film because a thin metal layer (typically ~50nm) is located on a glass prism. By changing the incident angle to the metal thin film through the glass prism, there should be a particular angle that makes the incident wave vector become equal to the plasmon wave vector. If this occurs, the incident electromagnetic wave energy can be strongly absorbed to create surface plasmon resonance.

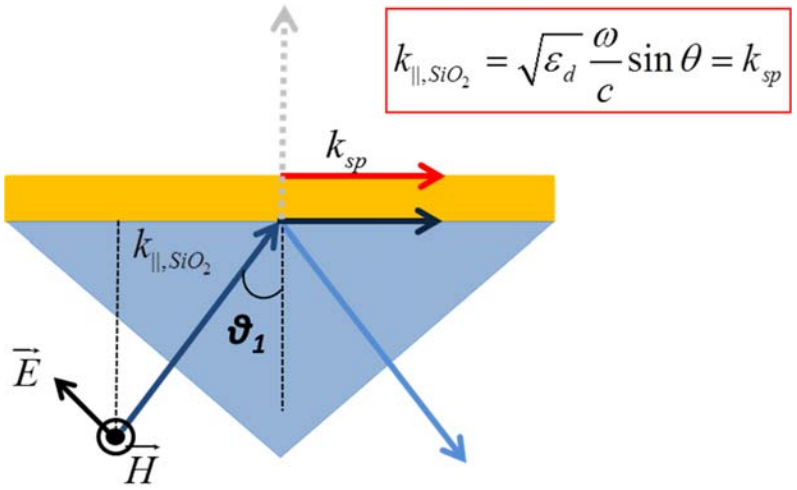

Figure 2.10 Surface plasmon excitation through prism coupling by the Kretschmann method.

Localized Surface Plasmon

A localized surface plasmon (LSP) is a surface plasmon trapped within conductive nanoparticles that are smaller than the wavelength of incident light to excite the plasmon. Localized surface plasmon is not propagated in any direction but aggregated around the metal nanoparticles. Light with the particular frequency is strongly absorbed and scattered by the metal nanoparticles because a sufficient level of the free electrons on the surface of metal nanoparticles vibrates at a particular frequency. The optical phenomenon is a result of the interactions between surface electrons in metal nanoparticles and the electromagnetic wave of the incident light [82]. This interaction produces coherent localized plasmon oscillations at the resonant frequency that cause the enhanced electric fields near the particle's surface and maximizes optical absorption [83]. The resonant frequency strongly depends on the composition, size, geometry, dielectric environment and separation distance of nanostructures.

Typical materials used for NP production are gold, silver, and copper. They release electrons quickly by external stimuli and have negative dielectric constant. Among them, silver exhibits the sharpest surface plasmon resonance peak; while gold has excellent surface stability and inert nature [84]. These metallic nanoparticles are extremely well resonated by visible light [85].

The nanoparticle's optical property is different from the property of its bulk material. Metallic nanoparticles' dimensions match with the quantum size regime. Continuous electron band becomes discrete. Thus, the optical property such as plasmon resonance depends on the nanoparticles' size and the quantity of them. The oscillating electric field by absorbing photon energy causes coherent oscillation of conduction electrons. It manifests itself as high absorption at a particular wavelength which is called LSPR. Polarization charges on the surface of a nanoparticle are accumulated by the dipole behavior as shown in Figure 2.11 [86-90].

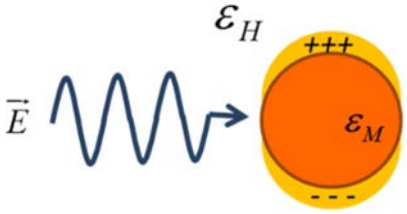

Figure 2.11 Polarization charges on the surface of a nanoparticle by LSPR.

Based on Mie's solution of Maxwell's equation, when only dipole oscillations contribute to the extinction cross-section, the extinction coefficient in Equation (2-1) can be used to obtain the spectrum of metal nanoparticles. This factor is proportional to the volume of the metal nanoparticles (V_M) and is related to the host refractive index matrix of

the nanoparticles. Where λ=wavelength, ε'_H is the dielectric constant of the surrounding medium, $\varepsilon = \varepsilon'_M + i\varepsilon''_M$ is the complex dielectric constant of the bulk metal [91-94].

$$\sigma_{ext}(\lambda) = 18\frac{\pi}{\lambda}\varepsilon_H^{'3/2} V_M \frac{\varepsilon_M^{'}(\lambda)}{[\varepsilon_M^{'}(\lambda) + 2\varepsilon_H^{'}]^2 + \varepsilon_M^{''}(\lambda)^2} \quad (2\text{-}1)$$

The factor value, a magnitude of two, in front of ε'_H in Equation (2-1) is assigned for a spherical particle and can be as large as 20 for nanorods with high aspect ratios [95]. The surface plasmon resonance peak is observed, and the EM field is enhanced when the denominator goes to zero, $\varepsilon'_M = -(2\sim20)\varepsilon'_H$. The resonance peak for gold and silver nanoparticles is matched within the visible wavelength. The extinction coefficient for a nanorod's surface plasmon can be calculated into two distinct modes because of the surface curvature and symmetry [96].

Schottky Junction

A Schottky junction is a junction formed between a metal and a semiconductor [97]. Metals and semiconductors junctions can either be rectifying or non-rectifying [98]. The rectifying metal and semiconductor junction form a Schottky barrier, making a device known as a Schottky diode because Schottky barriers have rectifying characteristics which are suitable for use as a diode. The non-rectifying contact is called an Ohmic contact [99]. A Schottky barrier is a potential energy barrier for electrons near the junction. The Schottky barrier height is one of the primary characteristics of a Schottky barrier, denoted by Φ_B. The value of Φ_B depends on the combination of metal and semiconductor.

Before further discussing the Schottky barrier, it is necessary to introduce the concept of the work function. The idea of the work function was proposed by Albert Einstein for the first time [100]. The work function of a material is the energy required to remove an electron from the Fermi level of the electrochemical potential and give it enough energy to escape to infinity and arrive there with zero energy [101]. The concept of work function can be explained by classical physics. When an electron tries to escape from the metal surface, it leaves a positive image behind on the metal surface, and this positive image attracts the negative electron to turn back to the metal surface. So, the electron cannot leave the metal crystal permanently. From an outside source, an electron requires sufficient energy more than work function to overcome this attractive force.

Two possible types of contact between a metal and a semiconductor are Schottky barrier contact, which is called a rectifying contact, and Ohmic contact. The kind of contact depends on the combination of metal and semiconductor used. The rectifying contact allows current to pass in one direction, while in the Ohmic contact, current can pass in either direction. Here we will discuss the rectifying contact.

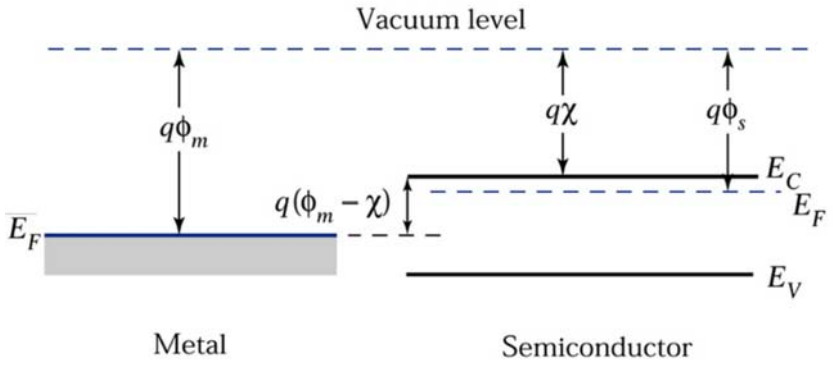

Figure 2.12 Energy band diagram of metal and an n-type semiconductor before making contact.

Figure 2.12 shows the energy band diagram for an isolated metal adjacent to an isolated n-type semiconductor. The vacuum level is a reference level. Φ_M and Φ_S represent the work functions of the metal and semiconductor respectively. The chemical potential (which is known as the Fermi level because the gap between the chemical potential and the Fermi energy can be ignored at low temperatures) of the semiconductor and the metal has been labeled E_F. The amount of energy (χ) between the lowest of the conduction band (E_C) and the vacuum level is called the electron affinity of the semiconductor. For a metal, the electron affinity is the same as the Fermi energy because the electron affinity in the metal is the energy from vacuum level to the highest unoccupied energy level of the metal.

After making contact, electrons can move between the metal and the semiconductor. To be specific, the electrons in the conduction band of the n-type semiconductor move into the metal to lower their energy because the work function of metal is more than the value of the n-type semiconductor. The transportation of electrons from the semiconductor to the metal slightly increases the negative charge of the metal. The induced electric field repels further flow of electrons from the conduction band of the semiconductor into the metal and it causes a deformation of the energy bands only in the semiconductor because the metal has a dominant number of valence electrons compared with conduction electrons in the semiconductor before making contact. Finally, the Fermi level in the semiconductor can be in equilibrium with the metal as shown in Figure 2.13. The barrier height (Φ_{Bn}) for electrons moving from the semiconductor to the metal is referred to as the Schottky barrier.

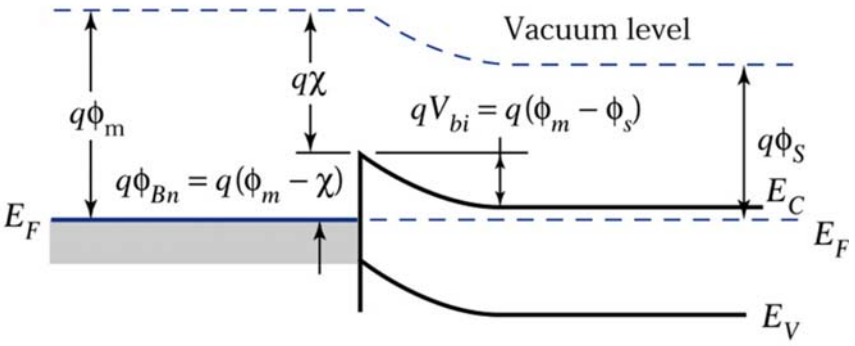

Figure 2.13 Energy band diagram of n-type semiconductor and metal in thermal equilibrium after making contact.

Plasmon Induced Hot Electron Emission based Detector

If the electrons in the metal are thermally excited enough to overcome the barrier, then they can diffuse into the semiconductor conduction band. This effect is a kind of photoelectric effect. One of the important aspects of this field is an efficient use of the absorbed electromagnetic energy via metal nanostructures. Recently, there have been several reports of plasmon induced hot electron detection using photodetector structures. The common design structure of these works is a Schottky junction between nanostructured metals and an N-type semiconductor. This Schottky junction photodetector approach enables a direct conversion of plasmonic energy absorbed in the metal nanostructures into an electrical signal. In addition, various designs of metal nanostructures allowed tailored spectral responses, polarization dependence and photoresponse with a narrow spectral bandwidth.

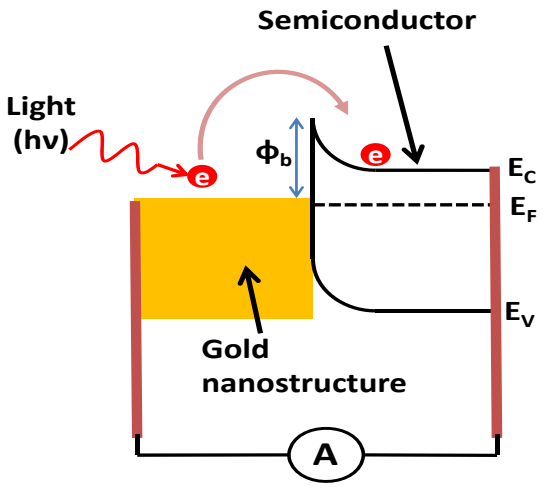

Figure 2.14 Metal-semiconductor Schottky junction hot-electron emission. The band diagram shows plasmonically driven internal photoemission from gold nanostructure to semiconductor. E_C, E_F and E_V stand for conduction band, Fermi level and valance band, respectively. And Φ_b is the barrier energy height [102]. Copyright (2016) Society of Photo Optical Instrumentation Engineers.

The working principle of a Schottky junction based internal hot-electron emission was reported a few decades ago [103, 104]. The photons that are absorbed in a metal contribute to generating 'hot electrons' and, if the hot electron energy is high enough, the hot electrons can overcome the Schottky energy barrier at the boundary between metal and semiconductor [105]. Therefore, the hot electrons can move to the semiconductor, resulting in photocurrent as illustrated in Figure 2.14. The reported works have shown that the generated current reflects exactly the plasmonic absorption in the metal nanostructures. However, all those demonstrations show very low responsivity (A/W) or external quantum efficiency due to the limited absorption in the thin metal structure and inefficient hot electron diffusion from metal to semiconductor. Up to now, the best internal quantum

efficiency (IQE) is 0.2% under no voltage bias. Besides the low efficiency issue, the reported Schottky junction based plasmon detectors use a device structure that has electrically connected plasmonic electrodes. It limits the plasmonic structure design and requires complex fabrication processes. Another issue of the Schottky plasmon detector is the limited detectable energy (lowest photon energy) due to the Schottky barrier height, while this plasmonic metal nanostructures can absorb the photon energy beyond the semiconductor bandgap energy, even up to the THz regime. Therefore, it is needed that a novel device design that can extend a detection spectrum beyond the mid IR wavelengths by taking the advantages of plasmonic nanostructures.

Plasmon Field Effect Transistor

Plasmon field effect transistor (plasmon FET) is a hybrid device which consists of thin film transistor with a back gate and incorporated metal nanoparticles on top of the transistor active layer to efficiently detect and amplify the localized surface plasmon energy as shown in Figure 2.15. High band gap materials such as ZnO and IGZO are used for the active thin film layer of the plasmon FET because they do not have any overlapped optical response with incorporated metal nanoparticles. This kind of transistor is considered as a unipolar transistor because it has one type of charge carriers in its active layer. The nanostructures are electrically isolated from drain and source electrodes.

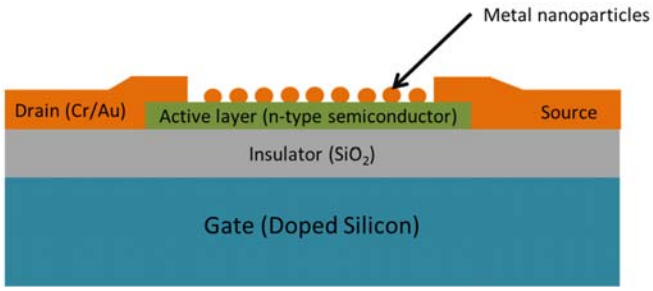

Figure 2.15 Plasmon field effect transistor structure.

In terms of optical properties, the gold NPs with 5-10nm in radius exhibit strong plasmonic absorption around a wavelength of ~520nm. This absorption peak depends on the dielectric constant of the host material surrounding the gold NPs and the size of the NPs. In order to avoid overlap of the absorption spectrum, ZnO for the FET channel material is used. The bandgap of 250nm-thick ZnO thin film is 3.3 eV and shows almost zero absorbance (<0.001%) at the spectral range between 450nm to 1100nm. Thus, it is expected that there will be no optical response in the drain current under illumination at any visible wavelength [106]. Copyright (2016) American Chemical Society.

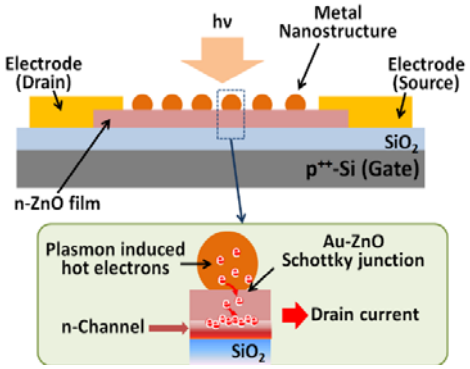

Figure 2.16 Illustration of the operation principle of plasmon FET. Hot-electrons induced by plasmonic absorption in the metal nanostructure can move to the semiconductor. Consequently, it increases the drain current [106]. Copyright (2016) American Chemical Society.

The gold nanoparticles are attached to the ZnO active layer, electrically isolated from all three electrodes (Drain, Source, and Gate). Therefore, the nanoparticles are free from voltage bias while the FET is operating. Also, a Schottky junction is created at the interface of the gold nanoparticle and the n-type ZnO film. Based on the work functions of the two materials, the Schottky barrier is expected to be around 0.6-7eV. Thus, electrons with higher energies than 0.5eV may have a chance to overcome the energy barrier to move

from the gold nanoparticle to the ZnO layer. Since the photon energy of the visible spectrum is greater than 1.7eV, the photons sbsorbed by plasmon resonance creates electron-hole pairs that can migrate from gold to ZnO. Consequently, this process will supply more electrons (charge) in the ZnO channel, resulting in increased Drain current (Id) [107], as graphically illustrated in 2.16. It is a novel device structure of direct surface plasmon detection from electrically isolated nanostructures. The expected current response as a function of wavelength should be matched with the absorption spectrum of a gold nanoparticle [106]. Copyright (2016) American Chemical Society.

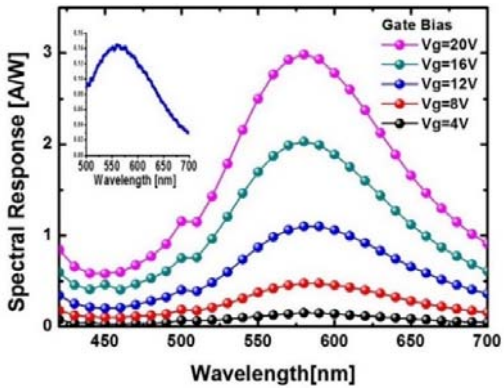

Figure 2.17 Drain current output with different gate voltage bias. Higher gate voltage bias facilitates the plasmon energy transfer and produces amplification of plasmon induced drain current. The inset shows the absorption spectrum of gold NP under the same condition [106]. Copyright (2016) American Chemical Society.

One of the most exciting properties of the plasmon FET is the highly efficient spectral response. We demonstrated amplified plasmonic spectral responses from the plasmon FET using gold nanoparticles as shown in Figure 2.17. The measured data shows that the amplitude of the hot electron induced drain current depends on the gate voltage bias. Under the saturation mode operation of the plasmon FET, the spectral response value, R(A/W) surpassed a value of 3, which implies that an amplification process was involved,

depending on the applied gate voltage bias [108]. This efficient amplification can be explained by an energy band model. Without gate voltage bias (Figure 2.18), the plasmon induced hot electrons can migrate only with diffusion once they have high enough energy to overcome the Schottky barrier. Due to the short mean-free-path in the gold and semiconductor structure, it is difficult to collect plasmon induced hot electrons with a lateral electric field across the Drain and Source (process① in Figure 2.18). When the positive Gate bias is applied to the plasmon FET, there will be a large potential difference between Schottky junction and gate oxide (Figure 2.18-(b)). This internal electric field created by gate bias facilitates electrons to move to the other boundary where the FET channel is located (process③ in Figure 2.18). The migrated hot electrons are seized by the gate voltage, consequently contributing to channel enhancement and allowing more drain current to flow (process④ in Figure 2.18) [106]. Copyright (2016) American Chemical Society.

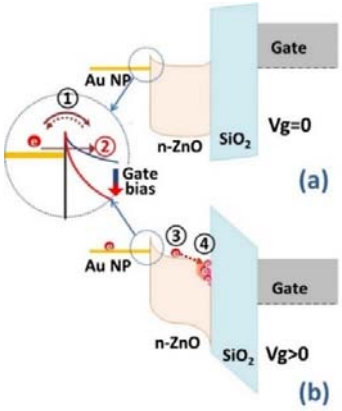

Figure 2.18 Energy band diagram of Au-ZnO plasmon FET (Gate to a gold nanoparticle). (a) 0V Gate bias- only allows thermionic emission (b) Positive Gate voltage bias facilitate the collection of the hot electrons and create thinner barrier structure for an efficient quantum tunneling of hot electrons [106]. Copyright (2016) American Chemical Society.

Therefore, the collected current from the device is proportional to the plasmonic absorption from the gold nanostructure, but is not limited to the number of hot electrons generated in the metal. The importance of the gate bias assisted hot electron accumulation has been studied using devices with different ZnO channel thicknesses and it shows that a stronger electric field is important for efficient plasmon energy detection. If the channel (ZnO layer) thickness is increased the effective electric field from the metal-semiconductor Schottky junction to the electron channel decreases. Therefore, we observed decreased current generation when the ZnO thickness is increased. When the gate bias is applied, there is another interesting hot electron migration mechanism, which is a quantum tunneling process through the thin Schottky barrier wall (process ② in Figure 2.18). The modified potential from the positive gate bias creates not only a drift field to facilitate hot electron migration, but also a thin enough Schottky barrier to allow electron tunneling from the gold nanoparticles to the semiconductor channel [106]. Copyright (2016) American Chemical Society.

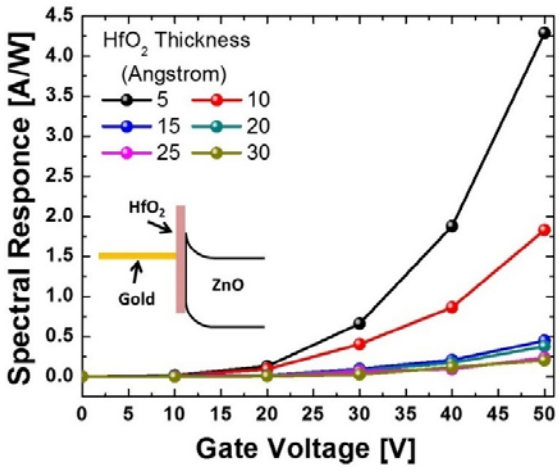

Figure 2.19 Spectral response from the measured drain current from plasmon FETs with various thickness of HfO2 film between gold and ZnO layer. Each data point is taken from the peaks of the spectral responses [106]. Copyright (2016) American Chemical Society.

In order to confirm this tunneling mechanism, we have fabricated devices with an HfO_2-layer (5-30 Å) inserted at the Schottky boundary (between gold and ZnO). The insulating HfO_2 layer inserted devices also show similar drain current amplification as a function of gate voltage bias (Figure 2.19). The probability of quantum tunneling is an exponential function ($T \sim e^{-2\gamma L}$, where, T is the probability of tunneled electrons, γ is the wavenumber inside the barrier and L is the barrier length). The measured drain current was decreased exponentially as the HfO_2 thickness is increased. This result is well matched with our expectation of tunneling induced hot electron migration and confirms quantum tunneling is one of the mechanisms of hot electron migration from the nanostructures to the semiconductor channel. In addition, the strong electric field creates a force to drift the hot electrons to the channel area. The migrated hot electrons increase the carrier concentration in the channel, resulting in higher channel conductivity [105]. We believe that these synergistic processes in the plasmon FET enable a highly efficient spectral response [106]. Copyright (2016) American Chemical Society.

The plasmon FET has several advantages. First, the migration efficiency of plasmon-induced hot electrons into the active layer can be controlled by adjusting the gate bias. As the electric field, increased by gate voltage, attracts more electrons in the current channel through drift current mechanism, the absorption spectrum of the plasmon FET uses plasmonic nanostructures which can be tailored by using different materials and different nanostructure design. Thus, the plasmon FET offers an extremely wide spectral range due to the wavelength tunability that can be used in various applications. Finally, the plasmon FET provides excellent thermal stability because the operating mechanism is independent from the temperature.

Other Works similar to Our Works

Diode based plasmon detectors and 2-dimensional transistor based photo detectors have been studied to generate the plasmon induced hot electron. For the diode based plasmon detectors, nanoantennas for light harvesting and photodiodes for converting light into a current of electrons are incorporated in the same device as shown in Figure 2.20 (b) and (c). Using the optical antenna-diode device, after photons which are coupled into Au nanorods excite the resonant plasmons, the plasmons decay into hot electrons. The energetic electrons overcome the Schottky barrier at the nanostructure-semiconductor interface. The injected electrons result in a photocurrent as shown in Figure 2.20 (a) [35].

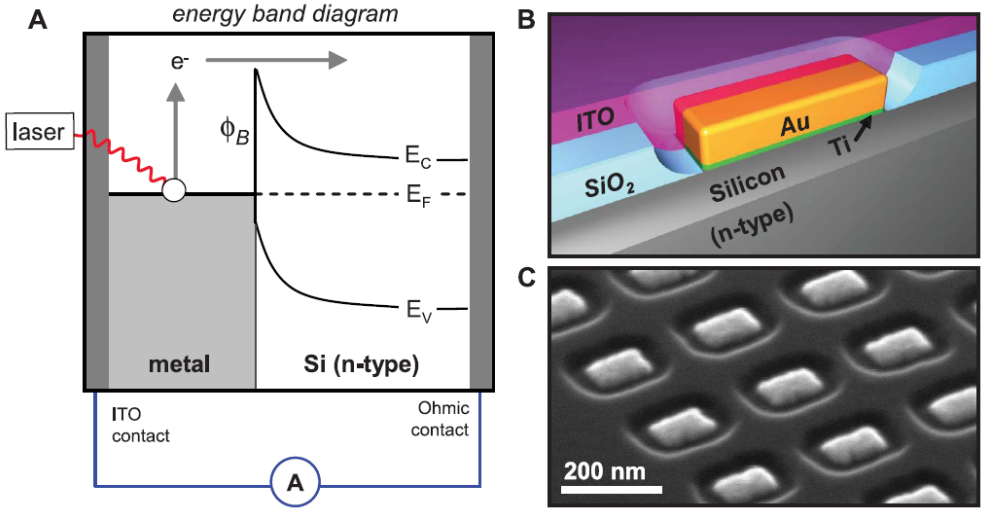

Figure 2.20 An optical antenna-diode for photodetection. (a) Band diagram for plasmonically driven internal photoemission over a nanoantenna-semiconductor Schottky barrier (fB). (b) Representation of a single Au resonant antenna on an n-type silicon substrate. (c) Scanning electron micrograph of a representative device array prior to ITO coating, imaged at a 65° tilt angle [35]. Copyright (2011) American Association for the Advancement of Science.

The 2-dimensional transistor based photo detectors is a Au nanoparticles decorated MoS_2 or graphene transistors. The two-dimensional material such as graphene (a single layer of carbon atoms with a hexagonal arranged lattice) [109] and molybdenum disulfide (MoS_2), have been widely employed for numerous applications in optoelectronics. For example, MoS_2 field effect transistor with Au nanoparticle shows a plasmonic enhancement of the device photocurrent at the plasmonic peak wavelength as shown in Figure 2.21 [110].

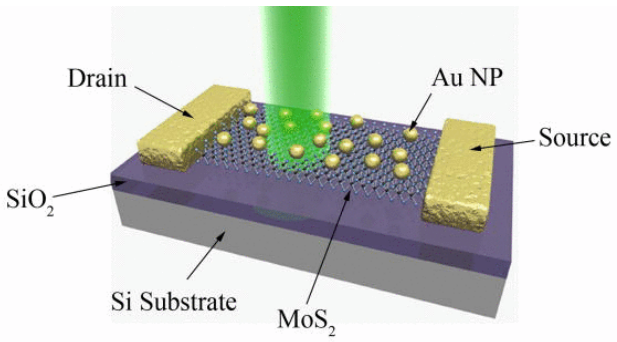

Figure 2.21 Three-dimensional schematic view of the MoS2 transistor. Reprinted from [110], with the permission of AIP Publishing.

The Plasmon FET is the only device that combines two distinct functions in the same structure for photodetection. One is a light harvesting function using nanostructures of noble metals such as gold and silver as a key optical component. The other is an amplification function using thin film transistors. The plasmon FET drastically amplifies the spectral response up to the order of A/W with gate bias using unpolarized light.

Chapter 3: FABRICATION PROCESS AND DEVICE CHARACTERISTICS

This chapter provides the fabrication method of the plasmon FET. We have conducted preliminary studies in order to illustrate the feasibility of constructing the Plasmon FET. The plasmon FET is fabricated by following a typical thin film transistor structure. The unique plasmonic energy detection capability has been added by incorporating a gold nanostructure on the active channel of the FET device. Briefly, the following fabrication procedure was used. We prepared an InGaZnO (IGZO) and ZnO film respectively on top of the doped p-type silicon (<100>, Resistivity: 1 ~ 10 Ω·cm) substrate which has a thermally grown silicon dioxide layer. After substrate preparation, we carried out conventional cleanroom fabrication processes, such as photolithography, metal deposition, and dry/wet etching, to create a thin film transistor. Finally, gold nanoparticles are incorporated by using the thermal reflow process to create self-assembled gold nanostructures. The following sections explain a detailed description of the fabrication and experimental techniques used.

Substrate Preparation

The prepared substrate layers for plasmon FETs are shown in Figure 3.1. Two different active layers of FETs were fabricated with ZnO and IGZO. Both of them were on the Silicon substrate where the doped silicon layer was used as a back gate of the transistor. They were fabricated via the following processes. A 100nm SiO_2 film as an insulator layer for Gate bias was pre-deposited on top of the Si wafer using a thermal oxidation process. Then, a thin n-type ZnO film and IGZO film (with different thicknesses) on top of the thermally grown SiO_2 film were deposited respectively using an RF magnetron sputter

machine to create an active semiconductor channel by applying 90 W of RF power under 6.2-mTorr Ar ambient at room temperature. The deposition rate was modulated to be 8.4nm/min, while the substrate was rotated for uniformity.

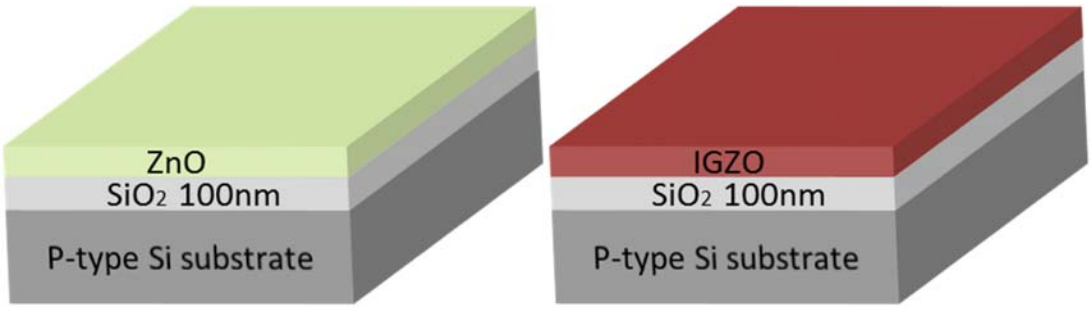

Figure 3.1 Substrate layers for plasmon FET with a ZnO active layer (left) and an IGZO active layer (right). The active layers were grown using sputtering.

Photomask Design

For channel isolation, the active layer was patterned by using a photolithographic process. The photomask for the photolithographic process was designed using the layout2009 software. In this design, two different widths and lengths (100µm by 100µm and 50µm by 40µm) were designed. Source and drain contacts were designed with the same size (200µm by 200µm) but different distances (100µm and 40µm) between the source and drain which are shown in Figure 3.2. So, we have two different W/L ratios (1 and 5/4) for FET structures. We also designed openings on top of the patterned channel for gold nanoparticle (NPs) incorporation. This opening is isolated from drain and source connections because we want the gold NPs to be electrically isolated from source and drain electrodes. We considered the position of the openings. One device has the fabricated gold

NPs near the source contact while the other one has the gold NPs near the drain contact as shown in Figure 3.3.

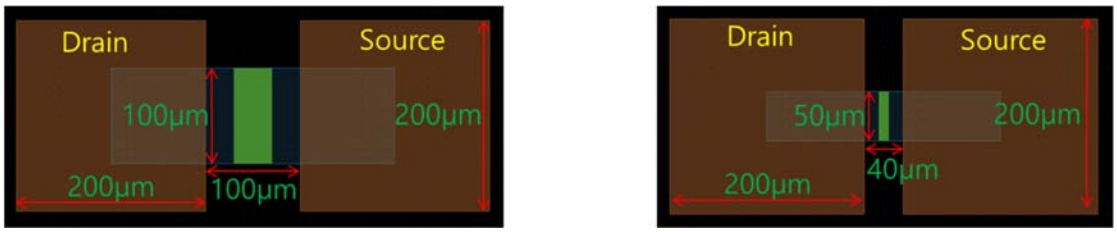

Figure 3.2 Mask design for the plasmon FETs with two different W/L of gold NPs. 100μm by 100μm (left) and 50μm by 40μm(right).

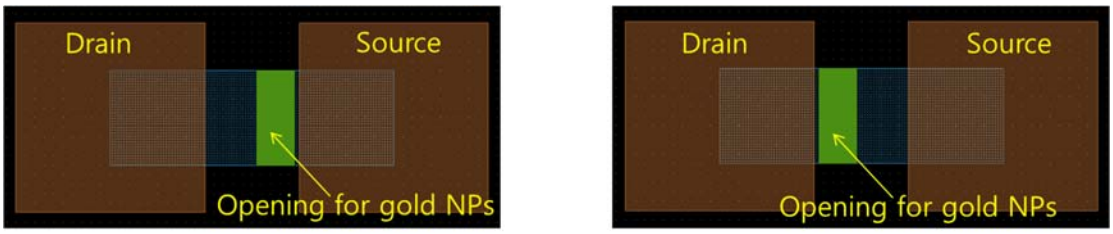

Figure 3.3 Mask design for the plasmon FETs with different positions of gold NPs. One device has the fabricated gold NPs near the source contact (left) while the other one has the gold NPs near the drain contact (right).

After this design, the photomask was made using a μPG101 mask maker. The following steps are used to make the mask:

1. Exposing using a μPG101 mask maker
2. Developing (AZ 400K 1:4, 1 minute)
3. Cr Etching (Cr Etch 1020AC, 2 minutes)
4. Photoresist Removing (Acetone)

Photolithography and Wet Etching

ZnO layer and IGZO layer were patterned using typical photolithography and wet etching processes with diluted HCl solution (1%) and (2%) respectively. Figure 3.4 shows the structures of the ZnO thin film (left) and the IGZO thin film (right) after active layer patterning and etching. The following steps are used to pattern ZnO and IGZO layers:

1. Photoresist (PR, AZ5214) Spin coating (4000rpm / 30 seconds)
2. Heat treatment (1minute / 97°C)
3. Exposing (3 seconds)
4. Developing (AZ 917 MIF, 30 seconds)
5. ZnO Etching (HCL:DI / 1:99) for 1 ~ 2 seconds depends on ZnO thickness

   IGZO Etching (HCL:DI / 2:99) for 60 seconds depends on IGZO thickness
6. Photoresist Removing (Acetone)

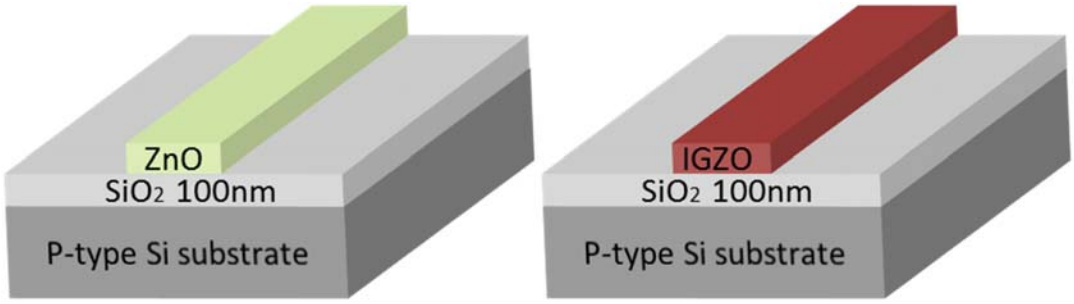

Figure 3.4 Active layer patterning of ZnO and IGZO**.**

After active layer patterning, the following procedures were used to create source and drain electrodes.

1. Photoresist (PR, AZ5214) Spin coating (4000rpm / 30 seconds)
2. Heat treatment (1minute / 97C°)
3. Exposing (3 seconds)

4. Developing (AZ 917 MIF, 30 seconds)

6. Metal deposition (Cr 5nm / Au 80nm) using an electron beam evaporator

7. Lift-off process (Acetone)

Cr / Au layers were deposited on the photoresist patterned substrate using an electron beam evaporator to create Drain and Source electrode contacts on the active layer. After the lift-off process, the device becomes a fully functional field effect transistor (FET) as shown in Figure 3.5. Then, we carried out a characterization of the electrical properties of the FET device before gold NPs incorporation on the active layer. Figure 3.6 shows microphotographs of the final fabricated FETs on a silicon substrate.

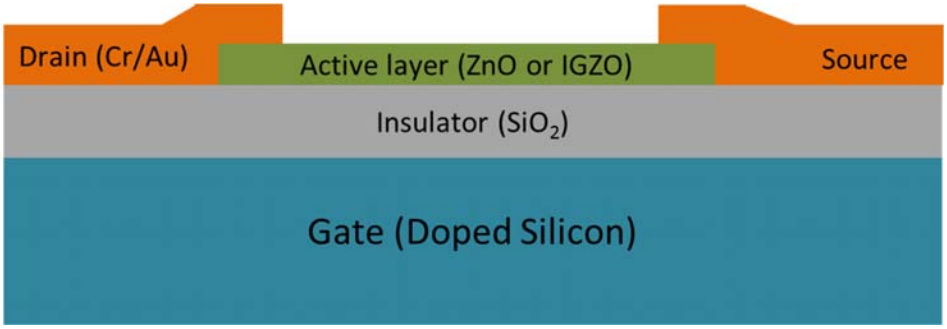

Figure 3.5 Schematic diagram of a fully functional field effect transistor.

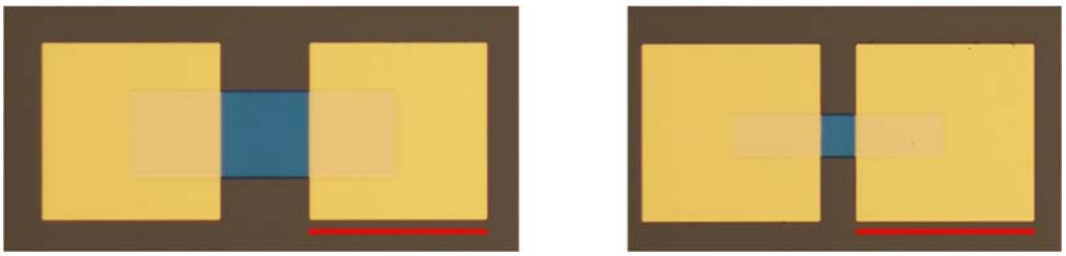

Figure 3.6 Microscopic pictures of fabricated thin film transistors with W/L 1/1 (left) and W/L 5/4 (right) on a silicon substrate. Scale bar is 200µm.

I-V Characteristics of Fabricated FETs

Figure 3.7 shows the I-V characteristics of fabricated thin film transistors with an IGZO channel (left) and a ZnO channel (right). The fabricated FETs have typical transistor characteristics. The measured drain current shows typical n-type thin film transistor characteristics.

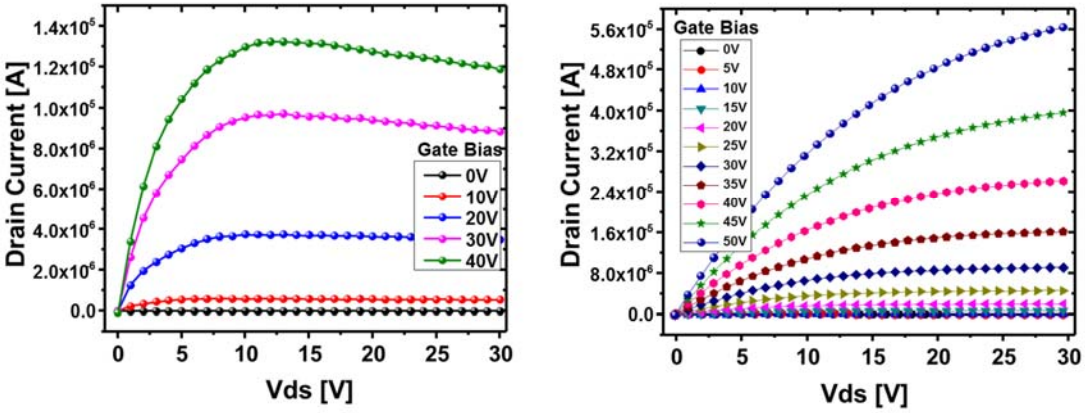

Figure 3.7 I-V characteristics of fabricated FETs with IGZO channel (left) and ZnO channel (right) [102]. Copyright (2016) Society of Photo Optical Instrumentation Engineers.

Gold Nanoparticles Incorporation

Finally, the gold thin film was deposited on top of the active layer using the electron beam evaporator. The opening area for gold NP self-assembly was 40 μm × 100 μm as shown in Figure 3.8 (a) ~ (c). To analyze the effect of gold NPs position on the plasmon FET, we fabricated three devices that have different opening positions for gold NPs. The first device has the deposited gold thin film near the source contact as shown in Figure 3.9 (a) The second device has the film in the middle of the active layer as illustrated in figure 3.9 (b). Finally, the third one has the gold deposition close to the drain contact as depicted in figure 3.9 (c). The details of the analysis for the effect of the position will be discussed

later in chapter 4. Then, a thermal reflow process creates self-assembled gold nanoparticle structures on the thin film. The reflow method employs a 5nm thin gold film which then undergoes 300°C of heat treatment for 10 minutes.

Figure 3.9 (d) shows the SEM picture of the gold NPs on top of the active layer with the thermal reflow method. Based on the SEM analysis, the size of gold nanoparticles is in the range of 5- 30nm. The shape and the size distribution of gold nanostructures play a significant role in the plasmon FET. The size distribution of gold NPs could depend on substrate condition, metal film thickness, and the thermal reflow condition. We have tested several reflow conditions with different thicknesses of the deposited gold thin film and the different substrate to investigate and analyze the size and the shape of gold nanostructures. Further investigations have been carried out, and the results are explained in chapter 4.

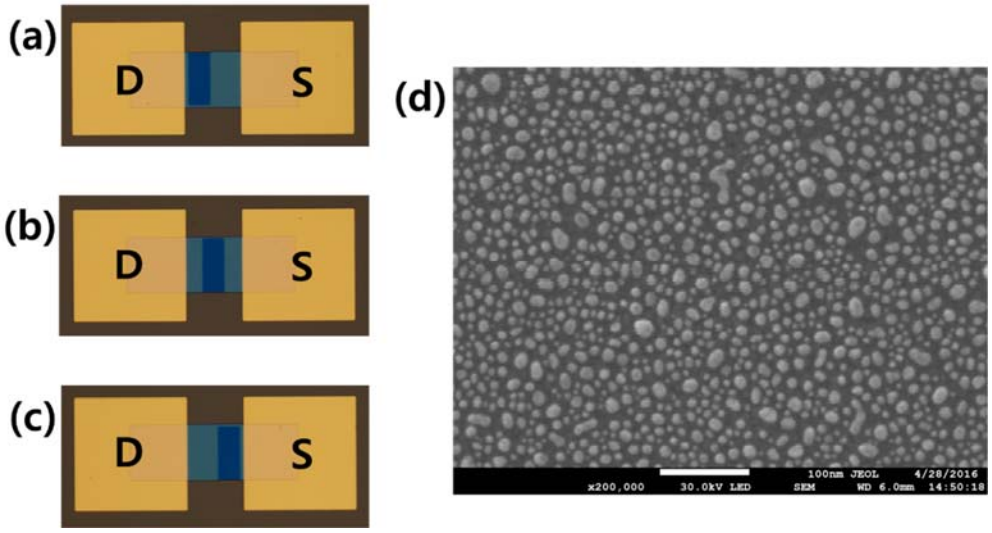

Figure 3.8 Microscopic pictures of fabricated plasmon FET with the different opening positions for gold NPs which are near the drain contact (a), in the middle of the active layer (b), and near the source contact (c). SEM picture of incorporated gold NPs in the plasmon FET using thermal reflow method (d).

Summary

The fabrication process of plasmon FET was explained in this chapter. The plasmon FET can be fabricated using conventional microfabrication. The field effect transistors which used ZnO or IGZO as an active layer were successfully fabricated, and the I-V characteristics showed that the fabricated FETs had a typical transistor response. The gold nanoparticles on the active layers were made using the thermal reflow process at 300°C with gold thin films. We confirmed that the fabricated gold NPs have the size distribution of 5nm to 30nm using SEM imaging. Also, we fabricated three devices that have different opening positions for gold NPs to investigate the effect of the position of gold NPs on the plasmon FET.

Chapter 4: EXPERIMENTAL RESULTS

In this chapter, the properties and characteristics of the plasmon FET will be discussed with different experimental setups. We will start this chapter with measuring the spectral responses of the plasmon FET using a lock-in amplifier. We fabricated three devices that have different gold NPs positions. The spectral responses of all three plasmon FETs were measured. By carrying out these experiments, we could understand how to increase the spectral response efficiently according to the position of gold NPs between source and drain. We confirmed the results by simulating a plasmon FET model.

The spectral response by the plasmon effect can be tuned by the shape, size and so on. The nanoparticles sizes could be controlled by using different substrates, process conditions or metal film thicknesses. We have tested several reflow conditions with various thicknesses of the deposited gold thin film and different substrates to investigate and analyze the size and the shape of the gold nanostructures. However, it was too difficult to control the size and the shape of metal nanostructures.

Measurement Setup to Obtain the Spectral Response of Plasmon FET

In the following section, the spectral response of the plasmon FET will be shown. Spectral response is a ratio of the current generated by the device to the power incident on it as a function of wavelength. The spectral response of the plasmon FET depends on plasmon-induced hot electrons inside the gold nanoparticles.

For the spectral response of the plasmon FET, two Keithley 2400 source meters are used to provide the Gate-Source and Drain-Source voltage biases same as a field effect transistor or thin film transistor. The spectral response measurement is carried out using a

monochromatic light source, as the optical characteristics of the device are dependent on wavelength. A SpectraPro 275 monochromator using an Oriel quartz tungsten halogen lamp delivers monochromatic light through a fiber-optic cable onto the sample with controlled angles at the probe station. For the spectral response calculation, the light power was measured with its wavelength using a Keithley 6485 Picoammeter with a Thorlabs FDS-1010CAL calibrated silicon photodiode and a Thorlabs FDG-05 calibrated germanium photodiode. Optical filters (FW102C filter wheel system) are used to suppress the second harmonic signals generated by the grating inside the monochromator.

An SR830 lock-in amplifier and the mechanical chopper which is controlled by SR540 chopper controller are used to detect and measure very small signals. The operation principle of the lock-in amplifier is known as phase-sensitive detection technique to pick up small signals obscured by enormous noise. The chopper modulates the incoming light to the monochromator. Noise signals do not affect the measurement because they make a reference frequency and reject noise with frequencies other than the reference frequency. By using the modulation frequency of chopper and a lock-in amplifier, we can extract only the optical response of our device. So, we can calculate the current enhancement by optical excitation in the plasmon FET. The current improvement that is collected by the modulated light illumination can be measured by indirectly since the device has a significant voltage bias across Drain and Source electrodes. A series resistor to the Drain-Source bias is used to produce the voltage value, and it is converted to the current value.

A customized LabView program controls two source meters, the monochromator, and the lock-in amplifier for automated computerized measurements. Figure 4.1 shows the schematic of the measurement setup.

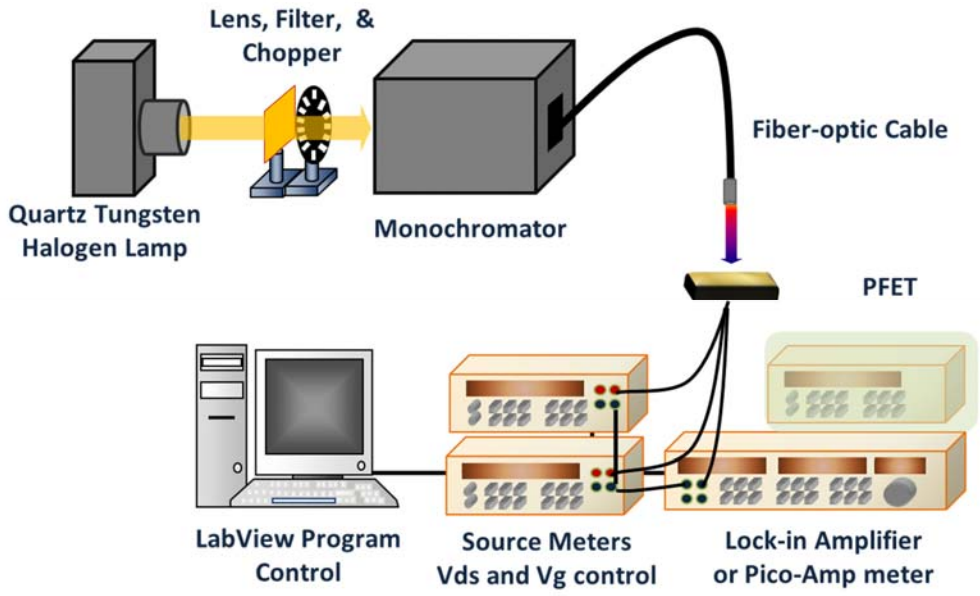

Figure 4.1 The schematic of the measurement setup to obtain a spectral response.

Spectral Response of Plasmon FET

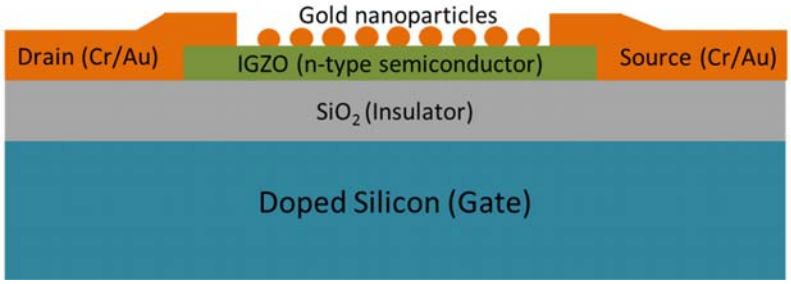

Figure 4.2 Schematic of the plasmon FET structure with gold nanoparticles on top of the IGZO layer.

The plasmon FET is fabricated using IGZO thin film transistor (TFT) (W/L= 100µm/100µm). A doped p-type Silicon substrate serves as a back gate, and an n-type IGZO thin film on SiO_2 insulator acts as an active semiconductor layer. Gold nanoparticles are incorporated into the IGZO TFT to detect the plasmonic energy as shown in Figure 4.2.

The gold nanoparticles are the source of injected hot electrons. The spectral response of the plasmon FET, with gold nanoparticles on the IGZO active layer, when applying 20 volts as a gate-source bias and 10 volts as a drain-source bias is shown in Figure 4.3. The plasmon energy can be amplified by increasing the gate bias increasing the channel conductivity. As we discussed in Chapter 2, the plasmonic absorption produces hot electrons in gold nanoparticles. The generated hot electrons can overcome the Schottky barrier and diffuse from gold nanoparticles to the IGZO active layer. This migration process increases the number of electrons in the IGZO active channel, contributing to the channel conductivity and drain current. The enhanced drain current depends on the number of diffused hot electrons. The plasmon FET converts localized surface plasmon energy to electrical charges and signals.

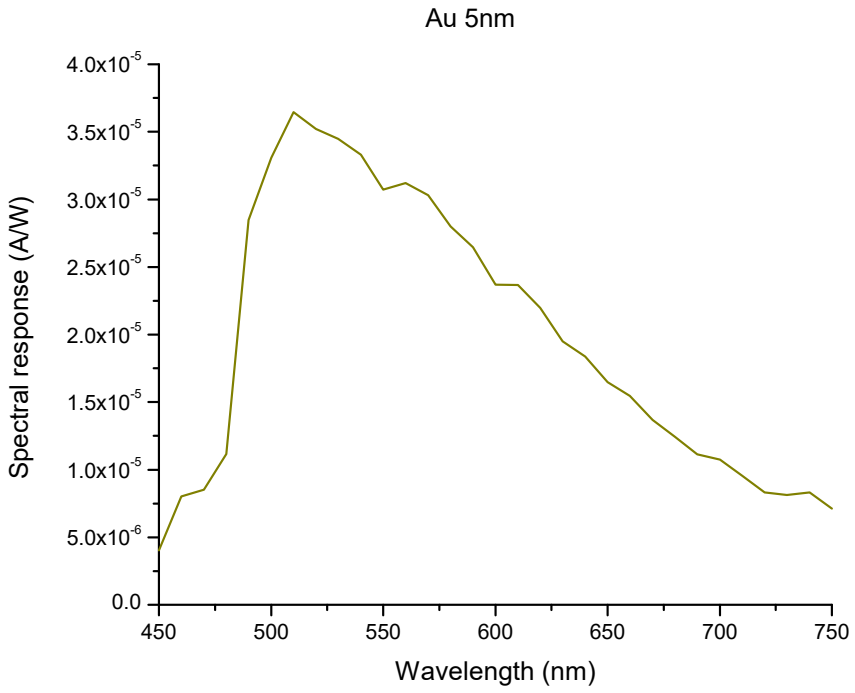

Figure 4.3 Spectral response of the plasmon FET with gold nanoparticles on the IGZO active layer when applied 20 volts as a gate-source bias and 10 volts as a drain-source bias.

Analysis of Gold NPs Area and Position on Plasmon FET

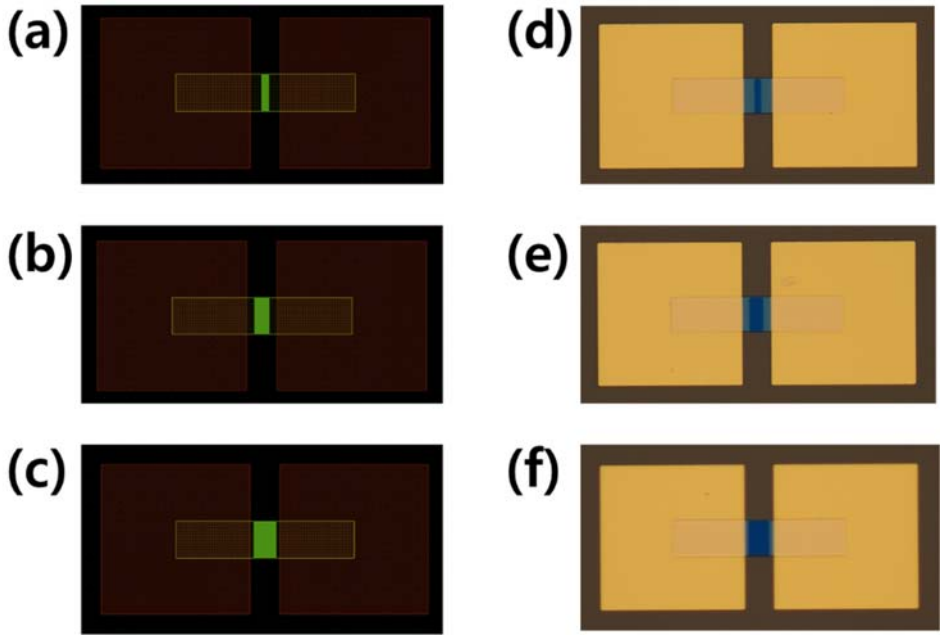

Figure 4.4 The layout designs of the plasmon FETs (W/L= 50μm/40μm) with three different sizes of the gold nanoparticles area (10μm × 50μm (a), 20μm × 50μm (b), and 30μm × 50μm (c)) and the microscopic pictures of the fabricated plasmon FET (10μm × 50μm (d), 20μm × 50μm (e), and 30μm × 50μm (f)).

One of the important aspects of the plasmonic hot electron detection is a keen understanding of the generation of the hot electrons. In the plasmon FET structure, the gold NPs are the source of hot electrons. Herein, we analyzed the effects of area, and position of the gold NPs in the plasmon FET and how these parameters affect the efficiency of plasmonic hot electron collection. First, we analyzed the effects of area of the gold nanoparticles in the plasmon FET and how the parameter enhances plasmon-induced hot electrons collection. We designed and fabricated plasmon FETs with three different sizes of the gold nanoparticles area (10, 20, and 30μm × 50μm) as shown in Figure 4.4. We designed gold NPs area located at the center of the active layer (W/L= 50μm/40μm). By

increasing the area of gold NPs, there are more sources of hot electron generation. The drain current in the plasmon FET increased due to more sources of hot electron depending on the area of gold nanoparticles. The generated photocurrent is directly proportional to the area of gold nanoparticles as shown in Figure 4.5.

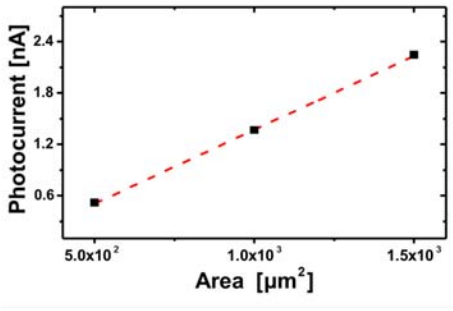

Figure 4.5 The photocurrent of the plasmon FETs with the three different areas (10, 20, and 30μm × 50μm) of gold nanoparticles at the plasmonic resonance frequency.

Second, we fabricated two devices with different positions of gold nanoparticles to analyze the effect of the position of gold nanoparticles in the plasmon FET. One device has the incorporated gold nanoparticles near the drain contact, and the other device has the gold nanoparticles near the source contact as shown in Figure 4.6.

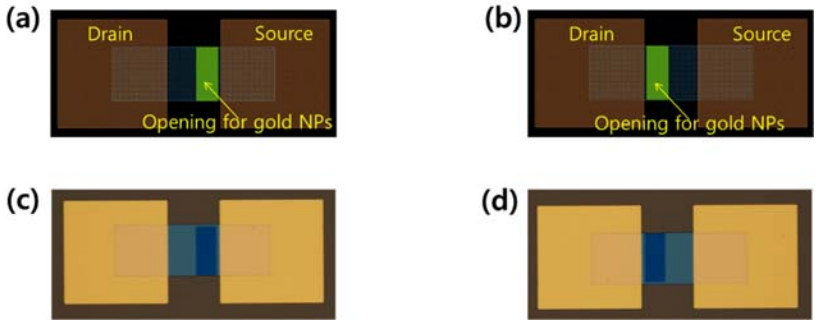

Figure 4.6 The layout designs of the plasmon FETs (W/L: 100μm/100μm) with the different gold nanoparticles positions that are near the source contact (a), and near the drain contact (b). Microscopic pictures of fabricated plasmon FETs with the different gold nanoparticles positions that are near the source contact (c), and near the drain contact (d).

The spectral responses of two plasmon FETs were measured at the resonance peak wavelength, and we normalized results. The spectral response of the plasmon FET with the gold nanoparticles near the source contact was 31% higher than the value of the device with gold nanoparticles near the drain contact as shown in Figure 4.7. This could be explained by the fact that there is a stronger vertical electric field near the source contact. It implies the importance of the hot electron transport after the transfer from metal to semiconductor. Even though the plasmon FET uses hot electrons for amplified drain current, it shows that an efficient hot electron transport is an important design consideration for the hot electron detector.

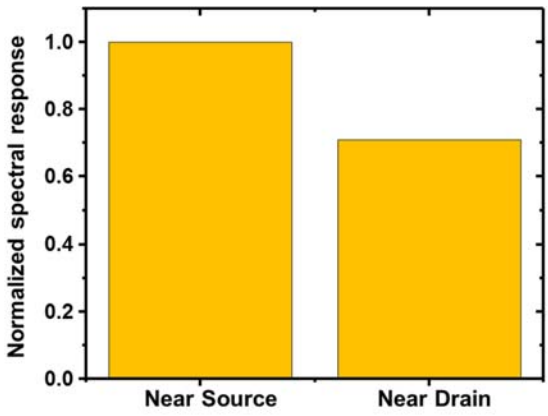

Figure 4.7 The normalized spectral response of two plasmon FETs with gold nanoparticles near the source contact (left) and the drain contact (right) when applied 15 volts as gate-source bias and 20 volts as drain-source bias.

Also, we simulated the IGZO TFT using SILVACO software with 15 volts of gate bias and 20 volts of drain bias to confirm the effect of the position of gold nanoparticles. Figure 4.8 shows the vertical electric field inside the IGZO TFT. The potential (1.82×10^5 V/cm) of the vertical electric field near the source contact is stronger than the value (1.2×10^5 V/cm) near the drain contact. The hot electron transport after the transfer from metal

to the semiconductor is necessary to detect the hot electron because the plasmon FET uses hot electrons for enhanced drain current. The plasmon-induced hot electrons near the source can easily reach the current channel due to the higher electric field and increase the drain current. Thus, the position parameter for an efficient hot electron transport is crucial because of the gradient potential of the electric field in the FET channel between the drain contact and the source contact.

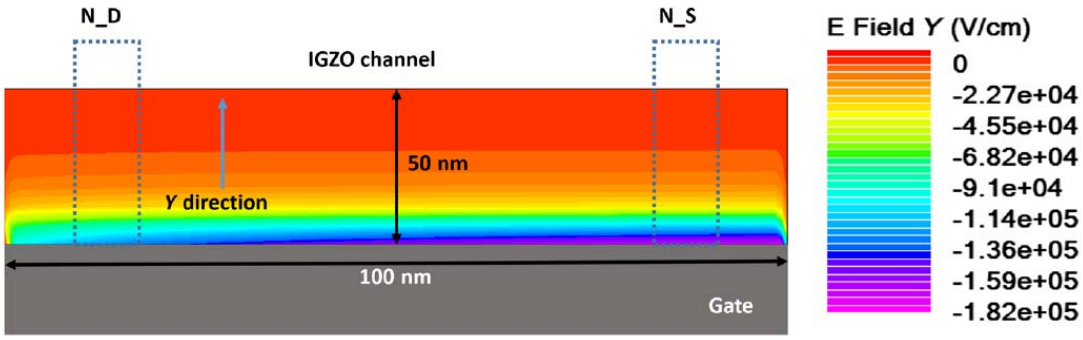

Figure 4.8 The electric field distribution in a vertical direction inside the IGZO TFT when applied 15 volts as gate bias and 20 volts as drain bias [102]. Copyright (2016) Society of Photo Optical Instrumentation Engineers.

However, when there is no applied gate bias voltage to the plasmon FET, the device that has gold NPs near the drain has a higher spectral response because the induced plasmonic hot electrons travel a shorter distance to reach the drain contact in comparison with the device that has gold NPs near the source. Further measurements on the plasmon FET with zero gate bias voltage and 20 V drain bias also confirm that the plasmonic photocurrent of the device that has gold NPs near drain is 84 pA while this value decreases to 30 pA when the gold NPs are located near source contact. Those simulation and experimental results confirm that there should be minimized path for hot electron transport

in a semiconductor area, and any built-in electric field in the device will facilitate the collection of hot electrons.

Fabrication of Gold NPs Changing Metal Film Thicknesses, Substrates, and Thermal Reflow Conditions

To control the size and shape of gold nanoparticles in the plasmon FET, three samples were fabricated by changing the thickness of the gold thin film: 3nm, 5nm, and 7nm thicknesses of the gold film were deposited on IGZO layer, and self-assembled gold nanostructures were obtained after heat treatment at 300°C for 10 minutes.

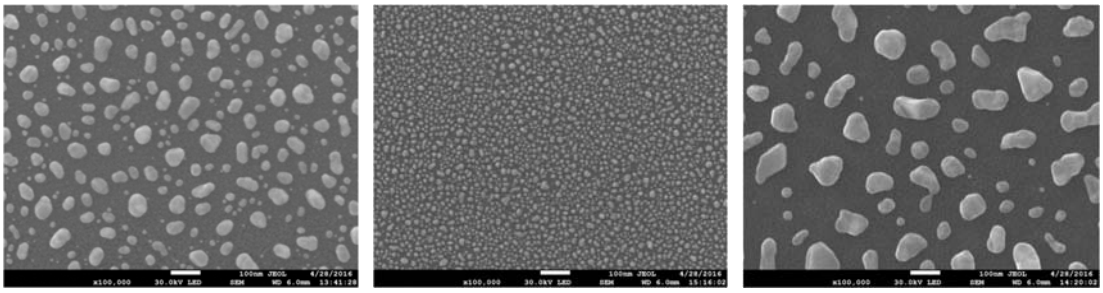

Figure 4.9 SEM images of gold nanoparticles obtained with a 3nm (left), 5nm (center), and 7nm (left) gold film in thickness after heat treatment at 300°C for 10minutes. Scale bar is 100 nm for all images [102]. Copyright (2016) Society of Photo Optical Instrumentation Engineers.

Figure 4.9 shows the SEM images of gold nanoparticles obtained from 3nm (left), 5nm (center), and 7nm (right) gold thin film after the thermal reflow method. Based on the SEM analysis, the size of the self-assembled gold nanostructures is not directly proportional to the thickness of the gold film before the thermal reflow process. The gold nanoparticles with a 5nm gold film show minimum size on average and narrow size distribution after heat treatment 300°C for 10 minutes. We can get the size of gold

nanostructures over 200nm length using a 7nm gold film. However, increasing the particle size made interparticle distance increase and resulted in a lower density of gold nanoparticles that reduced the spectral response of the plasmon FET as well. Thus, the density is a major factor to detect hot electrons.

We fabricated several plasmon FETs changing the thermal reflow conditions to analyze the size depending on heat treatment temperature and time. When we increased time and temperature for the thermal reflow methods, the gold nanostructures were connected to others like a dispersed liquid as shown in Figure 4.10.

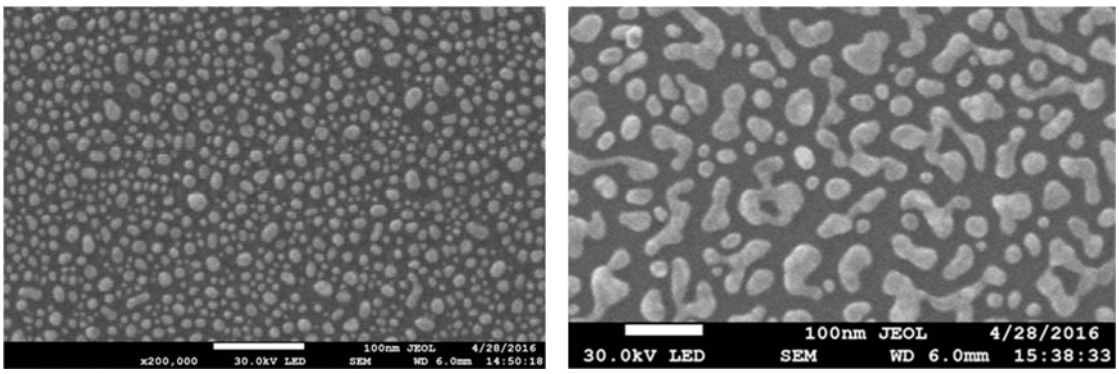

Figure 4.10 SEM images of gold nanoparticles obtained with a 5nm gold film in thickness after heat treatment at 300°C for 10minutes (left) and at 300°C for 12minutes (right).

We have studied the surface effect of substrates which affects the shape of gold nanostructures. First, a thin film of IGZO was deposited on the SiO_2 of the silicon wafer using RF sputter. Figure 4.11 shows the SEM micrographs of the IGZO surface (left) and the gold nanoparticles (right) on the IGZO substrate that was made after 300°C heat treatment for 10 minutes with a 5nm thick gold film. Second, vanadium dioxide (VO_2) substrate was prepared, and Figure 4.12 shows the SEM micrographs of the VO_2 surface (left) and the gold nanoparticles (right) on the VO_2 layer using the same thickness of the

gold film and thermal reflow process as above. Finally, a flat silicon wafer was used to incorporate the gold nanoparticles on it after removing SiO_2. SEM micrograph of gold nanoparticles after the same reflow process is shown in Figure 4.13. We found that the shape and size of gold nanostructures are strongly related with the surface roughness, but the particles on the flat surface can contain a wide variety.

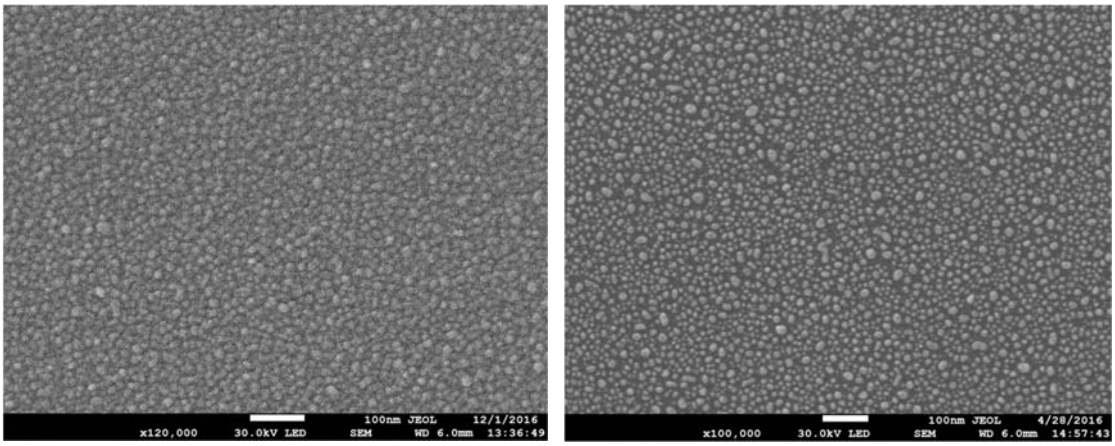

Figure 4.11 SEM image of IGZO surface (left) and gold nanoparticles on IGZO surface.

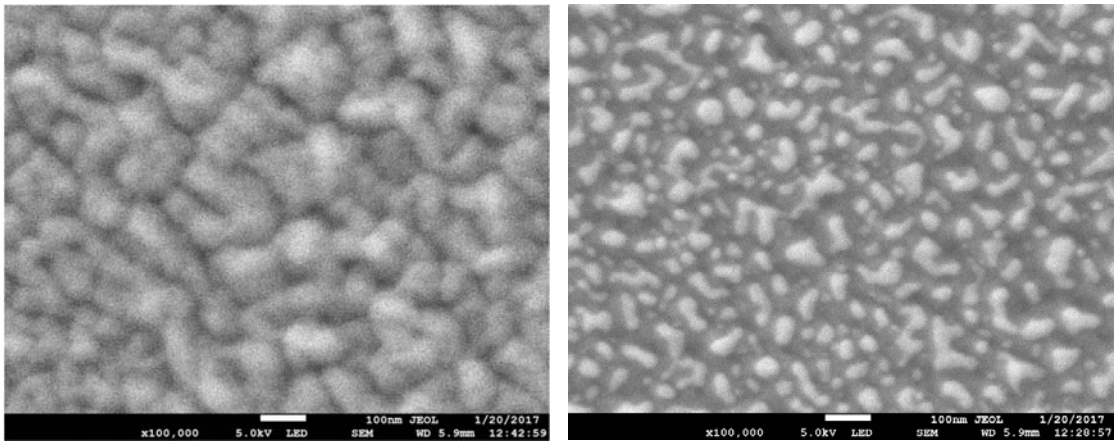

Figure 4.12 SEM picture of the VO_2 surface (left) and gold nanostructures on the VO_2 surface.

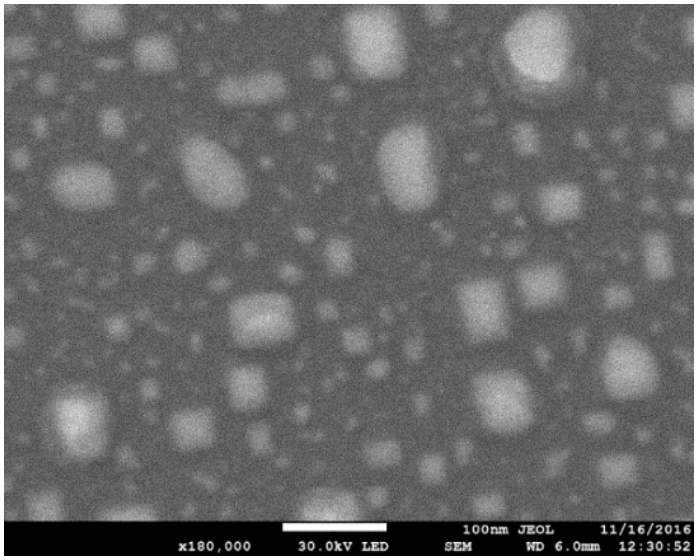

Figure 4.13 SEM micrograph of gold nanoparticles with a 5nm gold film on Silicon wafer at 300°C heat treatment for 10minutes.

In this chapter, we discussed the mechanisms of plasmon hot electron collection, transfer, and transport properties using various plasmon FET structures and internal band structures. For an efficient hot electron energy collection, the plasmonic absorption needs to be maximized with denser metallic nanostructures. We believe that the optimized and engineered nanostructures can increase plasmonic light harvesting. Our experimental study along with the simulation model emphasizes the importance of internal electric fields and short hot electron travel distance for an efficient carrier transfer and transport in hot electron devices. This work suggests a photovoltaic device structure with a strong internal potential that allows efficient hot carrier transport can increase hot electron conversion efficiency. Moreover, self-assembled gold nanostructures using the thermal reflow method are influenced by the temperature, the annealing time, the film thickness and the surface profile of the substrate.

Chapter 5: FABRICATION OF PLASMON FET USING NPGS

In Chapter 4, we found that it is too difficult to control the size distribution of nanostructures using the thermal reflow method. This chapter provides the manufacturing method of the plasmon FET which can create different sizes and shapes of nanostructures using Nanometer Pattern Generation System (NPGS). After TFT preparation, nanostructures were fabricated on the active layer using standard cleanroom and electron-beam lithography techniques. We carried out scanning electron microscope (SEM) lithography in the cleanroom. The NPGS is an SEM based lithography system. The fabrication processes include Pattern Design, Polymethyl Methacrylate (PMMA) resist spin coating, Exposure without mask, Development, Metal deposition, and Lift-off processes. Finally, gold nanostructures are incorporated by using the thermal reflow process for crystallization. The following sections will provide a detailed description of the fabrication and experimental techniques used.

Pattern Design of Nanostructures

The nanostructures were fabricated onto the active layer by an Electron Beam Lithography process. We designed a simple device geometry consisting of a metal nanostructure array to incorporate on the ZnO active layer using the Layout2009 software as shown in Figure 5.1 (a). In this design, nanostructures of 300nm diameter were designed in the 80μm by 100μm area as shown in Figure 5.1 (b). Adjacent nanorods were spaced 200nm apart for the device. The layout2009 design file (extension: dxf) was imported using the DesignCAD v21 software. The imported design file was saved as (Not for NPGS

Patterns), and then we saved the file to Current NPGS Project. To complete the design, the patterned area was selected and dashed line type was applied to the entire drawing. Different sizes and shapes were also designed including nanorod and nanowire arrays. The patterns are transferred onto the active layer without a mask by direct write electron beam inside the SEM chamber.

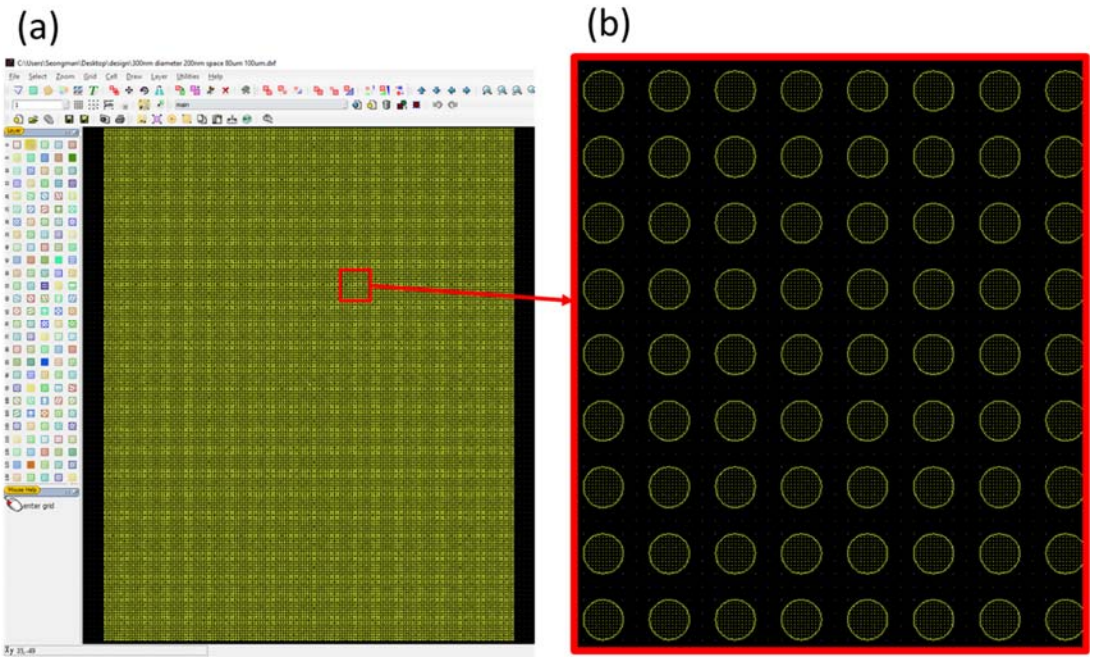

Figure 5.1 Design for nanodisk pattern of 300nm diameter and 200nm space in 80μm by 100μm area using Layout2009 software.

PMMA Resist Spin Coating

Unlike conventional photolithography, we use polymethyl methacrylate (PMMA) resist for electron beam lithography. PMMA is a versatile polymeric material that is well-suited for many imaging microelectronic applications. PMMA resists are dissolved PMMA polymers, the two most common solvents are chlorobenzene and anisole. Anisole is often

used with PMMA because it is the less hazardous solvent of the two. PMMA is the most commonly used photoresist for direct write e-beam as it offers high-resolution and is easy to handle. Spin coating is used for evenly spreading the PMMA resist on the thin film transistor surface. PMMA resist produces low defect surfaces over a broad range of film thicknesses. We used 2% 950k PMMA with a molecular weight of 950,000 dissolved in anisole. The concentration of the PMMA affects the thickness of the PMMA after spinning. We have used 2% by weight in anisole, which results in about a 100 nm thick film when rotated at 1000 rpm, and about 50 nm thick when spun at 4000 rpm. The resist thickness is determined primarily by the resist viscosity and rotation speed. The spin rate versus film thickness curves displayed in Figure 5.2 provides the information required to select the appropriate PMMA spin speed needed to achieve the desired film thickness.

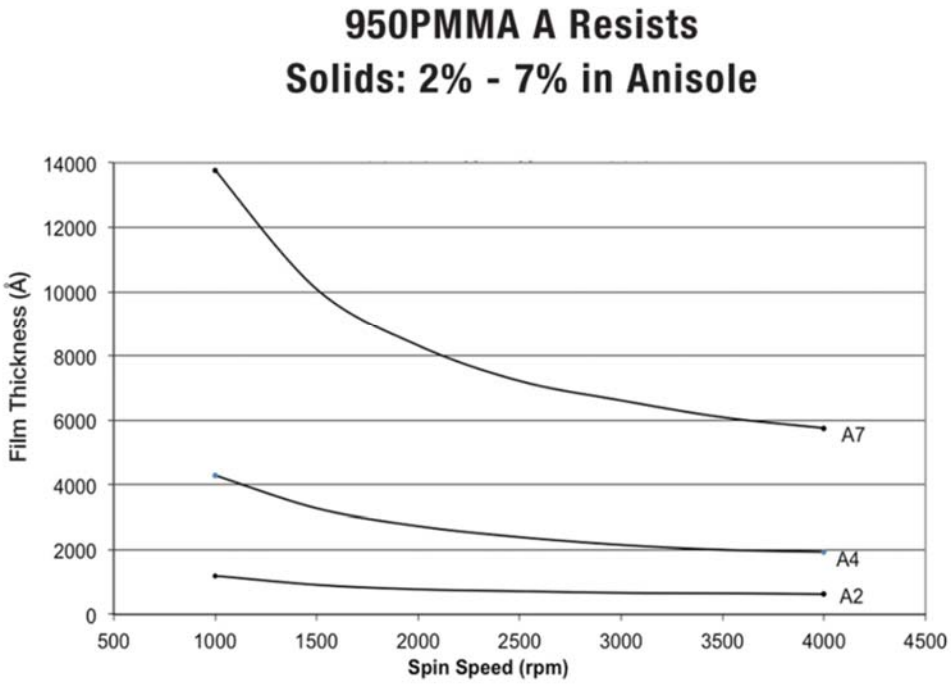

Figure 5.2 The film thickness vs. spin-speed curves of 950k PMMAs [111]. Copyright (2001) MicroChem Corp.

Later we will deposit no more than 30nm thick metal film on the patterned resist by using E-beam evaporator. The evaporated metal should be about 1/3 of the thickness of the resist layer. So, the resist thickness should be around 90nm which requires a spin speed of 1500 rpm. A pre-spin was used to spread the resist evenly over the wafer before the final spin speed produces the final thickness. We have used a pre-spin of 500 rpm for 3 seconds. The following steps are used for PMMA resist spin coating:

1. Substrate Preparation: Acetone −> Methanol −> Isopropanol or DI water
   −> dry with N_2 gun −> hot plate at 120°C for 5 minutes −> O_2 plasma cleaning
2. Spin coating: pre-spin, 500 rpm for 5 seconds −> 1500 rpm for 50 seconds
3. Pre-Baking: at 180°C for 60 seconds

Electron Beam Exposure using SEM and NPGS

Electron beam exposure using SEM and NPGS causes the scission of the PMMA polymer chains and it reduces the molecular weight and increases the development selectivity. The number of electrons exposed on the PMMA-resist is around 50μC/cm2 to 500μC/cm2 to break the PMMA polymer chains. JSM-7100F Field Emission SEM was used to obtain high magnification for the study of nanostructures by a microscopy method with an electron beam rather than light as shown in Figure 5.3. The SEM has the magnification of 10 to 1000000x and accelerating voltage 2 to 30 kV.

Figure 5.3 JSM-7100F Scanning Electron Microscope.

We use a faraday cup to measure the electric current of the SEM electron beam. It is a conductive cup which catch electrons in a vacuum. The current can be measured and used to determine the number of electrons hitting the bowl [112]. We also used a blanker to make pattern writing more convenient and improve the results for patterns. NPGS can control the SEM to move the beam fast enough between pattern elements to avoid unwanted exposure. However, the scan coils of the SEM frequently require a settling time after large changes in the beam position. Moreover, the beam is always bombarding the sample when the stage is moved between exposure locations. This causes unwanted exposure. With the beam-blanker, an overexposure at the start of each pattern element and unwanted hitting between exposure sites can be avoided allowing the beam to settle and move. The following steps are used for electron exposure with SEM and NPGS:

1. Loading the coated FET in the specimen exchange airlock chamber.
2. Vacuum the specimen exchange airlock chamber
3. Load the coated FET in the specimen chamber

4. Vacuum the specimen chamber (9.6 X e-6)

5. Set acceleration voltage to 30kV, probe current to 1, Filament current: 2.24A

6. Adjust the Z-axis of stage and the working distance to 6mm

7. Adjust Wobbling, Focusing, Stigma X and Stigma Y

8. Clean lens twice

9. Measure the electric current of the SEM electron beam (absorb current)

10. Focus and align in Fine 2 mode with a magnification of 1,400x

11. Beam blanker on and NPGS mode

12. Execute Run Files using NPGS

The Z distance is from the top of the specimen holder to the backscatter detector. The working distance WD is the distance from the lens to the point of focus on the specimen on the stage.

Development, Metal Deposition and Lift Off (Remove PMMA)

The electron exposure will break many of the bonds of large PMMA molecular chains, and the broken smaller chains will be more soluble in the developer than the unexposed chains. So, the exposed areas will be removed during development. However, the resist is not removed during the exposure to the beam. Blends of MIBK and IPA are used as a developer for the PMMA resist. MIBK is the solvent and active ingredient. It controls the solubility and swelling of the resist. Moreover, IPA is the alcohol (non-solvent). PMMA is usually developed in the following MIBK:IPA ratios: 1:1, 1:2 or 1:3. Higher amounts of MIBK are more aggressive and give higher throughput. However, higher amounts of IPA are less aggressive and designed for higher resolution and low sensitivity. So, we used

MIBK:IPA in the ratio of 1:3 to get high resolution. Developing time was optimized with the baking time, thickness of resist, and developer. The device was immersed in DI water immediately following developing and dried by an N_2 blow dry to prevent scumming. The following steps are used for developing:

1. Developing the device in MIBK:IPA in the ratio of 1:3 for 60 seconds
2. Rinse in DI water, N_2 blow drying, and O_2 plasma cleaning

The typical process is to evaporate a metal after development with the sample. We deposited gold of 25nm in thicknesses onto the patterned resist using an electron beam evaporator. After metal deposition, lift-off step was conducted to remove the excess metal by using Remover PG or conventional cleanroom solvents, such as acetone, photoresist thinner, or positive photoresist removers. We put the device in acetone at room temperature which dissolves the PMMA resist causing the metal from the unpatterned area to float away. We sprayed the acetone onto the device and used the ultrasonic cleaner more aggressively liftoff unwanted metal. Afterwards, only the metal deposited onto the device in the patterned areas remained. PMMA and copolymer resists can be removed by using Remover PG or conventional cleanroom solvents, such as acetone.

Challenges in Fabrication of Nano Patterns

This dissertation introduces a new process developed in the BioNIUM Nanofabrication Facility and we are trail blazing new technical and scientific challenges. Using very short-wavelength electrons for PMMA irradiation, an excellent resolution can be achieved. The completed fabrication of nanoscale particles less than 25nm is shown in

Figure 5.4 (b) and the resolution of SEM reached a few nanometers to obtain the nanoparticles as shown in Figure 5.4 (a).

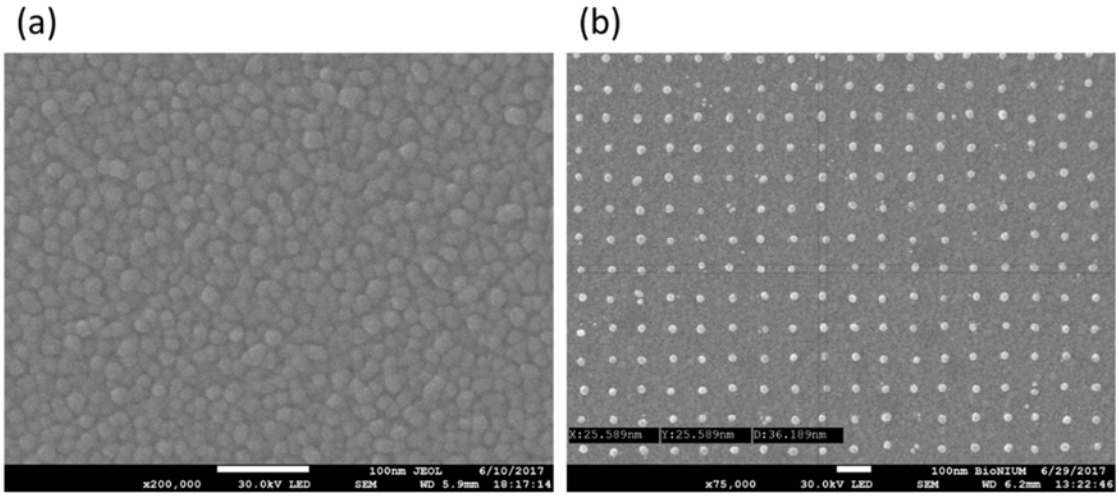

Figure 5.4 SEM image of the ZnO particles less than 5nm (a) and Fabricated Au NPs with 25nm diameter (b).

The plasmon FET has a 100µm by 100µm active layer between two metallic electrodes, the source contact and the drain contact. Particular challenges are to pattern large arrays of well-defined nanodisks with uniform separation between particles. Fabrication methods have been developed using conventional electron beam lithography to produce a million nanoparticles of the same size as shown in Figure 5.5. They were incorporated in the active layer area in the plasmon FET which is challenging and interesting for the study of sensitive biosensors.

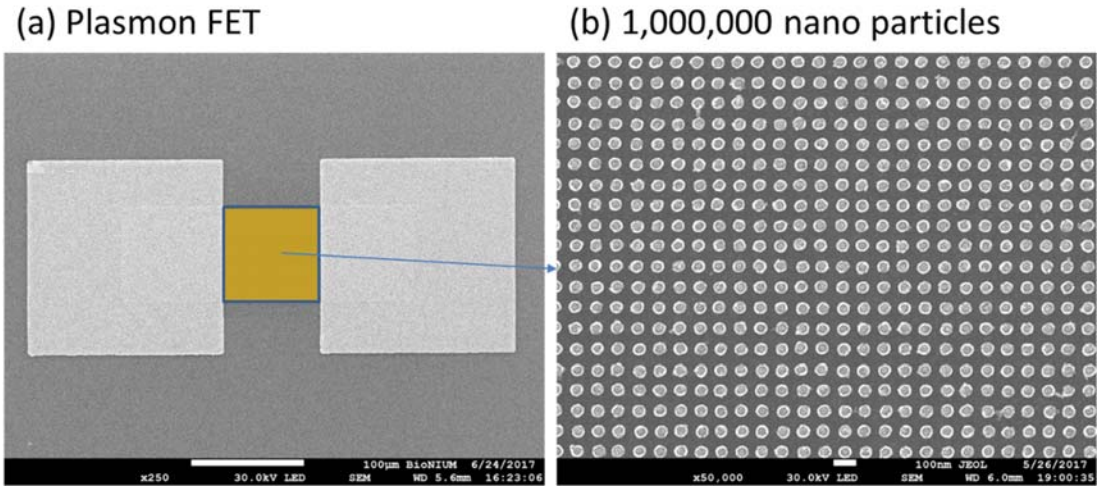

Figure 5.5 SEM images of the Plasmon FET (a) and Incorporated 1,000,000 Au 50nm diameter Particles in the Plasmon FET (b).

The exposure is performed with standard EBL and is based on the principle of direct writing procedures. To prepare the SEM for electron beam lithography (EBL) mode, the following values must be set: an acceleration voltage of 30kV, probe current of 1, filament current of 2.24A, the emission current for nanorod is at most 140μA, and the emission current for nanodisk is at most 108μA. Values for the setting are guideline values which we determined in the BioNIUM cleanroom facility after specific standard tests. When we conducted the EBL process for nanodisk patterns with emission currents between 130μA and 140μA, the lift-off step could not be completed because the beam stability decreases and the electrons expose the walls of the disk pattern as shown in Figure 5.6.

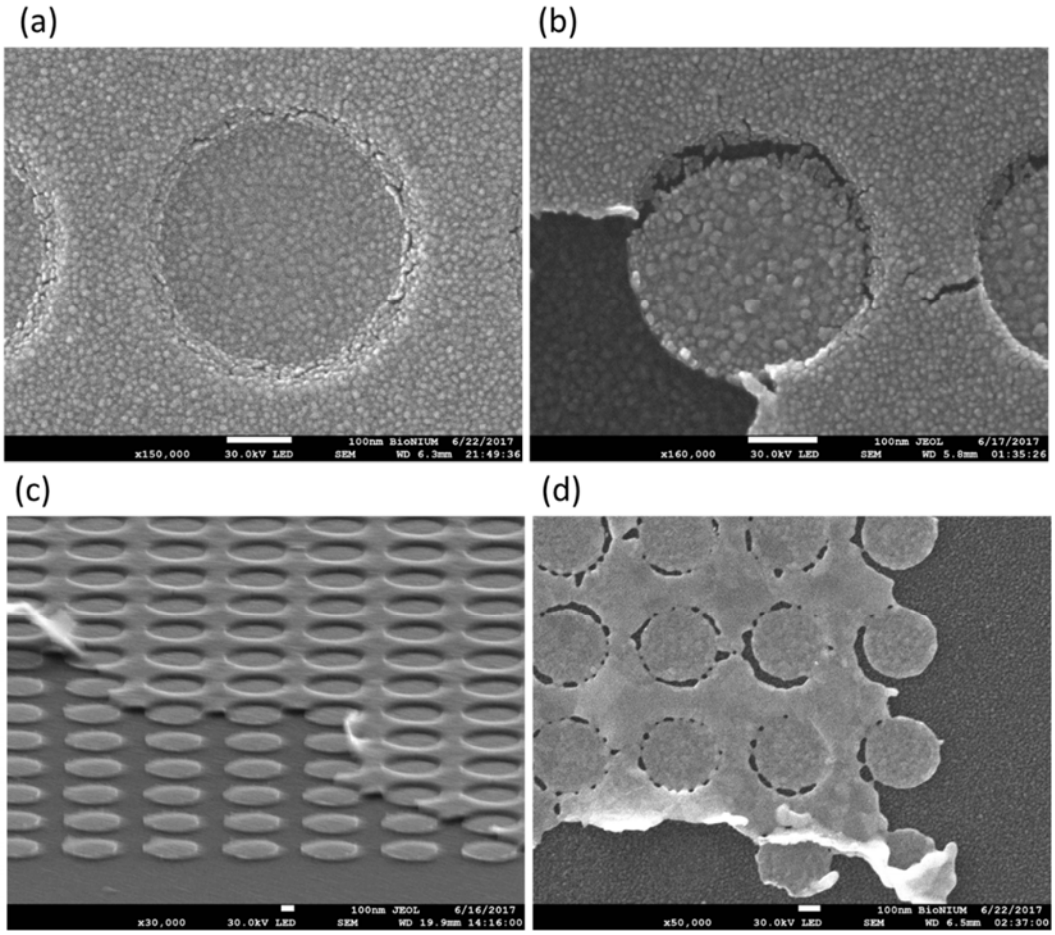

Figure 5.6 SEM images after Au deposition (a), after lift-off process (b and c), and after heat treatment with exposure process using unstable electron beam (d).

Summary

In this chapter, we presented the fabrication process of the plasmon FET using EBL. Nanostructures were fabricated on prepared thin film transistor using standard cleanroom and electron-beam lithography techniques. We carried out Polymethyl Methacrylate (PMMA) resist spin coating, Electron-beam exposure with the designed pattern, Development, Metal deposition, and Lift-off process as shown in Figure 5.9. Finally, gold nanostructures are incorporated by using the thermal reflow process to crystallize.

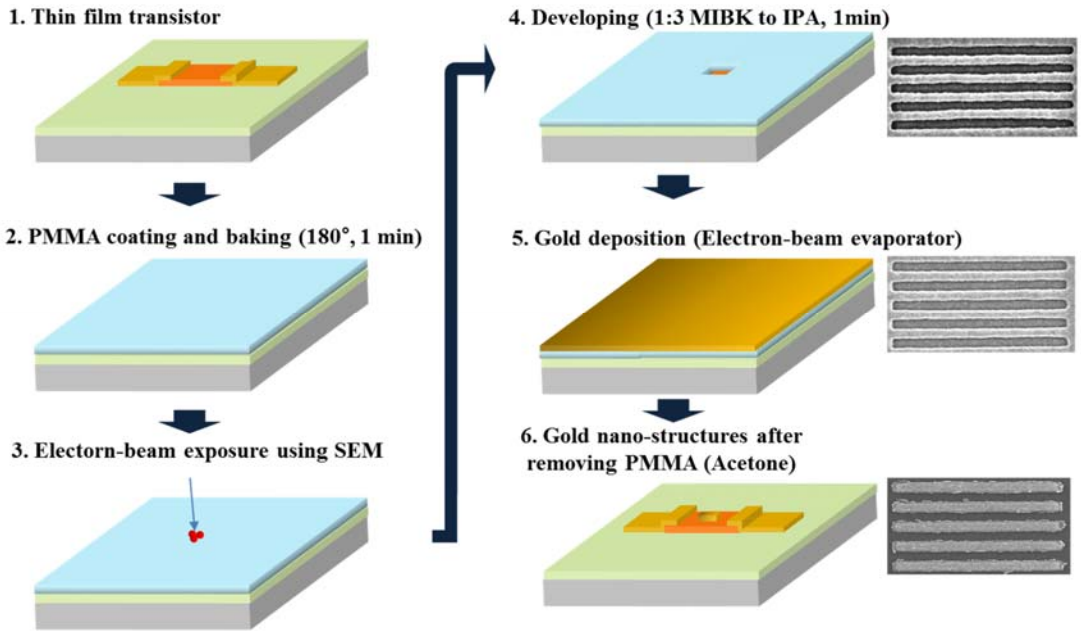

Figure 5.7 The Fabrication Process of plasmon FET using SEM Lithography including spin coating, Electron-beam exposure with the designed pattern, Development, Metal deposition, and Lift-off process.

We succeeded in combining the plasmon FET with different sizes and shapes of metal nanostructures and controlling the size distribution by using NPGS. The deformation can be reduced by increasing the metal thickness and by changing the condition of the reflow method. The spectral response of the plasmon FET with the controlled size and shape will be measured to understand how plasmon resonances are determined with different nanostructures on the active layer.

Chapter 6: STUDY ON WIDE SPECTRAL RESPONSE FOR PLASMON FET

In this chapter, we present experimental measurements of the plasmon FET devices with different nanopatterned metal, size, and different host materials surrounding the nanopatterns. In addition, simulation results based on Finite Difference Time Domain (FDTD) numerical solver are presented and compared to the measured data. Both the empirical and computational study will be further used to optimize the plasmon FET for a tailored spectral response.

Background of Numerical Calculation using FDTD Solution

FDTD solutions is a numerical calculation technique for modeling computational electromagnetics. Equation 6.1 is the fundamental equation of the FDTD solution [113].

$$E_x^{n+1/2}(k) = E_x^{n-1/2}(k) - \frac{\Delta t}{\varepsilon_0 \cdot \Delta x}\left[H_y^n\left(k+\frac{1}{2}\right) - H_y^n\left(k-\frac{1}{2}\right)\right]$$

$$H_y^{n+1}\left(k+\frac{1}{2}\right) = H_y^n\left(k+\frac{1}{2}\right) - \frac{\Delta t}{\mu_0 \Delta x}[E_x^{n+1.2}(k+1) - E_x^{n+1.2}(k)]$$

Equation 6.1 The Fundamental equation of the FDTD solution.

FDTD method can find accurate solutions to the differential equation with a wide frequency range with a single simulation because the method solves in the time domain. When we take the time dependent Maxwell's equations in differential form, the resulting equations for free space are shown in Equation 6.2.

$$\frac{\partial \boldsymbol{E}}{\partial t} = \frac{1}{\varepsilon_0}\nabla \times \boldsymbol{H}$$
$$\frac{\partial \boldsymbol{H}}{\partial t} = -\frac{1}{\mu_0}\nabla \times \boldsymbol{E}$$

Equation 6.2 The Time dependent Maxwell's equations for free space.

We can represent this equation in one dimensional case using E_x and H_y as shown in Equation 6.3.

$$\frac{\partial E_x}{\partial t} = -\frac{1}{\varepsilon_0}\frac{\partial H_y}{\partial z}, \quad \frac{\partial H_y}{\partial t} = -\frac{1}{\mu_0}\frac{\partial E_x}{\partial z}$$

Equation 6.3 The Time dependent Maxwell's equations in one dimensional case.

These equations mean that the electric field and the magnetic field of a plane wave are oriented in the x-direction and in the y-direction, respectively, and the wave travels in the z-direction. After using central difference approximations to the temporal and spatial derivatives, the equation 6.3 results in equation 6.4. All derivatives are discretized for the computer simulation. In equation 6.4, time is discretized by "n", so that, "n+1" stands for one step later in time. The *k* in parentheses means distance step. We can rearrange the equation 6.4 by repeating the calculation process as shown in equation 6.1.

$$\frac{E_x^{n+1/2}(k) - E_x^{n-1/2}(k)}{\Delta t} = -\frac{1}{\varepsilon_0}\frac{H_y^n\left(k+\frac{1}{2}\right) - H_y^n\left(k-\frac{1}{2}\right)}{\Delta x}$$

$$\frac{H_y^{n+1}\left(k+\frac{1}{2}\right) - H_y^n\left(k+\frac{1}{2}\right)}{\Delta t} = -\frac{1}{\mu_0}\frac{E_x^{n+1.2}(k+1) - E_x^{n+1.2}(k)}{\Delta x}$$

Equation 6.4 The Discretization of Maxwell's equations using central difference approximations to the temporal and spatial derivatives.

Using a commercial software, Lumerical FDTD solutions, the optical responses of nanopatterns were simulated in all 3 dimensions. For simplicity, we used the absorption of 9 nanodisks instead of 1,000,000 to 40,000 particles. To match the experimental conditions

precisely, the diameters of the nanodisks were designed to be same as the fabricated structures. The incident light was chosen as a plane wave with the polarization being transverse (TE) or parallel (TM). The polarization has no significant differences for the disk-shape patterns, since we aimed to develop a device without polarization dependency.

The wavelength-dependent absorption of Au nanodisk patterns was simulated. The diameter of nanodisks ranges from 25nm to 400nm and the thickness varied 25nm to 38nm. The following steps are used for the simulation with Lumerical software:

1. The first step is to define a device geometry. For the initial simulation of simple periodic particle systems of a single size and shape, we used the script editor to quickly produce 3 x 3 arrays of gold nanodisks, which are 25 nm tall, on top of a 50nm thick ZnO film which rests on a bulk SiO_2 substrate as shown in Figure 6.1.

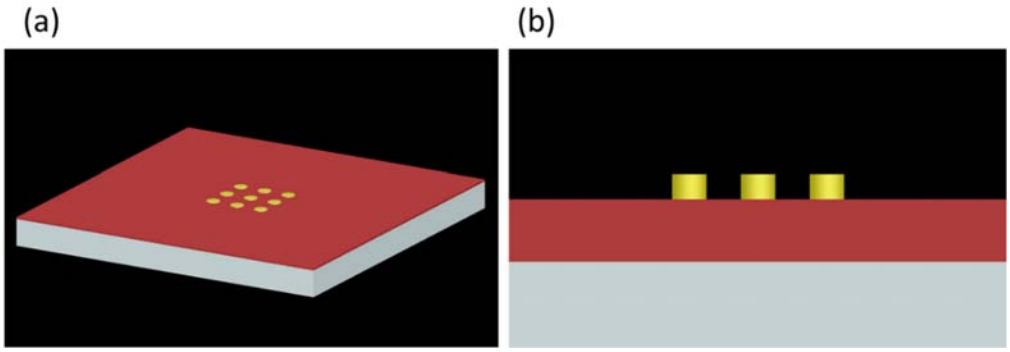

Figure 6.1 The perspective images of the initial device geometry (a) as well as the side view (b).

2. After the device geometry has been created we add our FDTD simulation region. Here we can determine the dimensionality, length, accuracy, and boundary conditions of our simulation. Here we used a 3D simulation of a duration of 500 fs, with a specialized mesh setup for simulations using metallic components. We

use a symmetrical simulation region that is twice the size of a single particle. The size of the simulation region in the Z direction was chosen to be 200nm which completely encloses the particles and ZnO. We will initially keep all our boundary conditions as Perfectly Matched Layer (PML), where absorbing boundary conditions are impedance matched to the simulation region and its materials as shown in Figure 6.2.

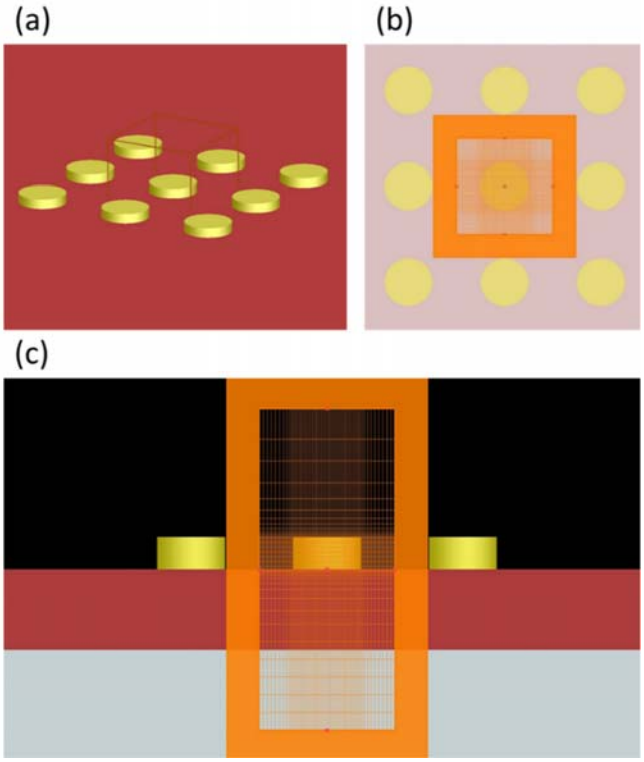

Figure 6.2 Device geometry with simulation mesh region from perspective (a), top (b), and side views (c), respectively.

3. We then place a mesh override region over the area of most concern. In this simulation, we place it around a single metallic nanodisk. We then override the mesh depending on the diameter of the nanodisk, for simulations of a 50nm diameter disk xy mesh sizes of 5Å are necessary for accurate results, while for

over 200nm in diameter override regions of 5 nm or greater suffice. However, keep the z mesh to at least 1 nm override as shown in Figure 6.3.

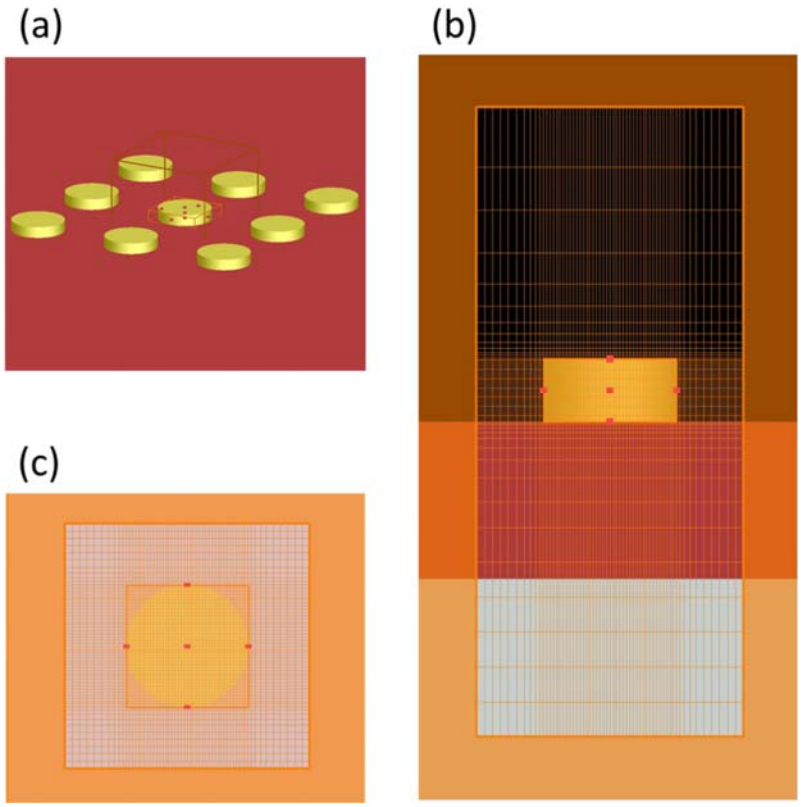

Figure 6.3 Addition of a mesh overide region around the nanodisk for finer results as seen from from perspective (a), side (b), and top views (c), respectively.

4. Afterwards we will place a light source on our sample. We selected a planar source with an amplitude of 1 with no polarization or incident angle. Depending on boundary conditions you may want to select a periodic/bloch or diffracting plane wave. We can then select the frequency range of our simulation. In our case, we chose from 300 nm- 2000 nm. We place this source completely around our simulation region in the xy plane but within the simulation in the z-plane as shown in Figure 6.4.

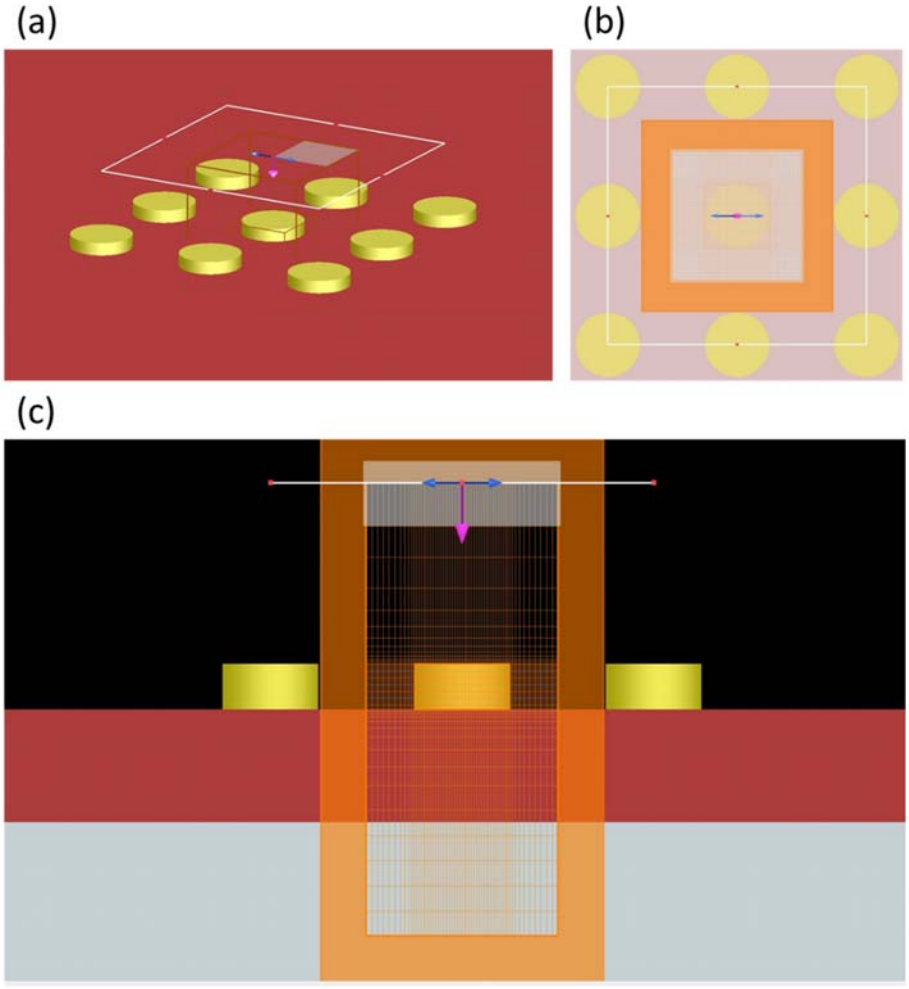

Figure 6.4 Implementing a plane wave source above the device as seen from perspective (a), side (b), and top views (c), respectively.

5. Once we have our polarization we can use symmetry to reduce memory and time requirements of our simulation. This is done by changing the boundary conditions in the FDTD simulation region from PML to Anti Symmetrical or symmetrical, which are chosen by the direction the Electric field of the source, the blue arrow, points. It is necessary that both the source and geometries are symmetrical to use these boundary conditions as shown in Figure 6.5.

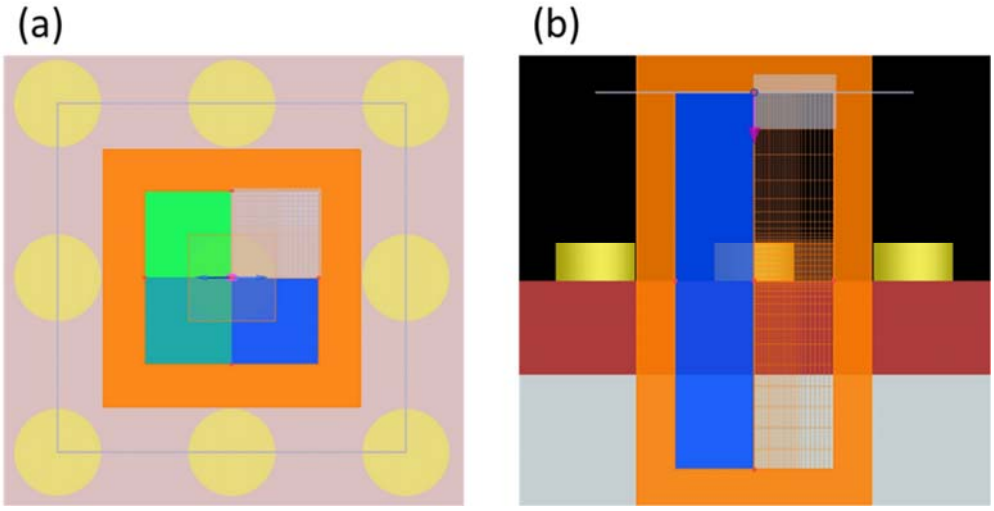

Figure 6.5 Taking advantage of device and source symmetry to reduce simulation resources as veiwed from the top (a) and side (b).

6. With this completed we add monitors to record important information. We use the power absorbed analysis group which contains 2 monitors Field, the electric field distribution inside the simulation region, and index that measures the complex refractive index during the simulation. From there a pre-written script will determine the power absorbed at each wavelength from our source using this equation:

$$L = -0.5\omega |E|^2 imag(\varepsilon)$$

Equation 6.4 The fundamental equation for the power absorbed at each wavelength.

This analysis group will be placed completely around our disk array.

7. We can use the script editor to create absorption cross sections and field distribution.

8. Running size sweeps we can conduct many simulations at a single time changing the parameters of the simulation, making sure to keep proper proportions as shown in Figure 6.6.

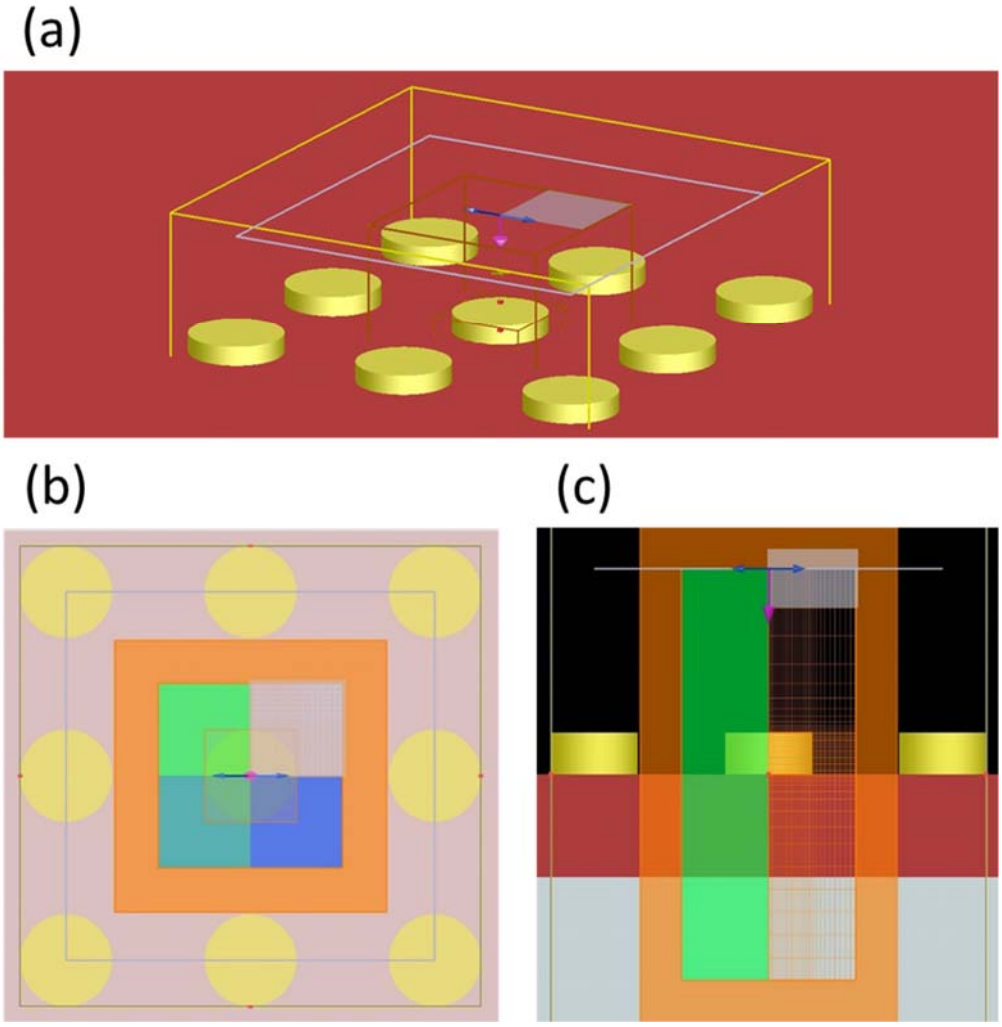

Figure 6.6 Incorporating a power analysis group which uses monitors to determine the power absorbed in the ZnO as seen from perspective (a), side (b), and top views (c), respectively.

ZnO Thin Film Transistor Characteristics

To get ideal ZnO FET characteristics, the ZnO layer was prepared using a pulsed laser deposition system at the Wright-Patterson Air Force Research Laboratory. As noted in Chapter 2, the plasmon FET has a unique working mechanism to collect plasmon induced hot electrons and produce an amplified signal. The internal field from gate voltage bias enables an efficient collection of hot electrons and increases channel conductivity by its drift force. In addition, a Schottky junction between the plasmonic nanostructure and the semiconductor offers a distinct method of plasmon generated hot electron collection. The mechanism of the plasmonic hot electron collection using a gold NP-ZnO Schottky junction differs from a conventional Ohmic device. Since the plasmon resonance creates a localized field at the surface of the nanostructure, the plasmonic resonance favorably excites the free electron at the Fermi level (sp-band absorption)) [114]. Therefore, the excited energy of these hot electrons is higher than the Schottky barrier (Φ_b), and consequently, these hot electrons can be transported through to the semiconductor.

We used the ZnO thin film for the FET active layer to avoid overlap of spectral response by nanostructures in the plasmon FET. The spectral response of ZnO in the range of 350-1500nm is shown in Figure 6.7. So, the bandgap of ZnO thin film is around 3.44eV (1.24/360nm=1.24/0.360μm=3.44eV). The bandgap of ZnO indicates that the thin film does not have any optical response at the spectral range between 400nm and 1500nm. The Schottky barrier between gold and ZnO is 0.6 ~ 0.7 eV which correspondes to light energy in the range of 1771 ~ 2066 nm wavelength. This is a very important working mechanism, because the Schottky barrier can selectively allow the hot electrons from only the plasmonic absorption in the nanostructure from 450nm wavelength or greater. Therefore,

an engineered metal nanostructure-semiconductor Schottky junction will enable to detect the targeted photon energy in the near-IR spectrum.

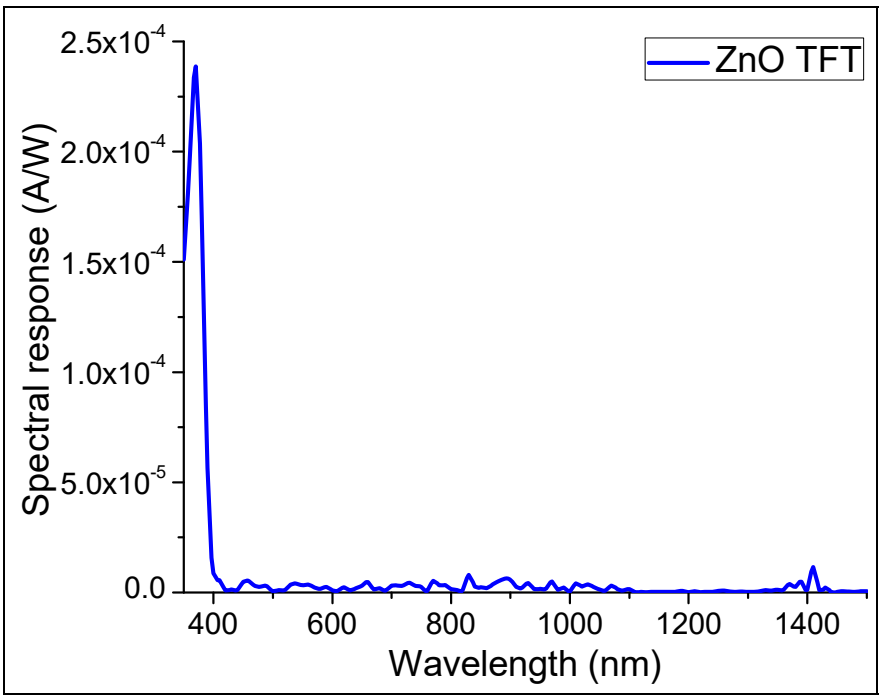

Figure 6.7 The spectral response of ZnO in the wavelength range from 350nm to 1500nm.

Figure 6.8 shows the I-V characteristics of a fabricated thin film transistor with a ZnO channel. The measured drain current shows the typical n-type thin film transistor characteristics, signifying that the electrical properties of the fabricated FETs are nearly ideal. The thin film transistor (TFT) has a threshold voltage of ~4V and a saturation voltage of ~16V at a gate voltage bias 20V. Once the drain voltage is large enough compared with the gate bias to deplete the carrier accumulation layer beneath the ZnO film, the device drain current saturates which is described as a pinch-off mechanism at the drain contact. All electrons that reached the drain space charge region are attracted into the drain contact by the drain bias. It does not pinch off the drain current, and causes it to saturate.

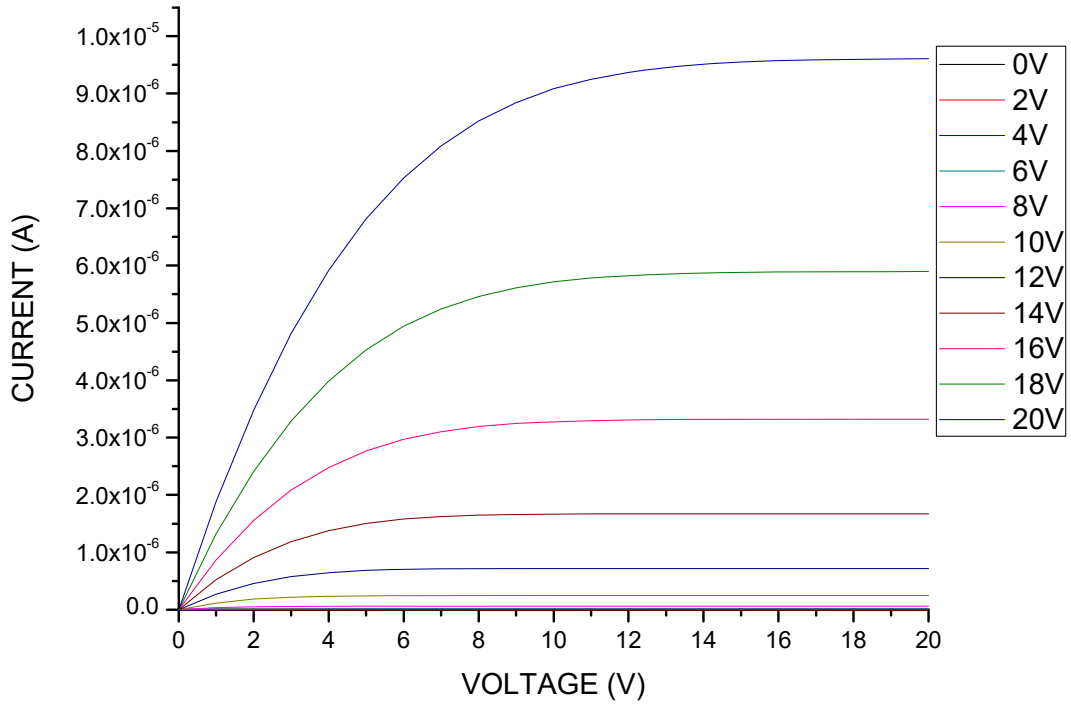

Figure 6.8 I-V characteristics of fabricated FETs with the ZnO channel.

Study on Metal Nano Pattern Shape of Plasmon FET

Gold nanostructures can be added on top of the ZnO layer with various fabrication processes. Figure 6.9 (a) shows the SEM image of the nanorod array on the ZnO active layer of the plasmon FET using electron beam lithography. Right after the lift-off process, the device was characterized to find its spectral response. The device showed no photocurrent responsivity. We further investigated the nanostructures on ZnO film. The nanostructures were 15nm thick. The SEM cannot offer high resolution while focusing on two different objects separated by more than 15nm in Z-axis. Thus, 10nm-thick gold nanostructures were fabricated on the ZnO active layer to observe the surface with the nanostructures array. Figure 6.9. (b) shows that the nanostructures did not densely

aggregated on the ZnO surface. This poor aggregation may cause weak adhesion of gold nanostructures to the ZnO film, consequently, hindering the electron transfer from metal to ZnO.

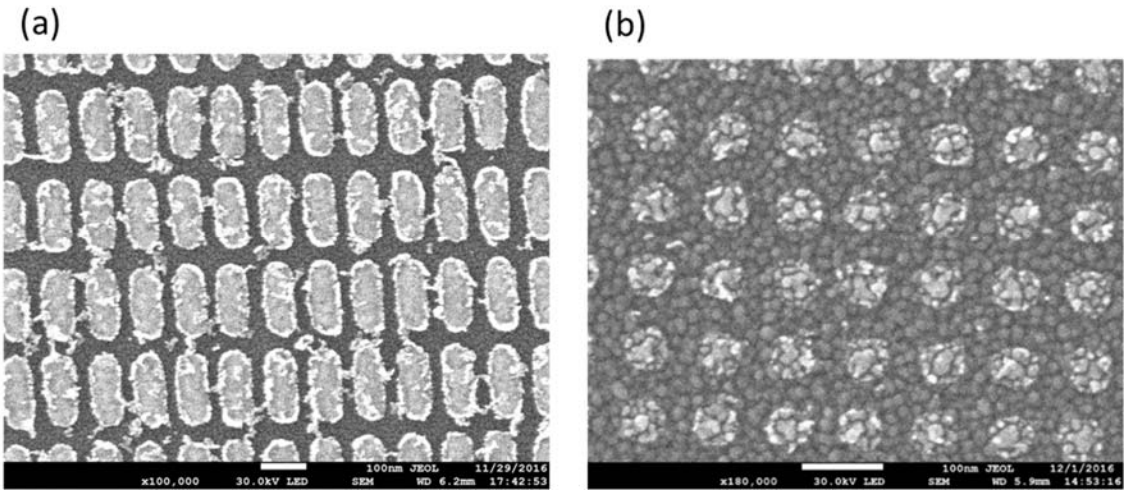

Figure 6.9 SEM images of Au 15nm nanostructures (a) and Au 10nm nanostructures in thickness on ZnO layer using the electron-beam lithography.

Thus, we modified the gold nanostructure by using the thermal reflow method. We used this method for randomly distributed gold nanoparticles and we used the same process condition (at 300˚C for 10 minutes) for the reconditioning of the gold nanostructures. Figure 6.10 shows the SEM images of gold nanostructures incorporated in the plasmon FET with the sizes of 50nm by 150nm (a) and 50nm by 200nm (c) after heat treatment at 300˚C for 10 minutes (b, d). After annealing, the nanostructure has a minor deformation of its original shape but it looks denser, which ensures better crystallization and adherence to the ZnO.

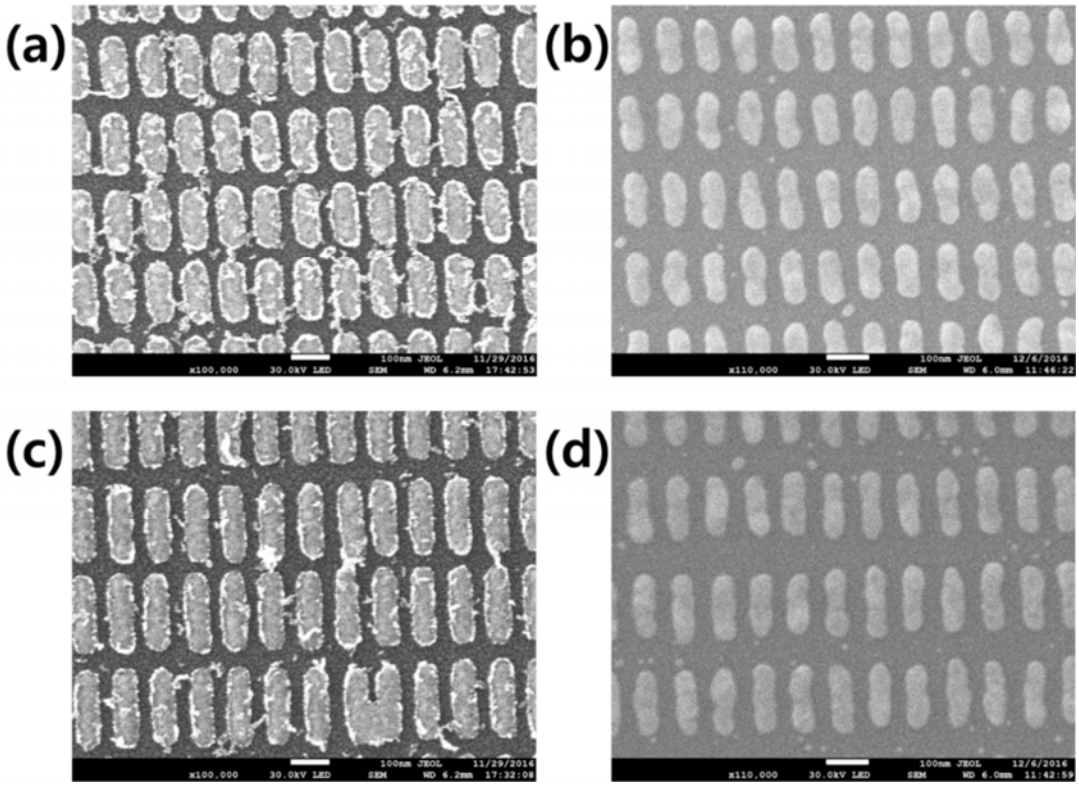

Figure 6.10 SEM images of 15nm thick gold nanostructures on ZnO surface with the sizes of 50nm by 150nm (a) and 50nm by 200nm (c) after heat treatment at 300˚C for 10 minutes (b, d).

We provide further evidence of the nanostructure crystallization by measuring the spectral response of the annealed device compared with the spectral response before annealing. Figure 6.11 shows the spectral response of the annealed device. The result shows broad spectral response but no sharp peak due to the deformation and the broad size distribution of the nanostructures after annealing.

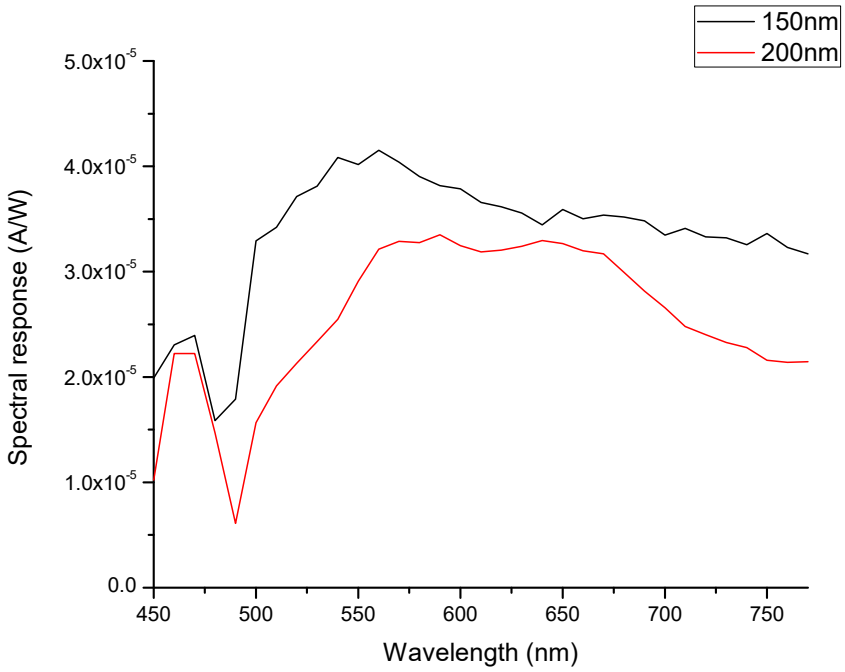

Figure 6.11 Spectral response of the plasmon FET after annealing.

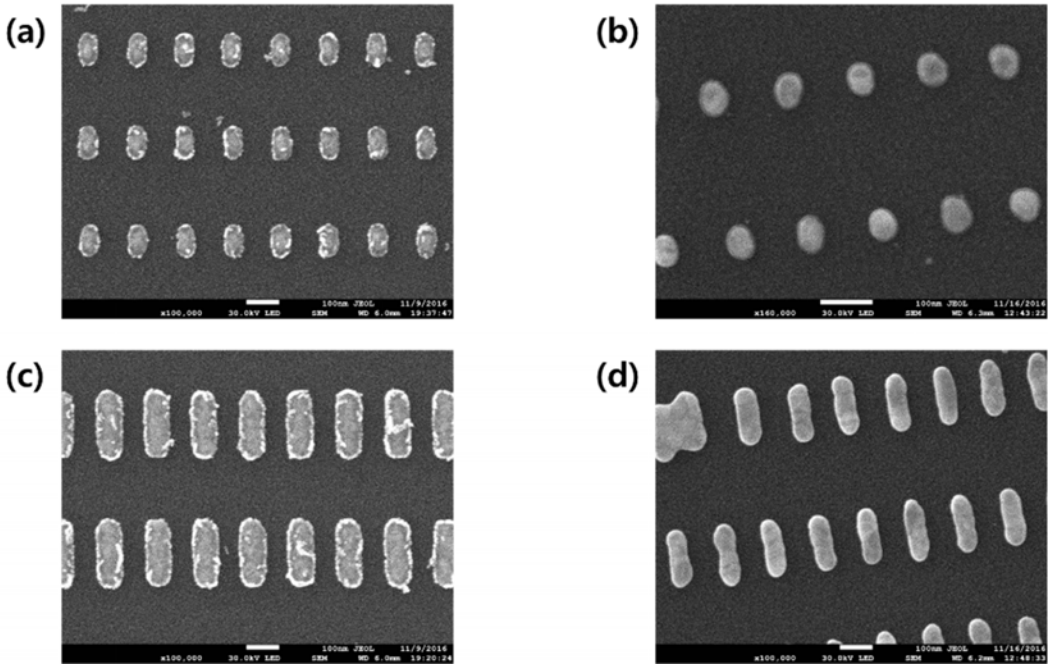

Figure 6.12 SEM pictures of Au 25nm-thick nanostructures on ZnO surface 50nm by 100nm and 50nm by 200nm after heat treatment at 300˚C for ten minutes.

Different gold thicknesses were examined to control the size distribution and reduce the deformation of the nanostructures. When the nanostructures are thicker we found less deformation of the nanostructions. Therefore, we increased the gold thickness from 15nm to 25nm to keep the shape of patterns after annealing. Thus, the patterns still have some distortions after heat treatment at 300˚C for 10 minutes as shown in Figure 6.12. And this structural deformation limits the control of the spectral response.

To have better control of the nanostructures, nanowire (slit) patterns were fabricated. The 300˚C heated wire patterns show uniform size as shown in Figure 6.13. However, a uniform long metallic nanowire has limited coupling to plane light source. The nanowire pattern has the polarization dependence because of its structural asymmetry. Practically, a polarization dependence will limit the spectral response from the unpolarized light source. Therefore, a different approach is required to maximize the efficiency of the device. Finally, we selected disk shaped patterns due to its reduced distortion and no polarization dependency. More details will be discussed in coming sections.

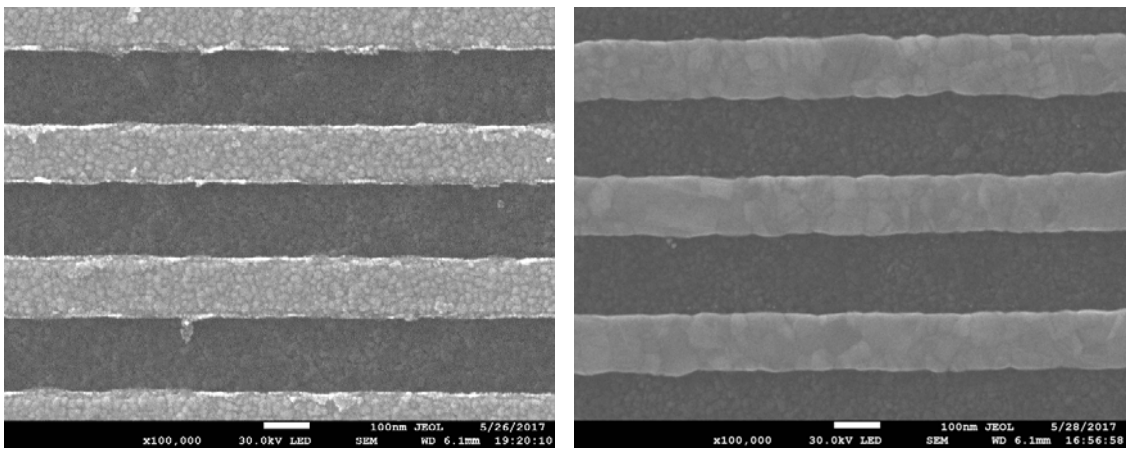

Figure 6.13 SEM images of 100nm width nanowire patterns in plasmon FET before (left) and after the heat treatment (right).

Spectral Response with Different Metal Composition of Nano Patterns

In plasmonics, noble metals are commonly used to serve as antennas that can convert light to electrical signals when their scale become nanometer size. Different metal has different plasma frequency that determines the surface plasmon resonance frequency. Therefore, we need to select proper metals for the plasmonic absorption at the targeted wavelengths. Noble metals such as gold and silver have been widely used in electronics and structural materials. In previous work, we used both silver and gold particles to investigate wideband spectral response. The plasmon FET was incorporated with silver nanoparticles which were fabricated using the thermal reflow method as shown in Figure 6.14 and measured as shown in Figure 6.15. The fabricated silver nanoparticles have sizes between 10-100nm in diameter. The silver nanoparticles show the localized surface resonance around 500nm, which is much shorter wavelength than the case of gold nanoparticles. Therefore, the silver nanoparticles can cover the spectral response between 400nm to 500nm, that the gold nanoparticles cannot cover.

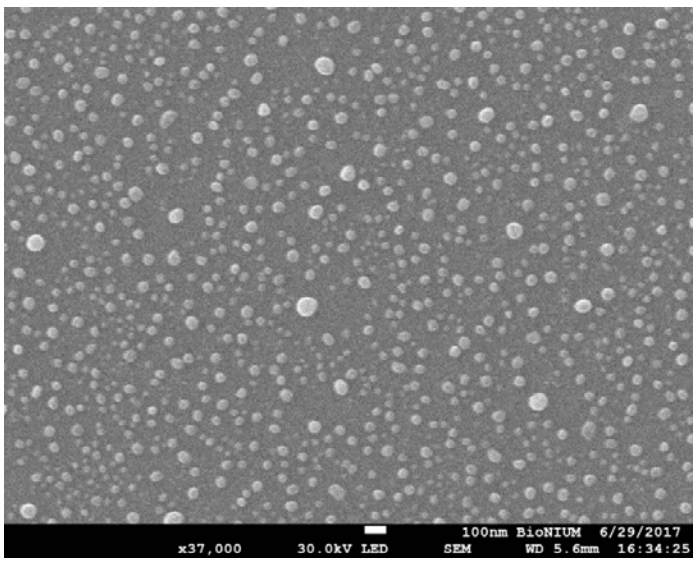

Figure 6.14 SEM image of silver nanoparticles in the plasmon FET.

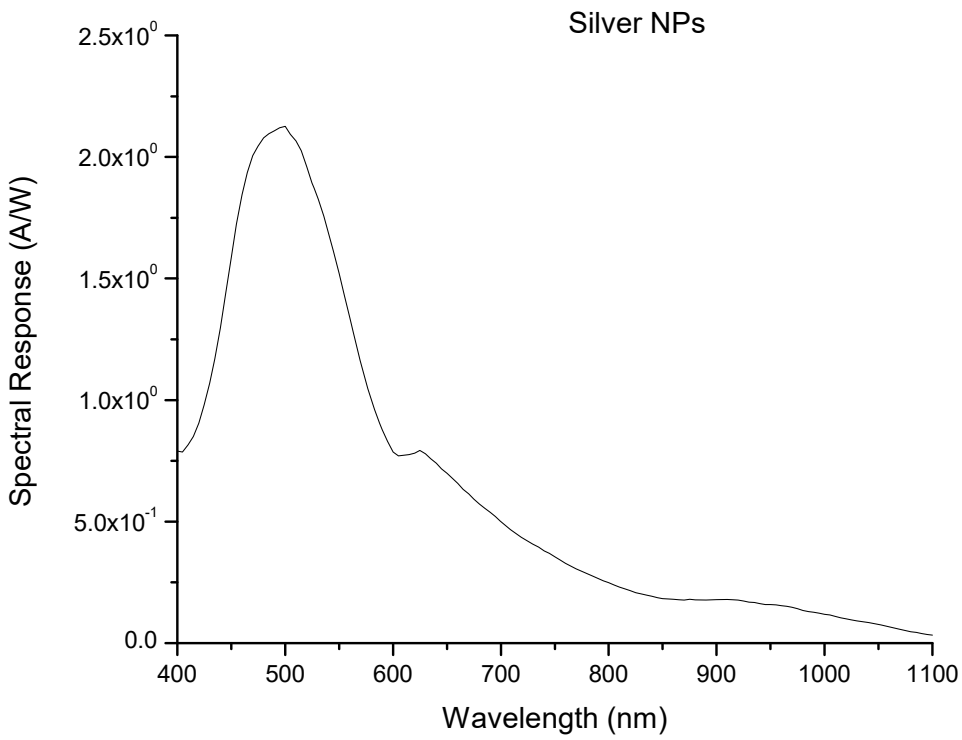

Figure 6.15 The spectral response of plasmon FET with silver nanoparticles.

To investigate how much both silver and gold nanostructures expand their spectral response toward the IR regime, we fabricated plasmon FETs with diameter sizes of 100nm, 200nm, and 300nm disk patterns using silver and gold, and measured the spectral responses of the plasmon FETs. With the diameter sizes, silver and gold support surface plasmon in 400nm to 800nm and 450nm to 1600nm regions respectively as shown in Figure 6.16 ~ 18.

The silver based nanostructures are very good in the visible spectrum, but it was difficult to extend its spectral response beyond 1000nm. Thus, we concluded that Silver and gold nanostructures can be separately used for visible range and near IR, respectively.

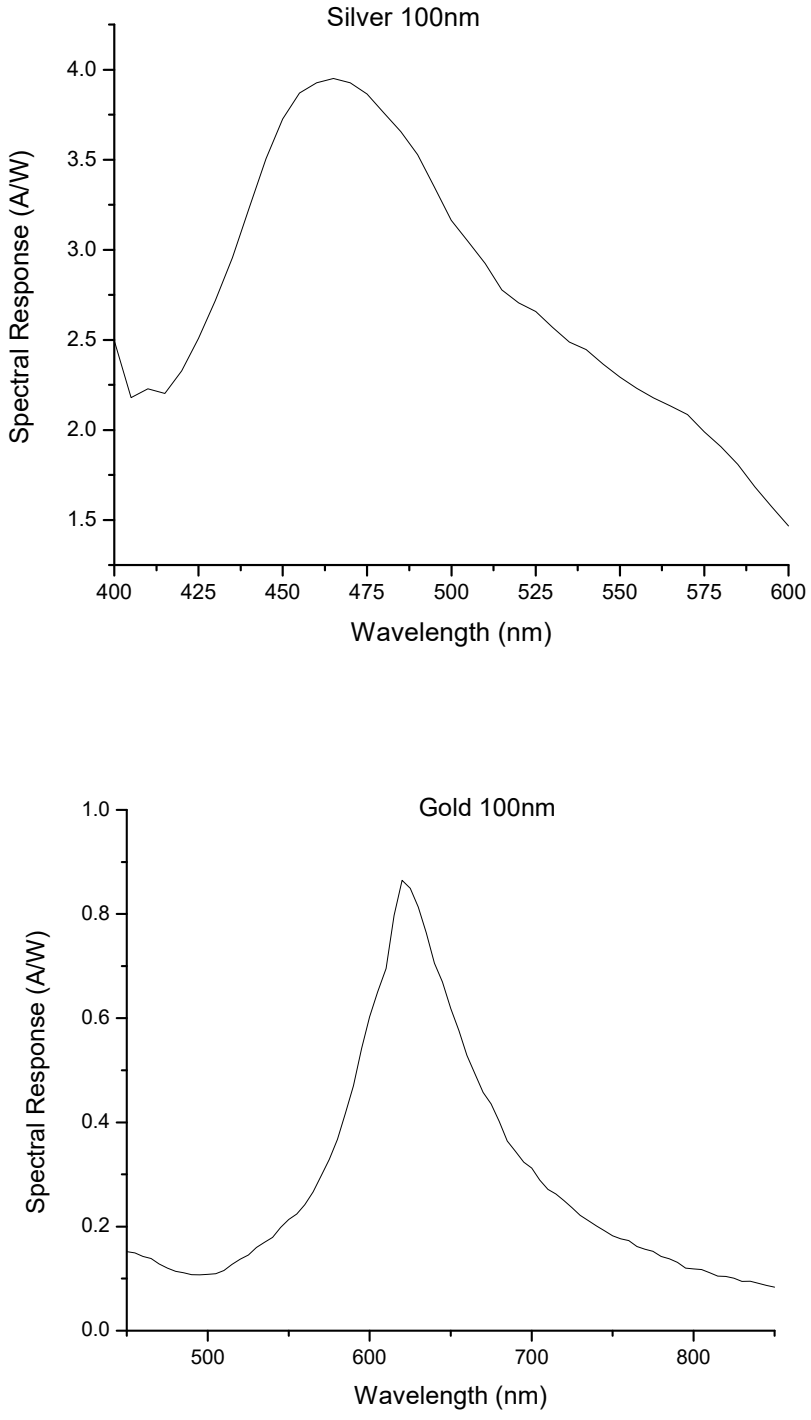

Figure 6.16 The spectral responses of 25nm thick 100nm diameter Ag nanodisk patterns (top) and Au nanodisk patterns (bottom).

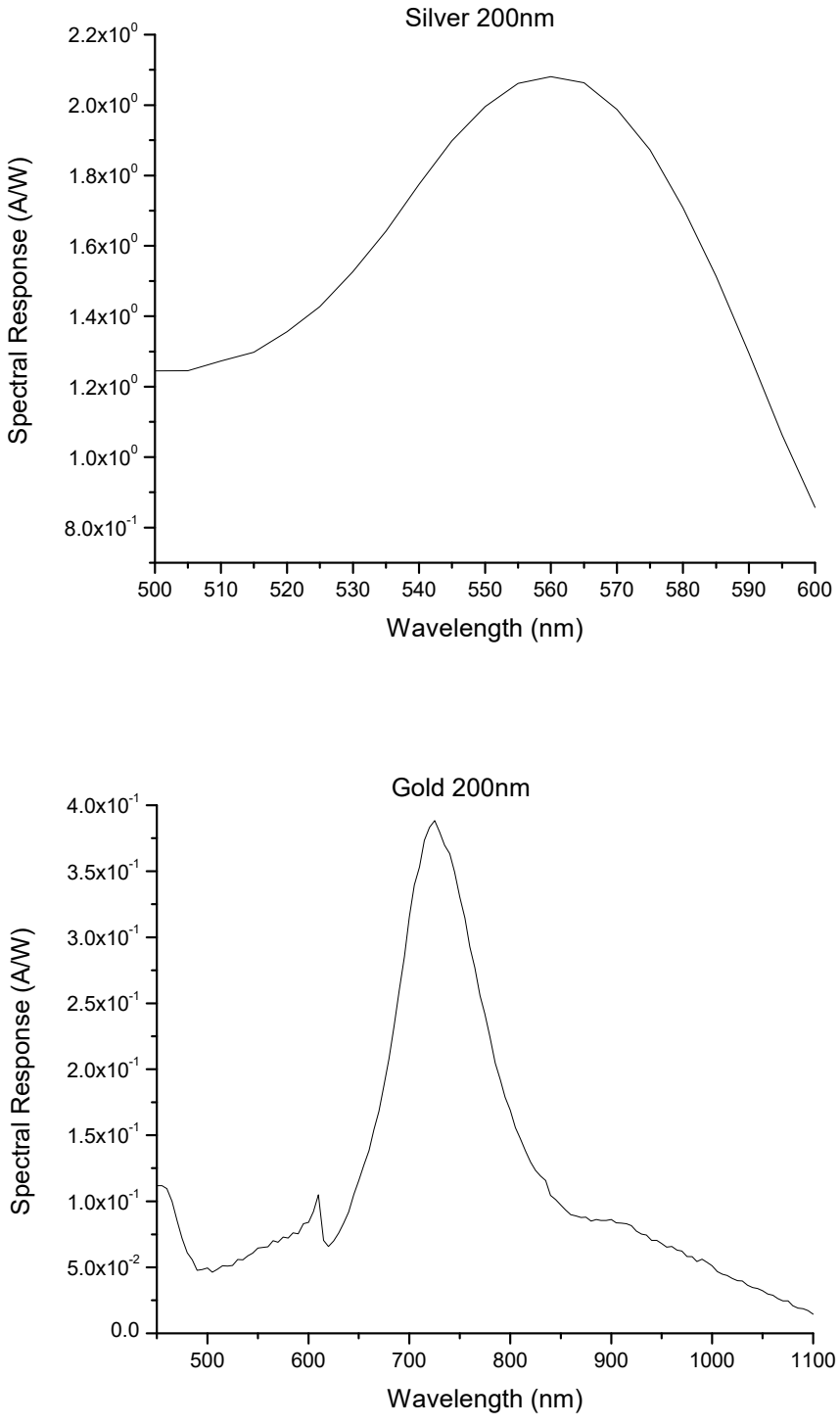

Figure 6.17 The spectral responses of 25nm thick 200nm diameter Ag nanodisk patterns (top) and Au nanodisk patterns (bottom).

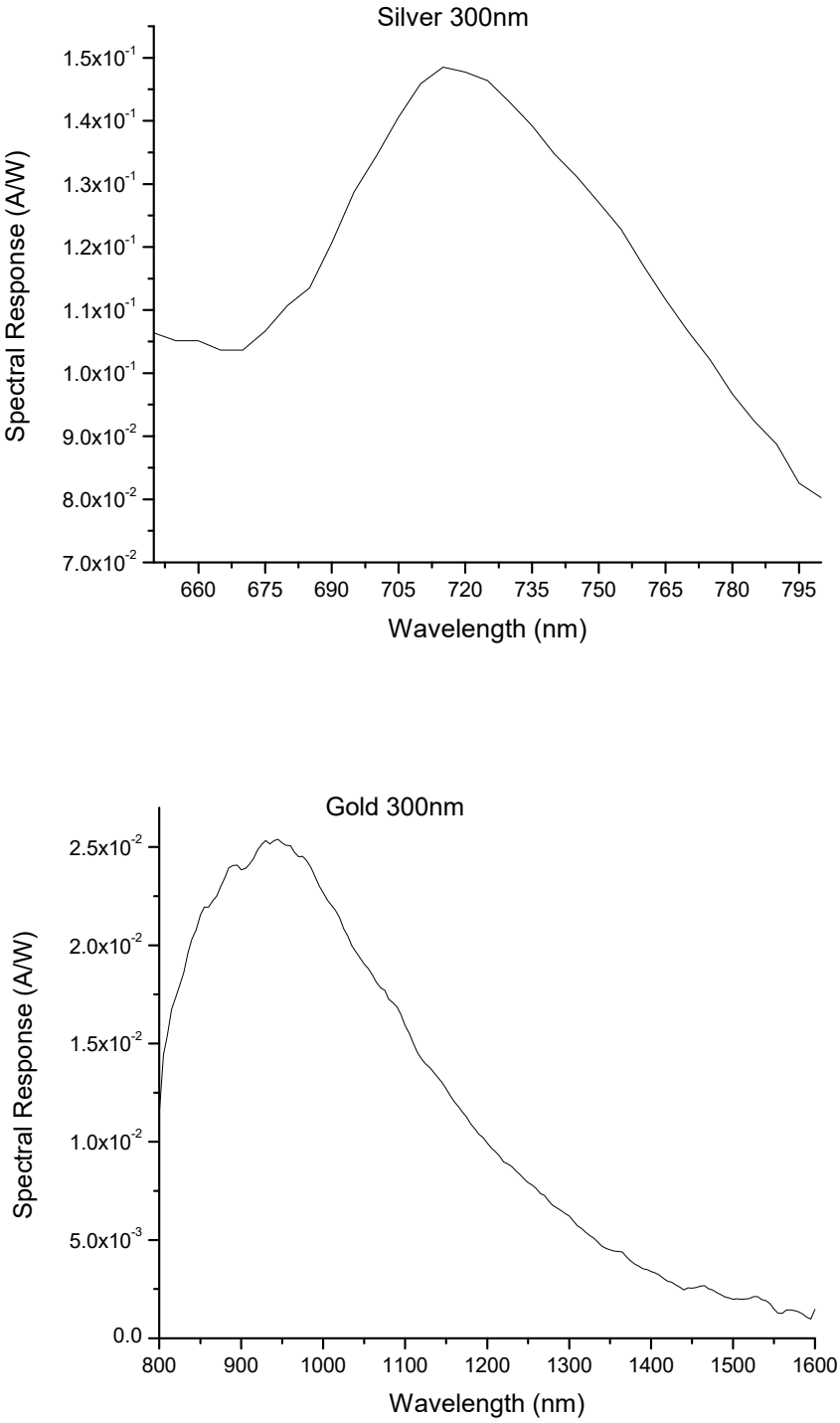

Figure 6.18 The spectral responses of 25nm thick 300nm diameter Ag nanodisk patterns (top) and Au nanodisk patterns (bottom).

The plasmon FET with silver nanoparticles using the thermal reflow method has a strong spectral response from 400nm to 600nm wavelength region in Figure 6.15. The 200nm diameter gold nanodisk patterns, with a 20nm thickness, on the ZnO thin film transistor was fabricated and the thermal reflow method was processed with the deposited 5nm silver and the deposited 5nm gold as shown in Figure 6.19 and Figure 6.20 respectively.

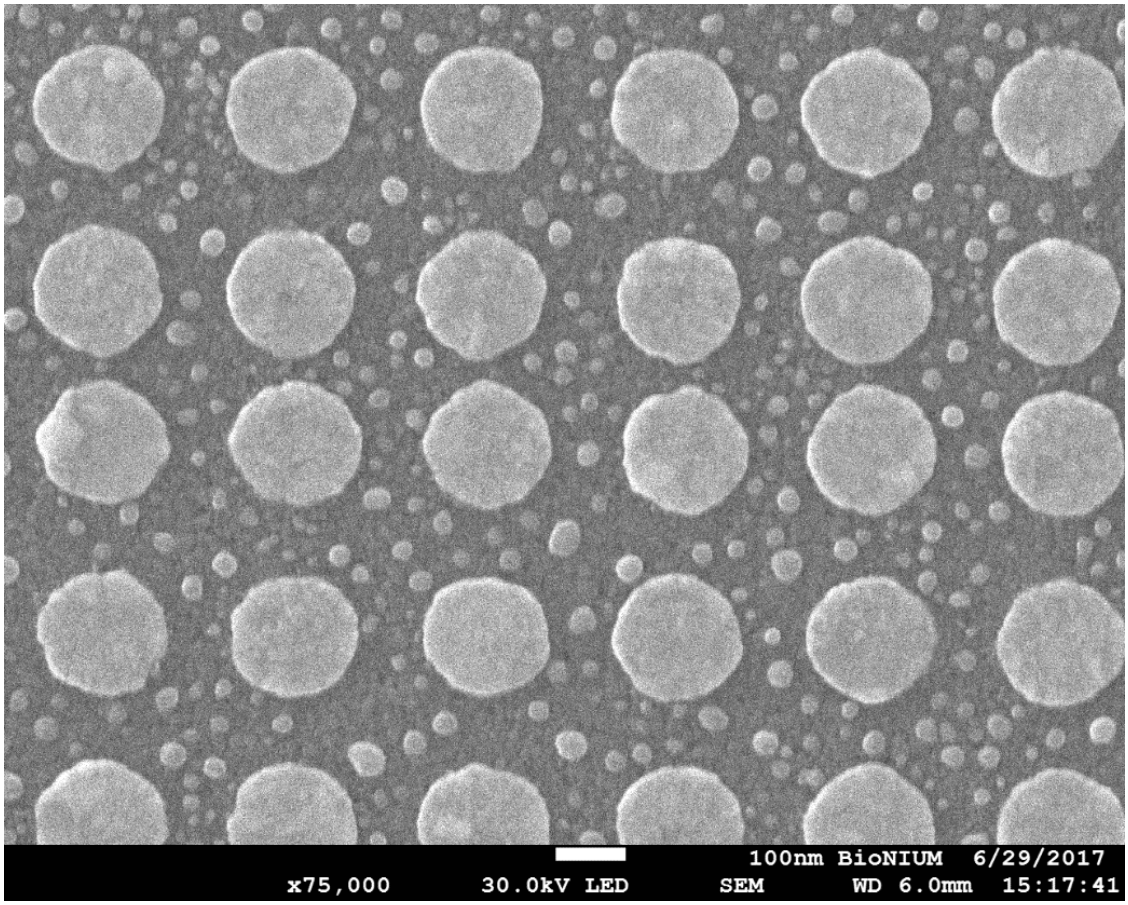

Figure 6.19 The SEM image of the 20nm thick 200nm diameter Au disk patterns with Ag nanoparticles.

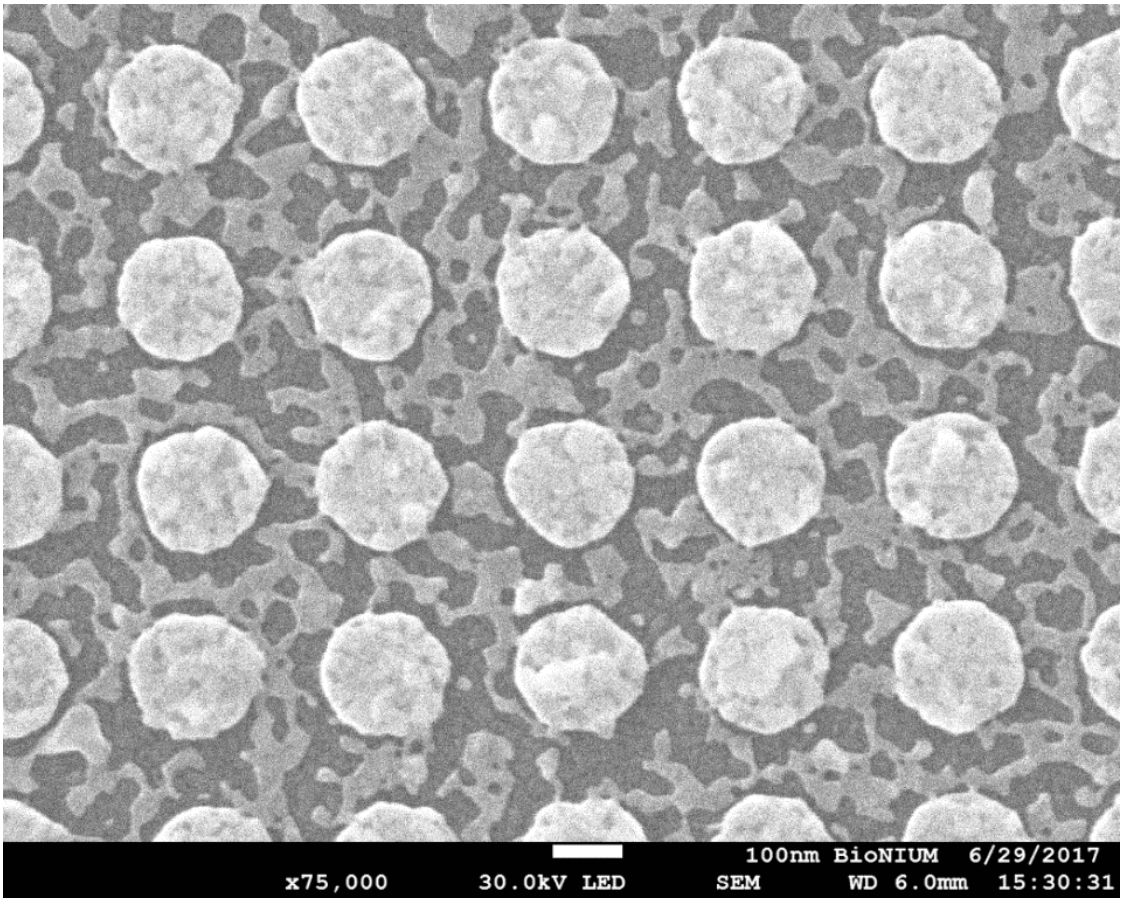

Figure 6.20 The SEM image of the 20nm thick 200nm diameter Au disk patterns with the deposited 5nm Au after the thermal reflow process.

We increased the pattern thickness from 20nm to 25nm. The 200nm Au nanodisk patterns, with a 25nm thickness, on the ZnO thin film transistor were fabricated, an additional 5nm of silver was deposited and then annealed. This deposition and temperature annealing process is known as the thermal reflow method as shown in Figure 6.21. However, with the 25nm thick Au patterns, the deposited 5nm silver, after the thermal reflow method, did not become silver nanoparticles as expected, but only increased the volume of the Au nanodisk patterns as shown in Figure 6.21 (right).

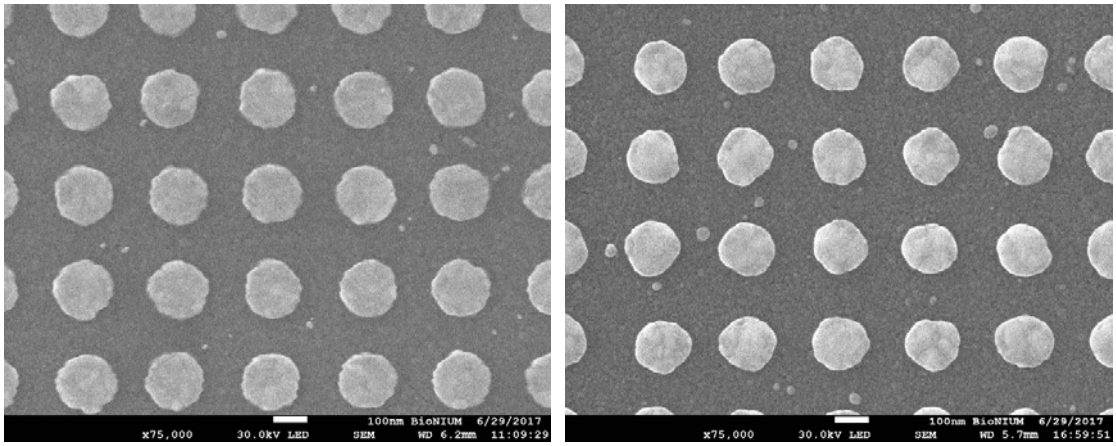

Figure 6.21 SEM images of the 25nm thick 200nm diameter Au disk patterns (left) and after the thermal reflow process with the deposited 5nm Ag (right).

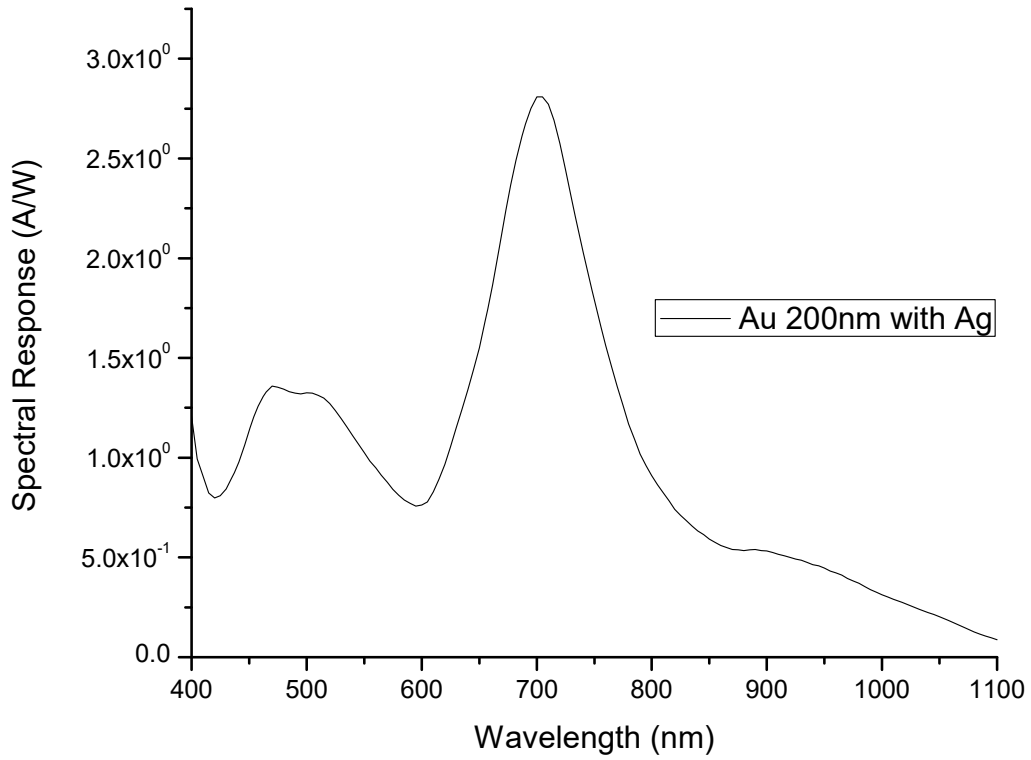

Figure 6.22 The spectral response of the plasmon FET with 25nm thick 200nm diameter Au disk patterns after the thermal reflow process with the deposited 5nm thick Ag.

The spectral response of the plasmon FET has two resonance peaks as shown in Figure 6.22. The second peak wavelength is the same as the spectral response peak of the plasmon FET before the deposition of 5nm of Ag. Further investigation was made to find the reason for the first peak wavelength. The SEM image of Figure 6.23 shows that within the nanodisk patterned area, only a few Ag nanoparticles were formed, but we found decent number of silver nanoparticles at the outside of the nanodisk area. Figure 6.24 shows the SEM image after the thermal reflow process with the 5nm thick Ag. It also shows the size difference depending on the substrates (the incorporated Ag nanoparticles on SiO_2 are smaller than the Ag nanoparticles on ZnO). Therefore, we concluded that the Ag nanoparticles on ZnO outside of the nanodisk pattern area causes the first peak of the device spectral response and this is limited due to the size of the area that the silver nanoparticles are located.

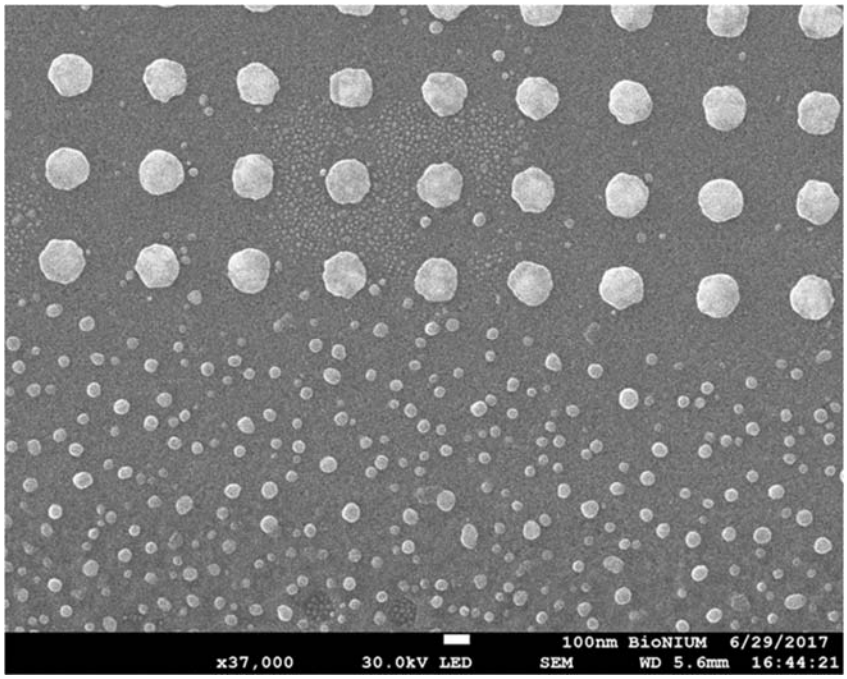

Figure 6.23 The SEM image of the nanoparticles within the nanodisk patterned area (top) and outside of the nanodisk area (bottom).

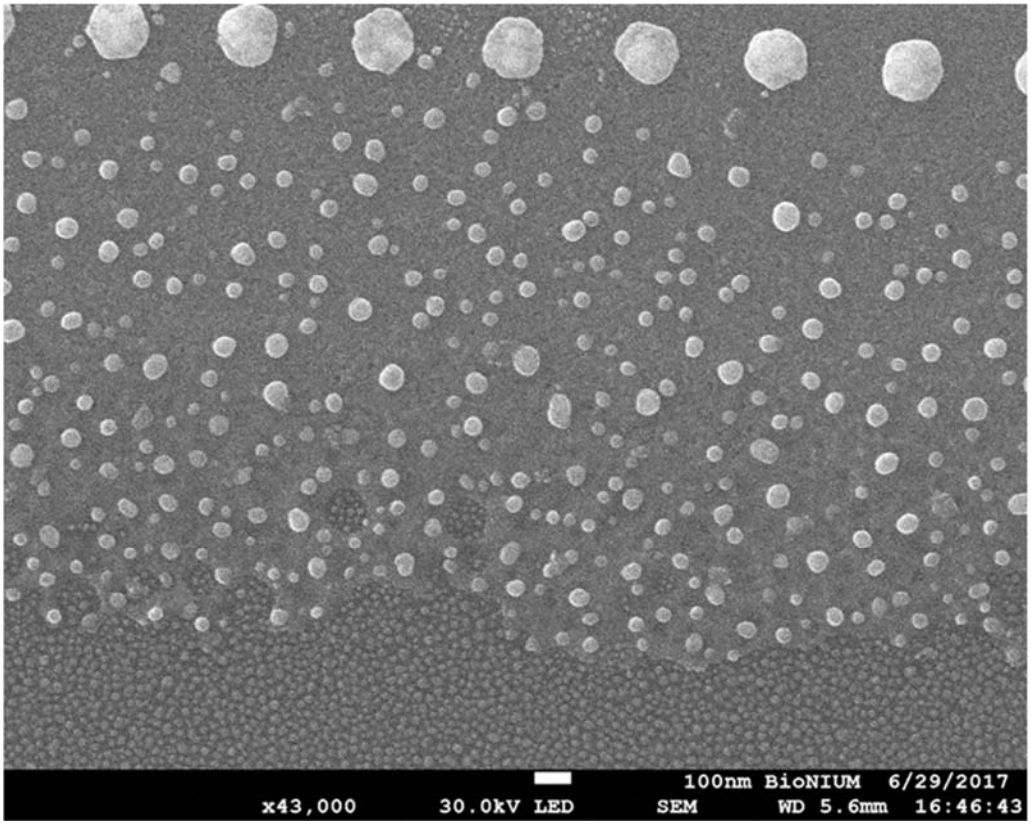

Figure 6.24 The SEM image of the nanoparticles on ZnO layer (middle) and on SiO_2 substrate (bottom).

To investigate the limitation of NIR spectral response, 100nm, 300nm and 400nm diameter nanopatterns were incorporated on the ZnO TFT (a 25nm thick Au nanodisk pattern and the Ag silver nanoparticles are used). With the deposited 5nm thick Ag, the 25nm thick Au nanodisks bulked up after the thermal reflow method instead of Ag nanoparticle formation as shown in Figure 6.25. Regardless of the nanodisk's diameter, the 25nm thick Au nanopatterns do not have the Ag nanoparticles inside the Au pattern area when we increased the spacing between patterns such as the 200nm spacing as shown in Figure 6.27 and 6.29. We need further investigation on this fabrication issue in the future. Alternatively, the nanodisks can grow in volume. The spectral responses of the plasmon

FET with 25nm thick 300nm and 400nm diameter Au disk patterns after the thermal reflow process with the deposited 5nm Ag were measured as shown in Figure 6.28 and 6.30.

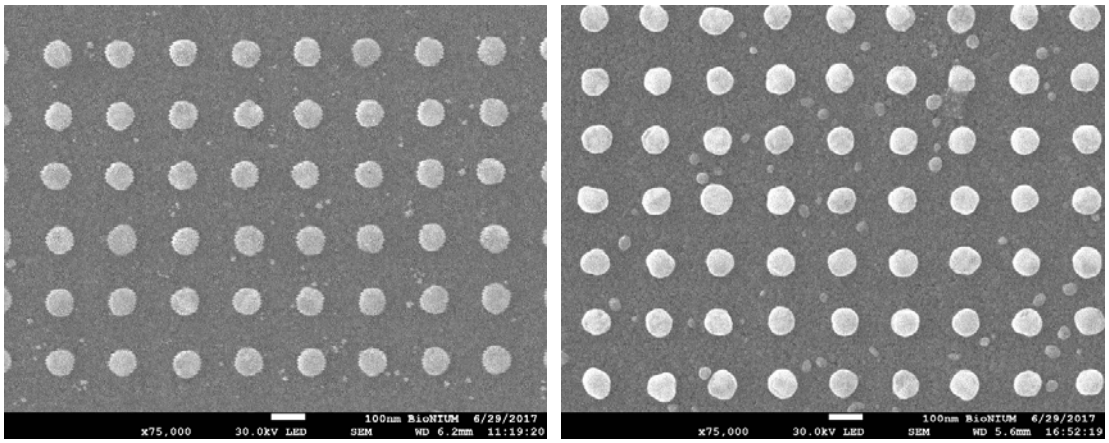

Figure 6.25 SEM images of the 25nm thick 100nm diameter Au disk patterns (left) and after the thermal reflow process with the deposited 5nm Ag (right).

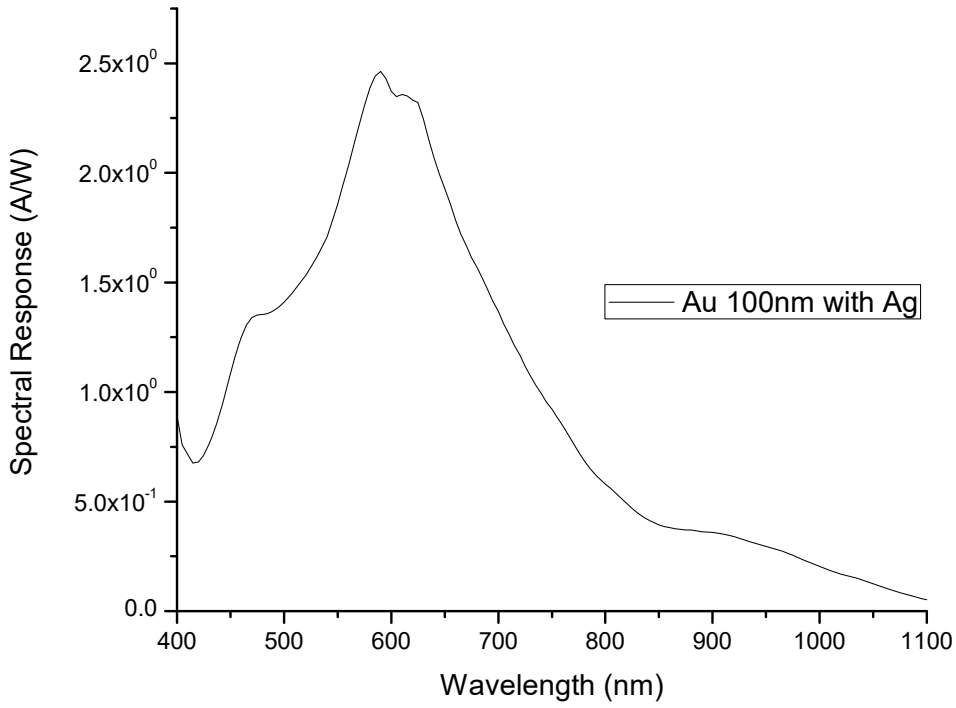

Figure 6.26 The spectral response of the plasmon FET with 25nm thick 100nm diameter Au disk patterns after the thermal reflow process with the deposited 5nm Ag.

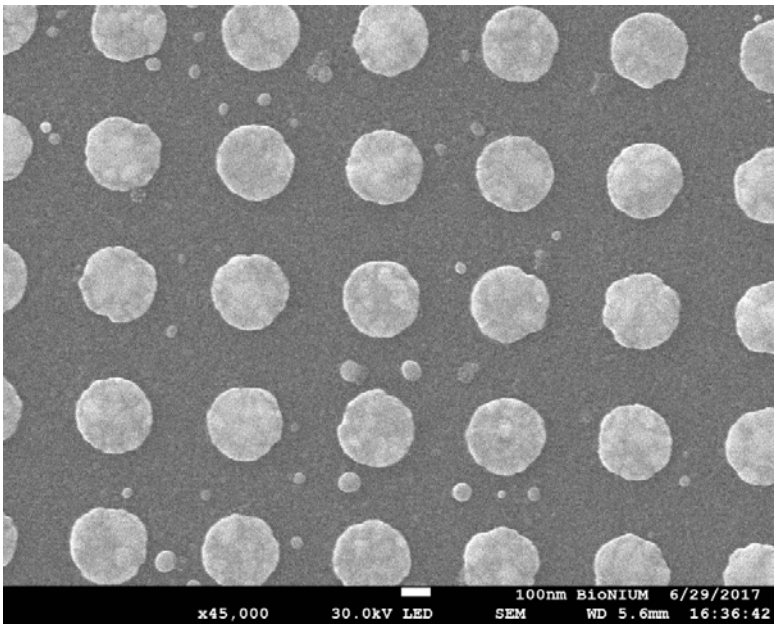

Figure 6.27 SEM image of the 25nm thick 300nm diameter Au disk patterns with 200nm separation after the thermal reflow process with the deposited 5nm Ag.

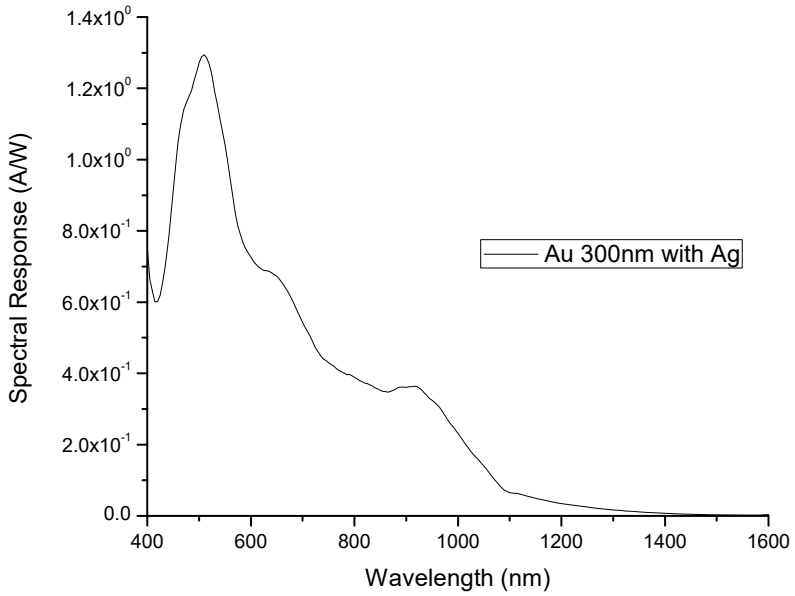

Figure 6.28 The spectral response of the plasmon FET with 25nm thick 300nm diameter Au disk patterns after the thermal reflow process with the deposited 5nm Ag.

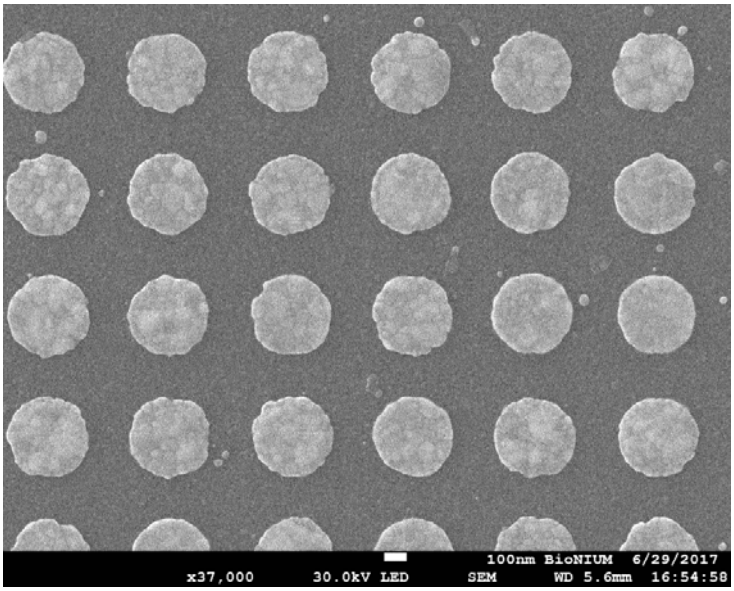

Figure 6.29 SEM image of the 25nm thick 400nm diameter Au disk patterns with the 200nm spacing after the thermal reflow process with the deposited 5nm Ag.

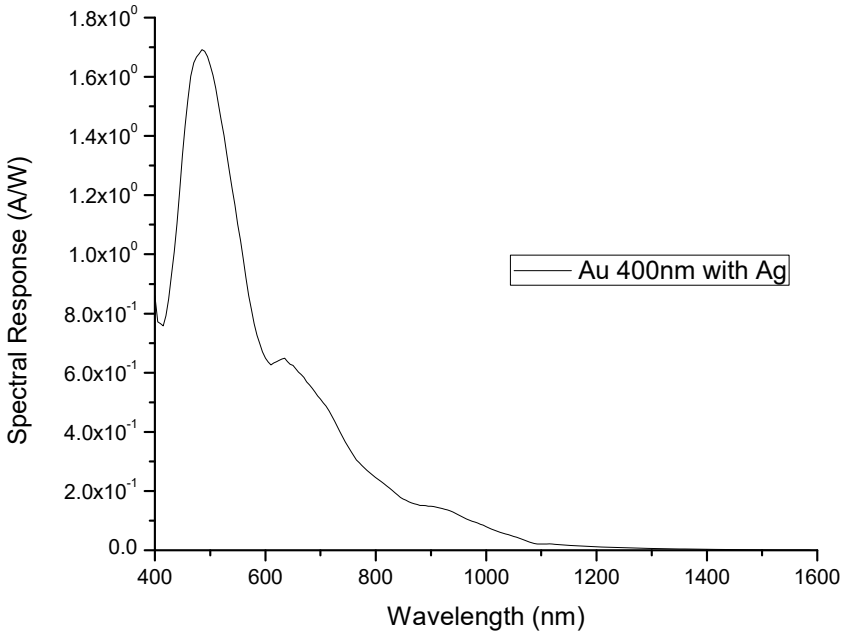

Figure 6.30 The spectral response of the plasmon FET with 25nm thick 400nm diameter Au disk patterns after the thermal reflow process with the deposited 5nm Ag.

Spectral Response with Different Nano Pattern Size and Thickness

We have successfully demonstrated plasmon detection in visible spectrum using gold nanoparticles as shown in Chapter 4. The thin gold film deposition and the thermal reflow method have been used for the plasmon FET that can detect within the visible range. Plasmonic nanostructures are important components to have a desired optical response in a plasmon FET. To move the plasmonic resonance to longer wavelengths, there could be two different approaches. The first approach is to change the size and/or shape of the plasmonic structure. Typically, the bigger plasmonic structure can stretch its plasmonic resonance to the longer wavelengths. We increased the nanodisk diameter up to 400nm and measured spectral response and simulated using the Lumerical solution software as shown in Figure 6.31.

A good match between the measurement and the simulation was observed. The diameter of nanodisks ranges from 50nm to 400nm. We also found a slight discrepancy of the peak wavelength between the simulation results and the experiment results. We analyzed the SEM images to find how the size of nanodisks after the heat treatment changed. The patterns shrunk after the annealing process. For example, Au 200nm disk in diameter with 25nm thickness became 187nm in diameter as shown in Figure 6.32. We simulated it again with the 187nm in diameter and 28.6nm thickness to keep the same Au volume. The spectral response peak changed from 929nm to 866nm as shown in the Figure 6.33.

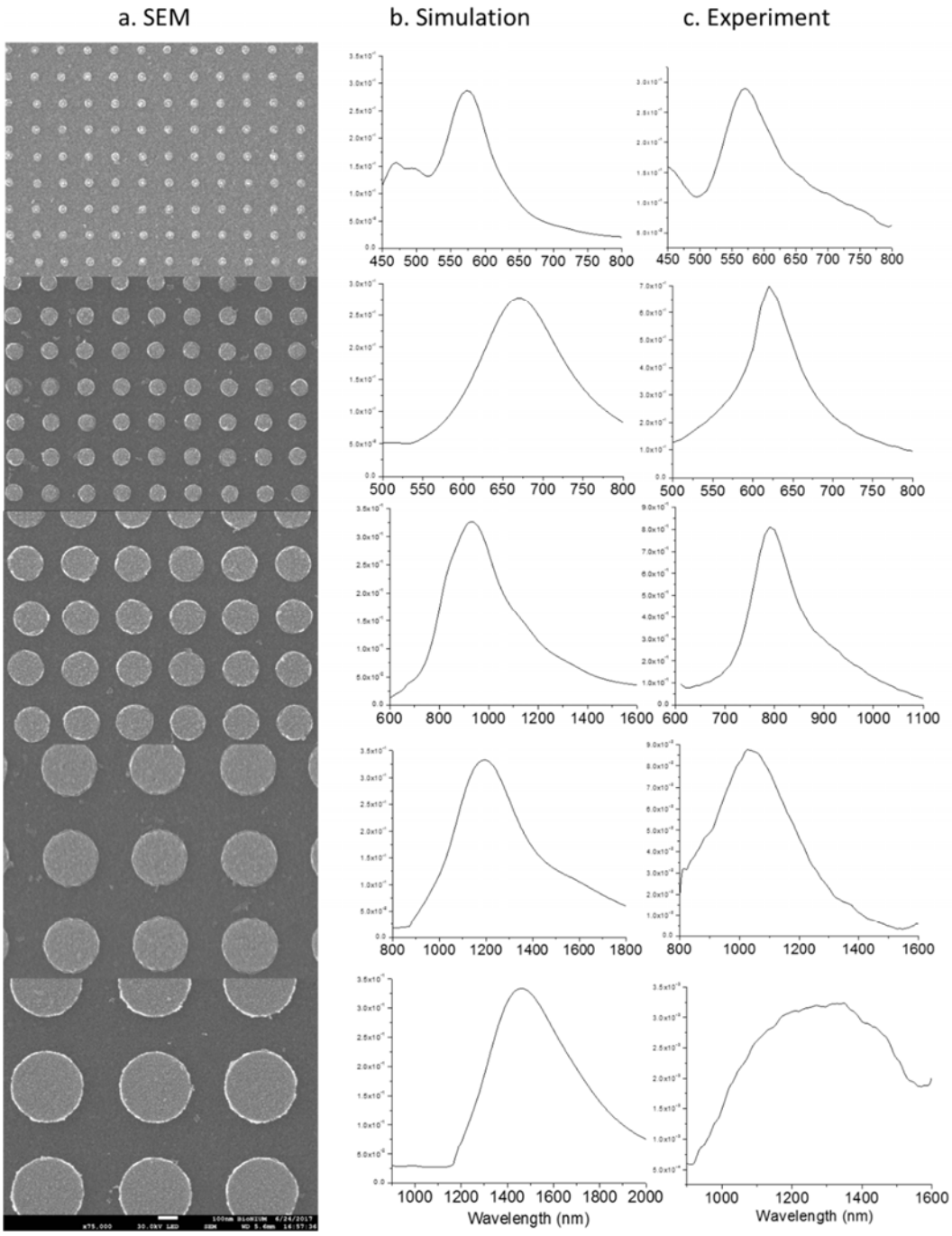

Figure 6.31 SEM images of the nanodisk patterns with the diameters of 50nm, 100nm, 200nm, 300nm, and 400nm in the plasmon FETs. Scale bar is 100 nm. (a) Experimentally measured device spectral response for the plasmon FETs (c), and corresponding theoretical calculation results (b).

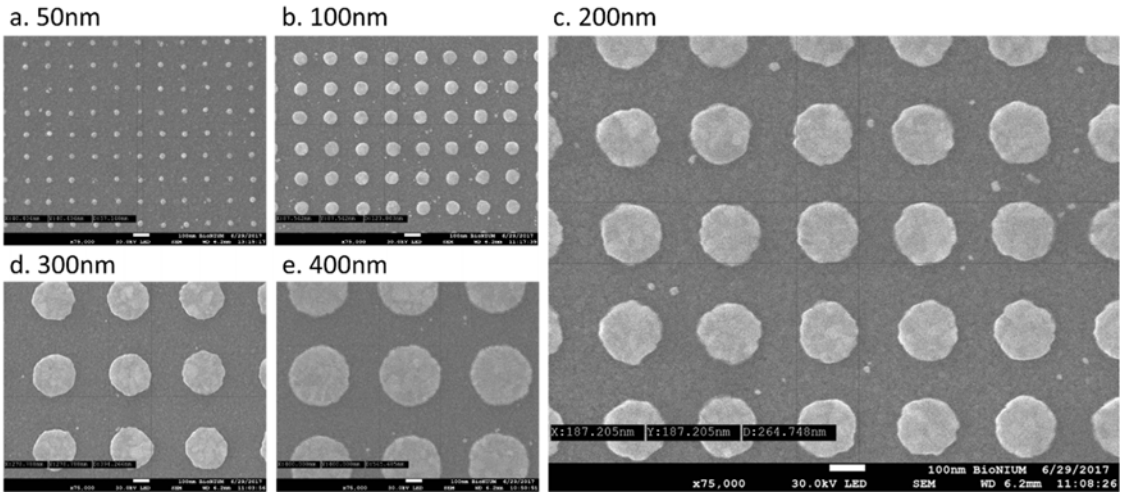

Figure 6.32 SEM images of 50nm (a), 100nm (b), 200nm (c), 300nm (d), and 400nm (e) disks in diameter after annealing process. Scale bar is 100 nm.

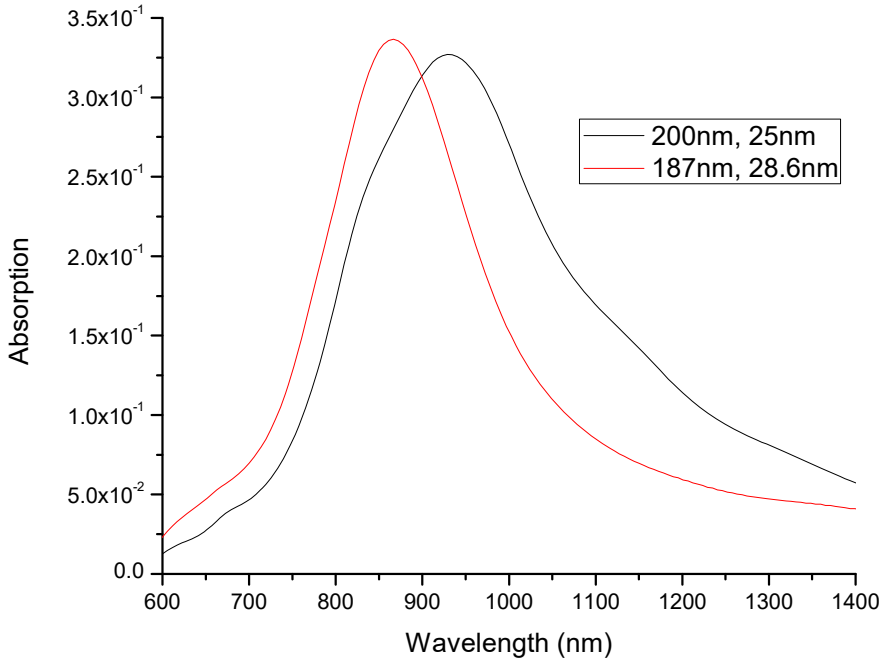

Figure 6.33 The theoretical calculation results of the absorption for the plasmon FET with the 25nm thick 200nm diameter Au disk patterns (black) and the 28.6nm thick 187nm diameter Au disk patterns (red).

We still have a difference in the response peak between the simulation of 187nm in diameter with 28.6nm thick nanodisk and the experimental result, which has the spectral response peak at 790nm wavelength. We tilted the device and took the SEM images again to see the shape of the disk pattern. We found that the center of the disk is thicker than the edge of the disk pattern as shown in Figure 6.34.

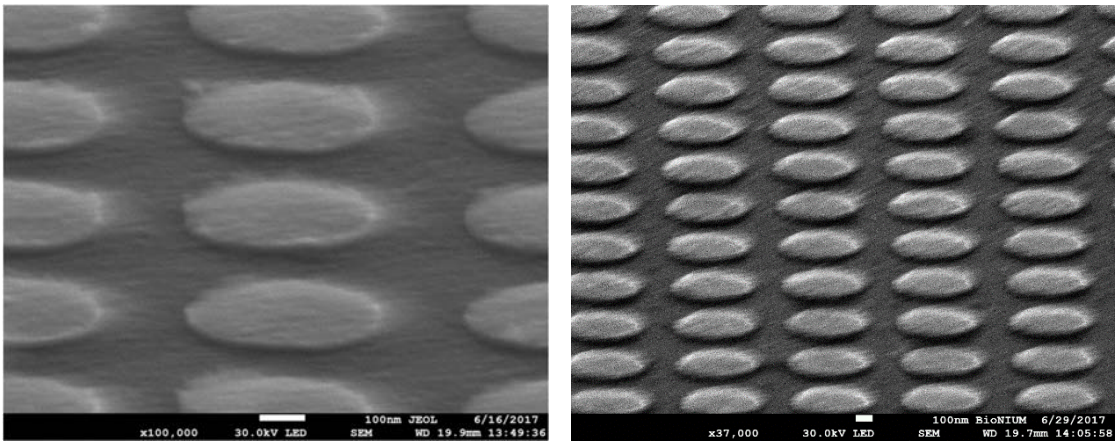

Figure 6.34 The SEM images of nanodisk patterns at a 70˚ tilt angle.

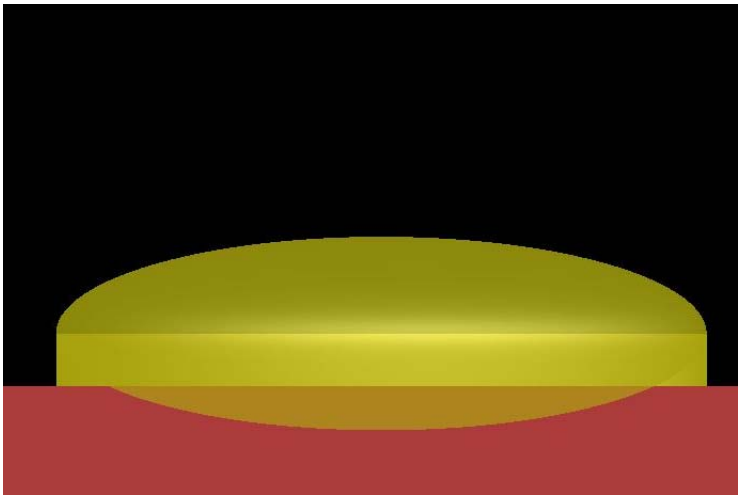

Figure 6.35 The modified simulation design of the nanodisk pattern with the 38nm center and the 10nm edge in thickness.

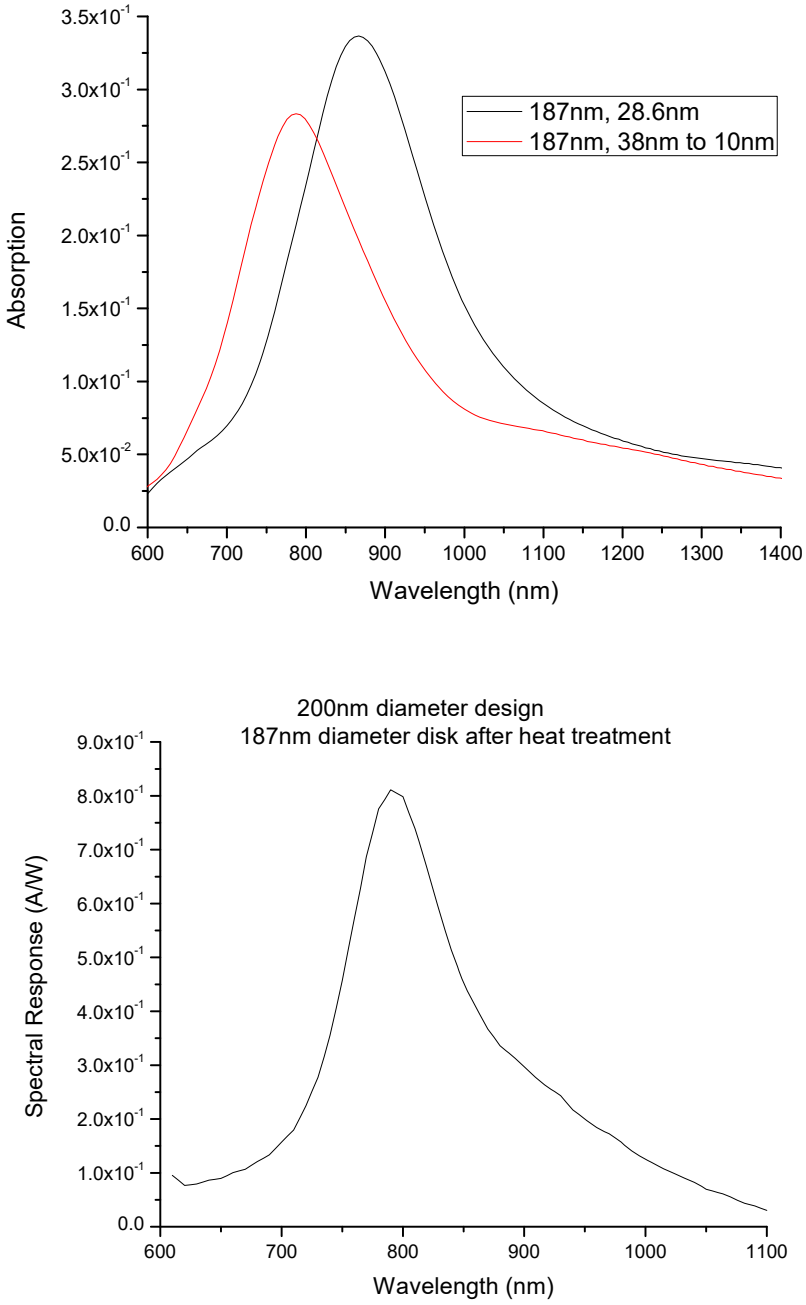

Figure 6.36 The calculated absorption of 187nm diameter disk patterns with different thickness (black line: 28.6nm and red line: 38nm center, 10nm edge) (top) and the measured spectral response of designed disk patterns with a 200nm diameter (bottom).

We designed the 187nm in diameter nano-disk pattern with a 38nm center height and a 10nm edge height to keep the Au volume constant as shown in Figure 6.35. The simulation result has blue-shifted and was nearly identical to the experiment result as shown in the Figure 6.36. We thus conclude that top and bottom surfaces of nano-disk patterns after annealing change to more of ball shape through the SEM image and the spectral response. Therefore, we have a better understanding of the expected spectral response with our fabrication process. And this confirmed model can be used for future studies.

Spectral Response with Different Host Materials Surrounding Au patterns

Here we focus on the relationship between the peak wavelength and the surrounding refractive index around the gold nanostructures. LSPR occurs when the metal structure (0-dimensional structure) is much smaller than the wavelength of the light. There is a specific energy (i.e. wavelength) that makes the electrons in the metal resonate by absorbing the photon energy [105]. Therefore, there is a strong absorption near a particular wavelength and the related equation (6.5) shows that the absorbance is sensitive to the refractive indices of the host matrix as shown in Figure 6.37.

$$\sigma_{ext}(\lambda) = 18\frac{\pi}{\lambda}\varepsilon_H^{'3/2} V_M \frac{\varepsilon_M^{''}(\lambda)}{[\varepsilon_M^{'}(\lambda) + 2\varepsilon_H^{'}]^2 + \varepsilon_M^{''}(\lambda)^2} \quad (6.5)$$

Where λ=wavelength, ε'_H is the dielectric constant of the surrounding medium, $\varepsilon = \varepsilon'_M + i\varepsilon''_M$ is the complex dielectric constant of the bulk metal.

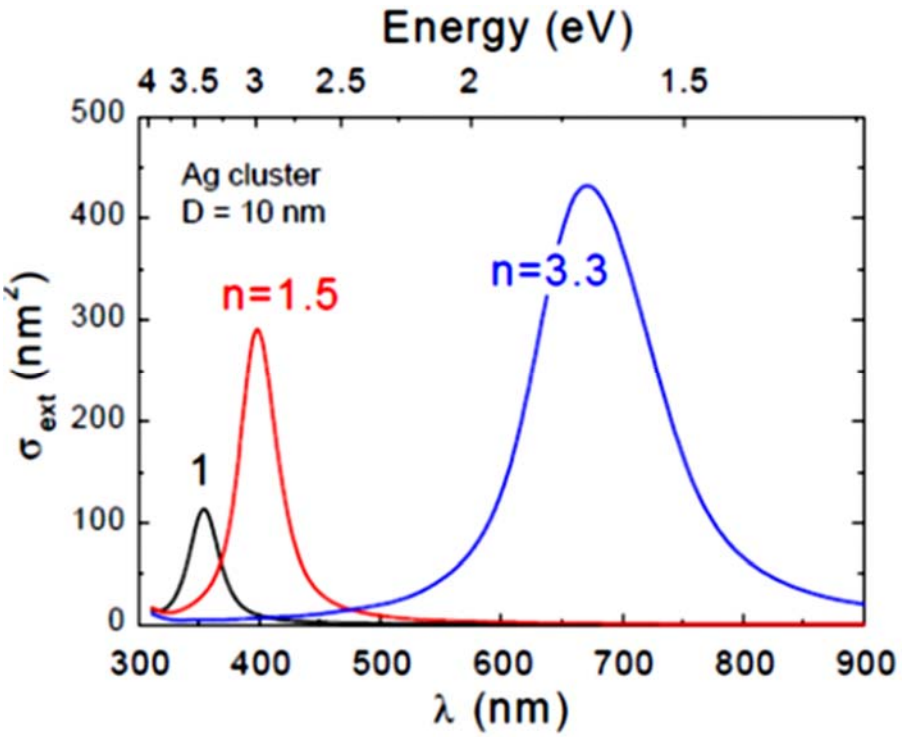

Figure 6.37 The resonance wavelength red-shifts when the refractive indices of the host matrix and the metal nanostructure increase.

We used gold nanoparticles deposited glass substrate to detect the changes in surrounding refractive index of gold nanoparticles. First, the plasmonic absorbance of gold nanoparticles on a glass substrate was measured. Next, we carried out an experiment by manipulating the refractive index surrounding the gold nanoparticles using lectin. The lectin has a higher refractive index than air. The lectin coated gold nanoparticle increases the average bulk refractive index and consequently induces an 18nm red shift in the plasmonic absorption spectrum as shown in Figure 6.38.

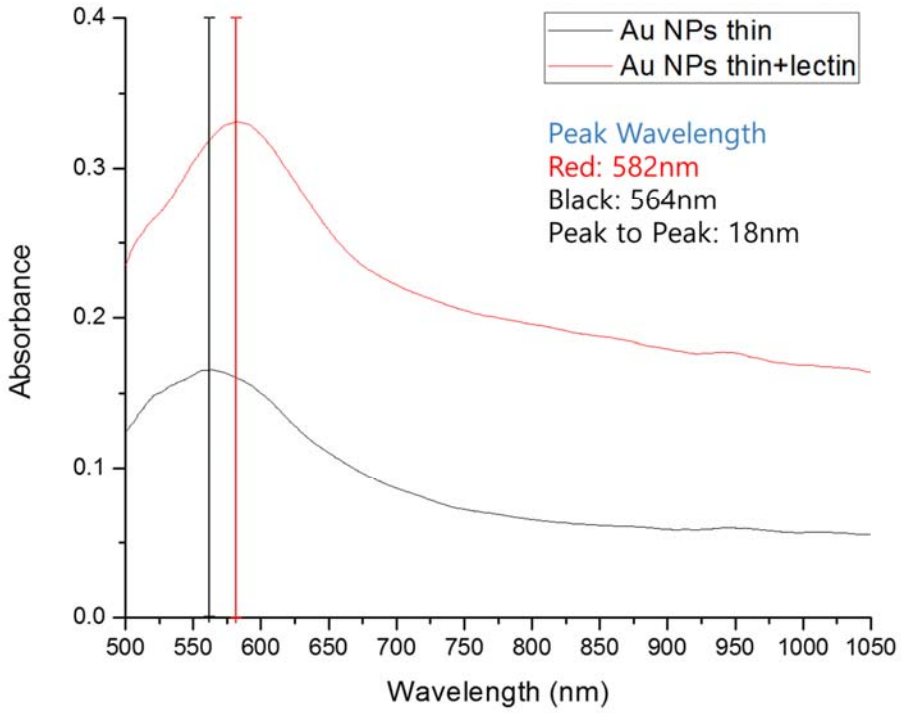

Figure 6.38 The absorbance of the gold nanoparticles (black) and the gold nanoparticles combined with the lectin (red).

The dielectric constant of surrounding medium can be increased to make red-shift of the plasmonic resonance. Typically, the high refractive index can move the plasmonic resonance to the longer wavelengths. The experiment used ZnO (n = 2.0034 at 587nm wavelength), and Polymethyl Methacrylate (PMMA, n = 1.4906 at 587nm wavelength) to manipulate the refractive index surrounding the gold nanopatterns. Plasmon FET was prepared using EBL as shown in Figure 6.39 (a) and the device structure is shown in Figure 6.39 (c). It was supposed to change the dielectric constant of host materials surrounding gold nanostructures. However, the sputtered ZnO on top of the plasmon FET was not even as shown in the Figure 6.39 (b).

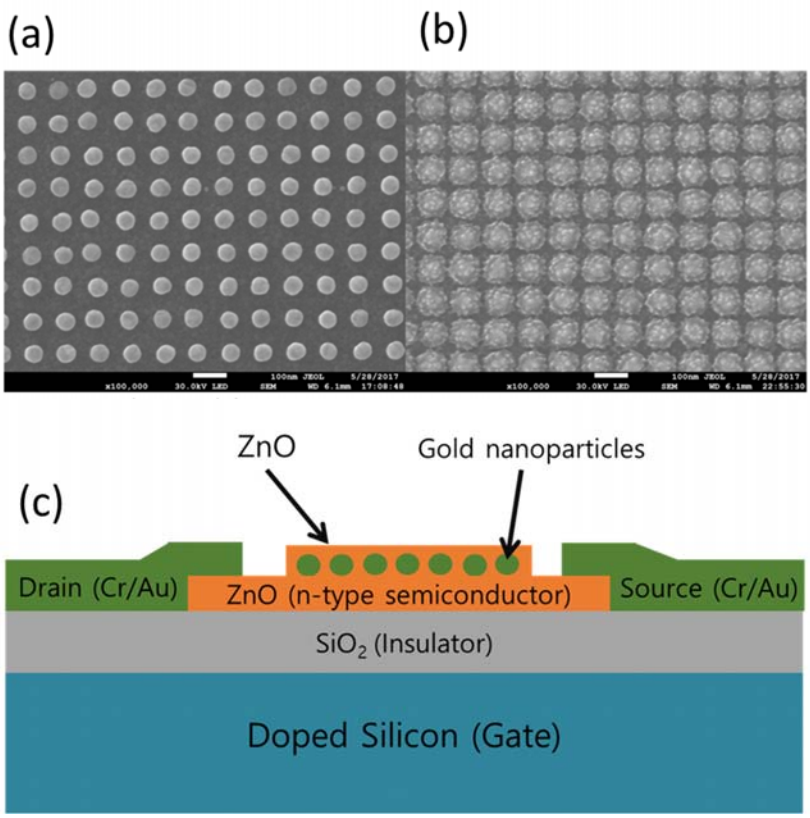

Figure 6.39 SEM images of the gold nanodisk patterns on top of the ZnO layer before (a) and after (b) the additional sputtered ZnO layer (50nm in thickness). Scale bar is 100nm. The device structure of the plasmon FET that has the gold nanodisks covered by ZnO that has a higher refractive index than air (c).

We spin-coated a layer of PMMA on the plasmon FET and have the spectral response with for Au with 100nm, 200nm and 300nm in diameter disk patterns with a 25nm thickness as shown in Figure 6.40 ~ 6.42 respectively. The resonance wavelength red-shifts by changing the surrounding material of the gold nanoparticles in the plasmon FET because it changes the dielectric constant surrounding the gold nanostructures. We can change the dielectric constant of host materials surrounding gold nanostructures with a higher refractive index to make the wavelength red shift much more.

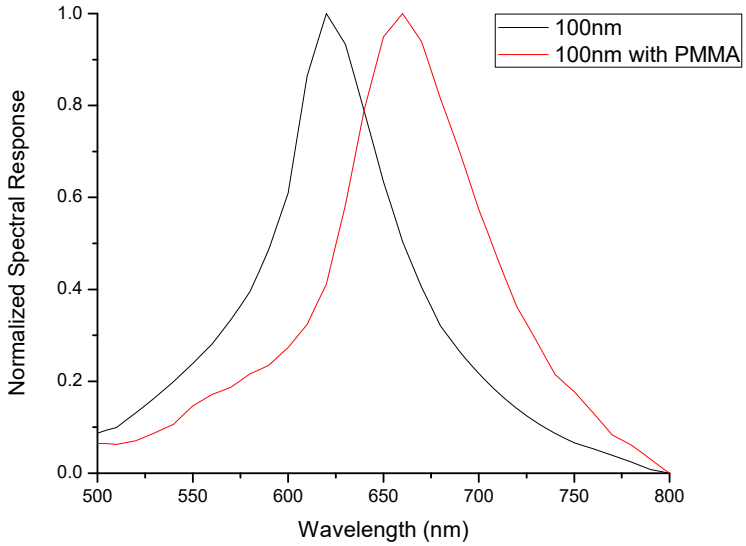

Figure 6.40 Normalized spectral response of 100nm disk pattern (black, 620nm peak wavelength) and with PMMA coating on top (red, 660nm peak wavelength).

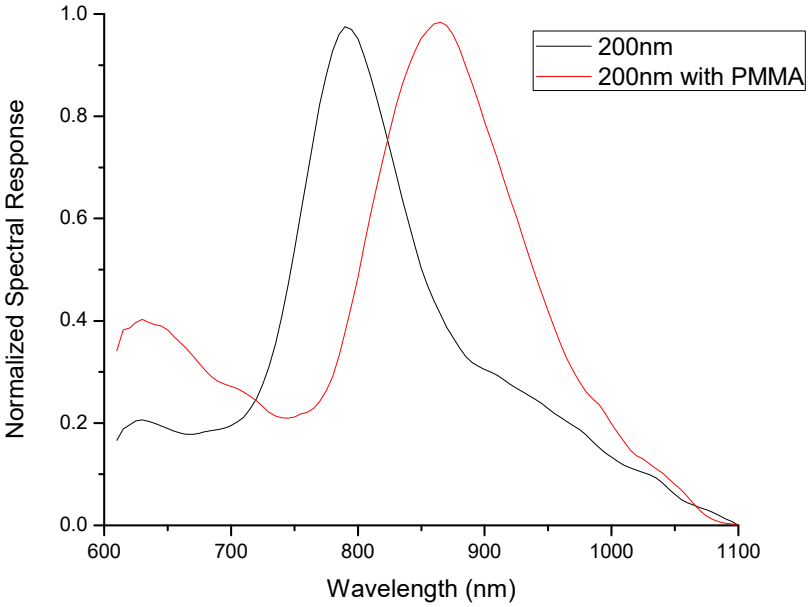

Figure 6.41 Normalized spectral response of 200nm disk pattern (black, 790nm peak wavelength) and with PMMA coating on top (red, 870nm peak wavelength).

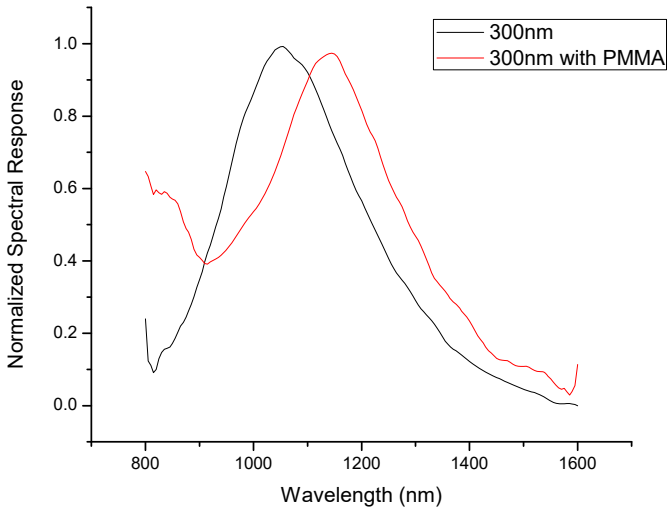

Figure 6.42 Normalized spectral response of 300nm disk pattern (black, 1050nm peak wavelength) and with PMMA coating on top (red, 1140nm peak wavelength).

Spectral Response of Plasmon FET at Different Gate Bias Voltages

To measure the plasmon FET response to an optical excitation, a lock-in amplifier system was used. The input wavelength-modulated light from a tungsten-halogen lamp was obtained through a monochromator. Then, the lock-in amplifier reads only generated plasmon induced current in plasmon FET regardless the DC drain current. The plasmon FET was biased to operate at the saturation region. The energy band diagram from gold NPs to gate electrode under saturation mode is described in Figure 6.43. At the plasmonic resonance frequency, the incoming photons excite electrons near the Fermi energy level of the Au NPs (Figure 6.43, ①). These excited hot electrons have enough energy to overcome the Schottky barrier formed by Au NPs and IGZO (Figure 6.43, ②). Applied gate bias voltage creates an electric field to collect free carriers in the IZGO and forms a channel for

drain current. At the same time, this gate voltage accelerates the entry of electrons into the FET current channel by generating a vertical electric field that produces a force to collect additional hot electrons from the Au NPs (Figure 6.43, ③). If there is no electric field by the gate bias, the hot electron transport is mainly from diffusion inside the ZnO to reach the current channel. This results in decreased hot electron collection due to the recombination process. But the internal electric field generated by the gate bias enables efficient transport of the plasmonic hot electrons to the channel area (Figure 6.43, ④) [102]. Copyright (2016) Society of Photo Optical Instrumentation Engineers.

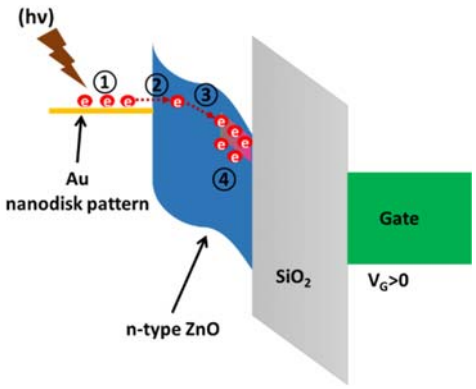

Figure 6.43 Energy band diagram of Au/IGZO/SiO2 with applied gate voltage, hv presents the energy of the incident photon [102]. Copyright (2016) Society of Photo Optical Instrumentation Engineers.

As shown in Figure 6.44 ~ 6.46, the spectral response of the plasmon FET is amplified as increasing the gate bias, because the stronger gate bias increases collection of hot electrons. In addition, the gate bias voltage causes band modification which increases the probability of quantum tunneling effect at the junction of Au/ZnO, resulting in more efficiency of plasmonic energy detection [102]. Copyright (2016) Society of Photo Optical Instrumentation Engineers.

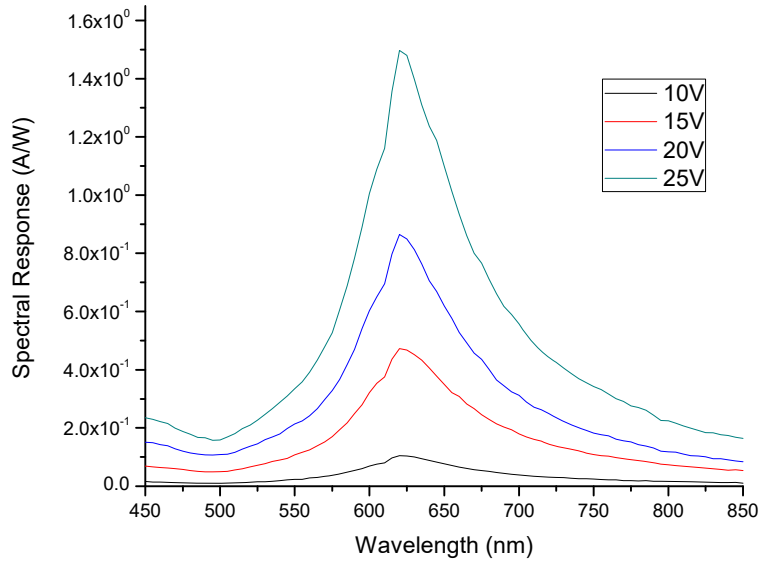

Figure 6.44 Spectral response (A/W) of plasmon FET with the 100nm diameter disk patterns at different gate bias voltages.

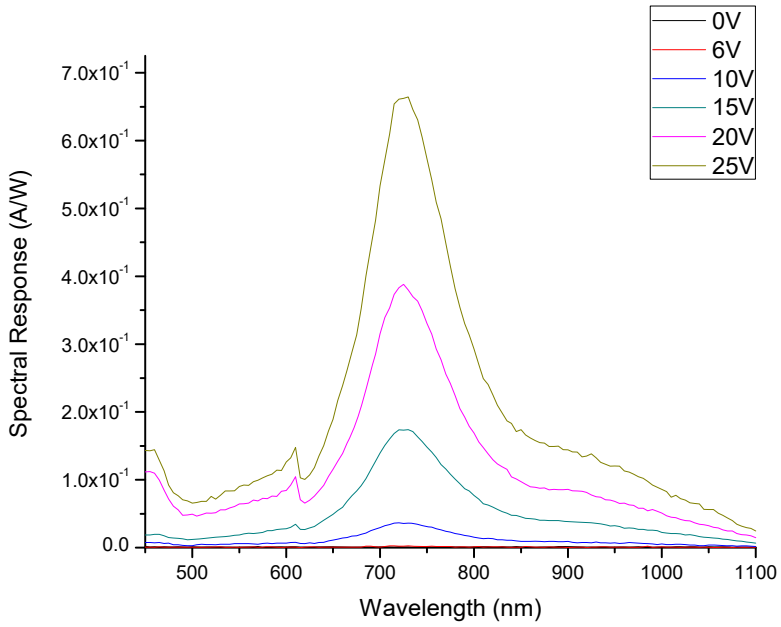

Figure 6.45 Spectral response (A/W) of plasmon FET with the 200nm diameter disk patterns at different gate bias voltages.

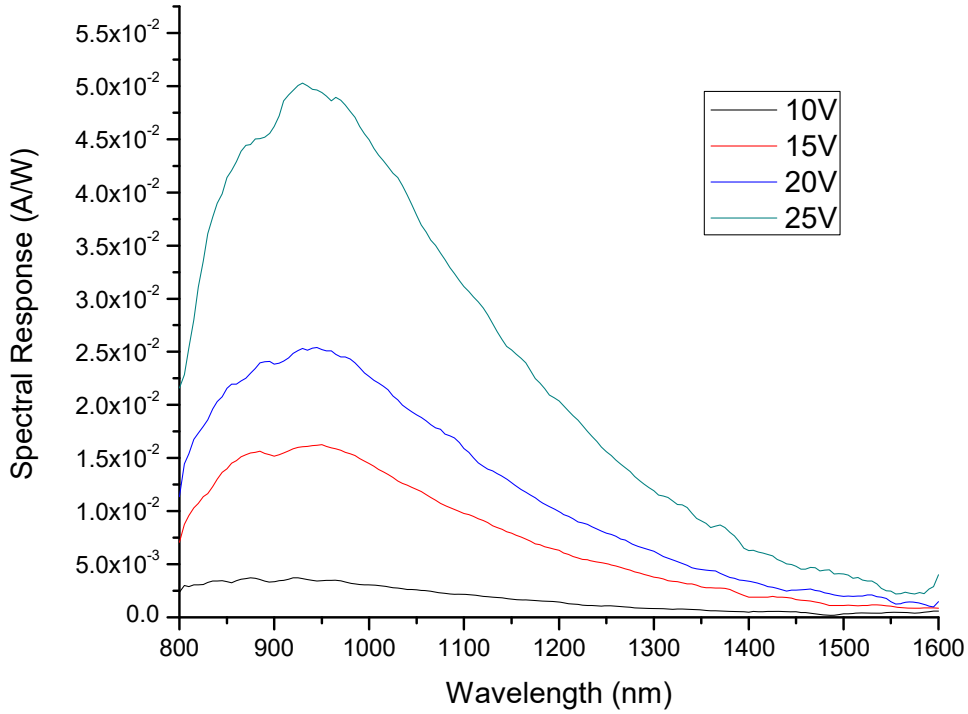

Figure 6.46 Spectral response (A/W) of plasmon FET with the 300nm diameter disk patterns at different gate bias voltages.

Spectral Response with Combined Two and Three Au Nanodisk Patterns

One of the important aspects of the plasmonic hot electron detection is the effect of the position of gold nanoparticles in the plasmon FET. In Chapter 4, we studied dependency of the nanoparttern position on the active channel of the TFT. The spectral response of the gold nanoparticles near the source contact was 31% higher than the response of the plasmon FET with gold nanoparticles near the drain contact because of the stronger vertical electric field near the source contact. The size and the location of nanostructures can be easily controlled by using electron beam lithography. We combined two patterns such as 100nm and 200nm disks patterns in a plasmon FET as shown in Figure 6.47.

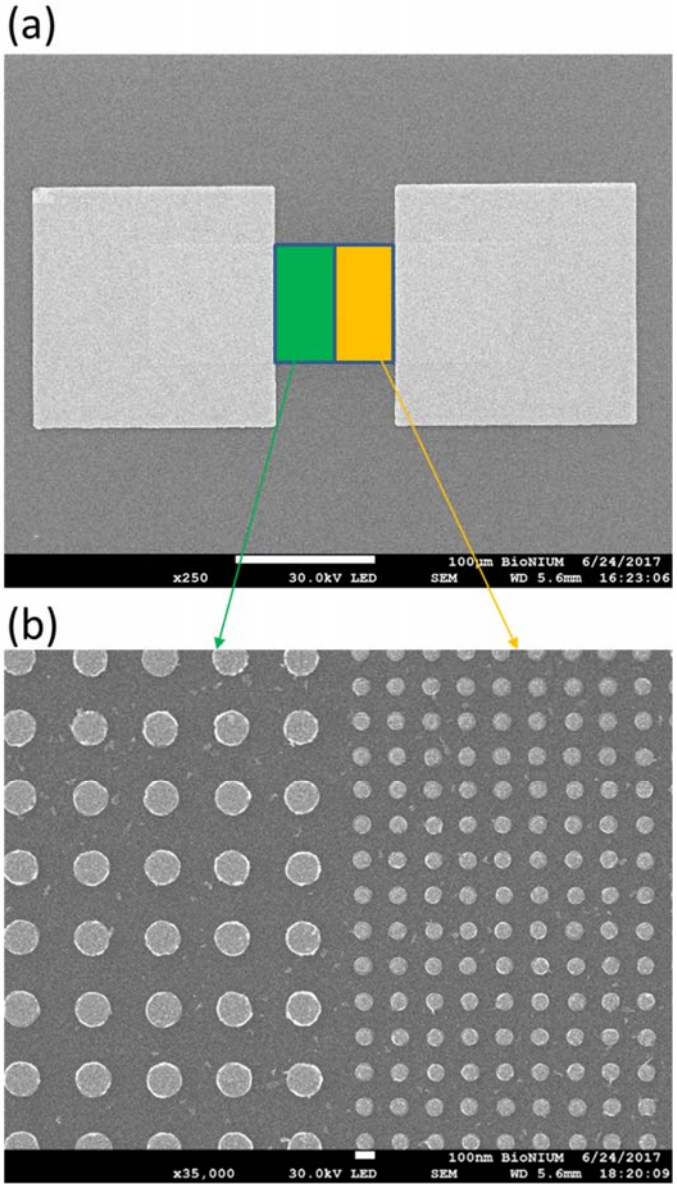

Figure 6.47 SEM images of the plasmon FET of the combined 100nm and 200nm disk patterns with the magnification of x250 (a) and x35,000 (b).

The spectral responses of the combined 100nm disks near the source contact and 200nm disk patterns near the drain contact were measured and the spectral response is shown in Figure 6.48. Then, the position of the source and the drain was switched and the

measured spectral response is shown in Figure 6.49. This measured data confirms the positional effect of gold nanopatterns in the plasmon FET. The plasmonic photocurrent of the device with 100nm nanopatterns near the source contact is 0.68A/W at peak wavelength while this value decreases to 0.51 A/W when the nanopatterns are located near the drain contact. Also, the spectral responses on plasmon FET with 200nm nanopatterns near the source contact is 0.46A/W at peak wavelength while this value decreases to 0.35 A/W when the nanopatterns are located near the drain contact. The experimental results confirm that the position of the plasmonic nanostructures should be considered for hot electron transport in a semiconductor area, and the built-in electric field in the device facilitates the collection of hot electrons when we combine different size patterns to control the generated photocurrent.

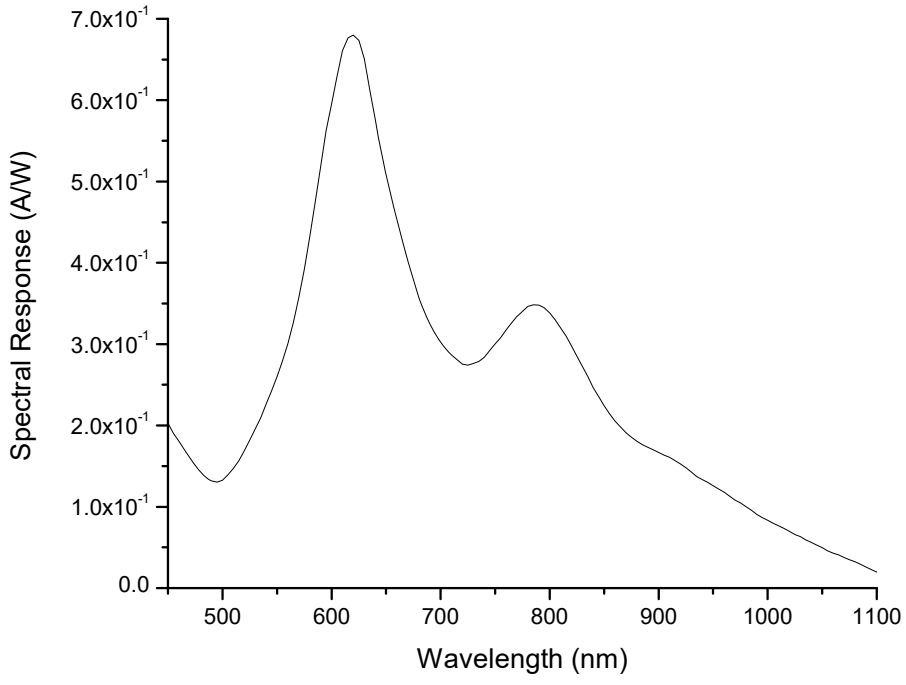

Figure 6.48 The spectral response of the combined 100nm disks near the source contact and 200nm disk patterns near the drain contact.

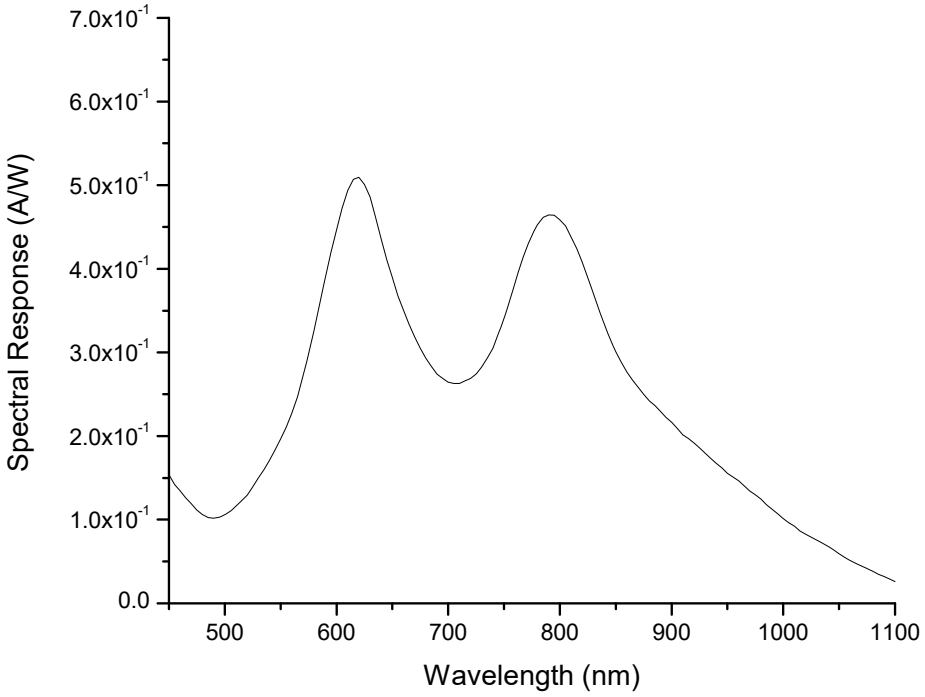

Figure 6.49 The spectral response of the combined 200nm disks near the source contact and 100nm disk patterns near the drain contact.

Finally, we fabricated a plasmon FET to achieve a spectral response from 450nm to 1600nm in wavelength, taking into account both the internal electric field and the number of particles. The area and the position of each nanopattern were considered by following the earlier results. In Chapter 4, we studied that the generated photocurrent is directly proportional to the area of gold nanoparticles. As a matter of fact, the number of nanodisks instead of the area is proportional to the spectral response. In addition, the plasmonic loss in gold was concerning at the spectral range for mid-IR. The area ratio of 100nm, 200nm, and 300nm patterns in diameter is 1 : 1 : 8 and the 300nm patterns are located near the source electrode as shown in Figure 6.50. And then the measured spectral response is shown in Figure 6.51.

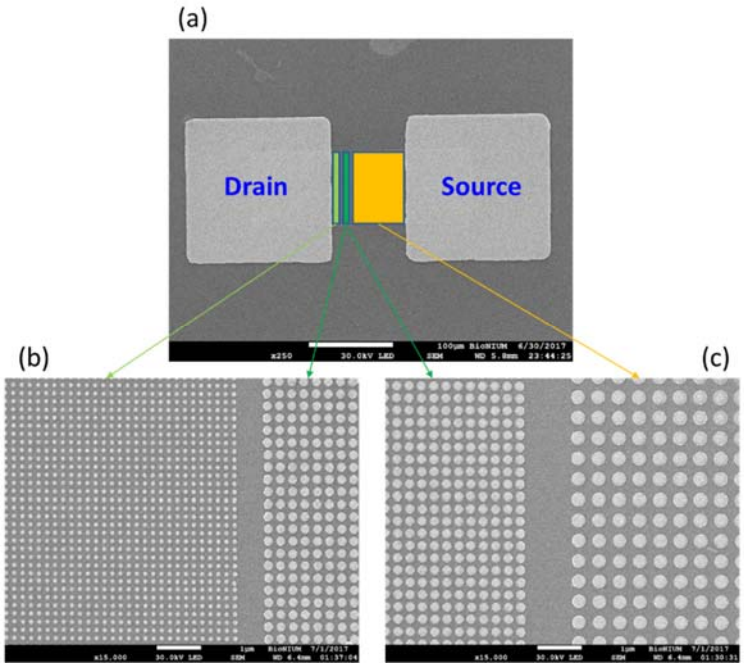

Figure 6.50 SEM images of the plasmon FET to achieve a spectral response from 450nm to 1600nm in wavelength (a), 100nm and 200nm patterns (b), and 200nm and 300nm patterns (c) on the ZnO layer.

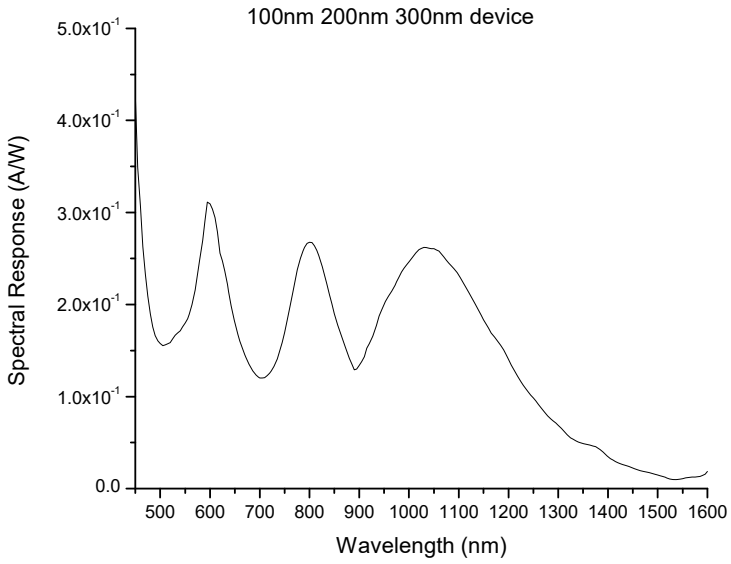

Figure 6.51 The spectral response of the plasmon FET incorporated with Au 100nm, 200nm and 300nm nanopatterns in diameter.

In previous work, we optimized the spacing between two nanodisk patterns according to the nanodisk diameter. It was determined that for the electron beam lithography, exposure, developing, and lift-off processes, 100nm, 200nm, and 300nm disk patterns in diameter needed 100nm, 100nm, and 200nm distances between each pattern, respectively as shown in Figure 6.52. Using these designs, the density ratio of nanopatterns in the same area is 25 (100nm) : 11 (200nm) : 4 (300nm).

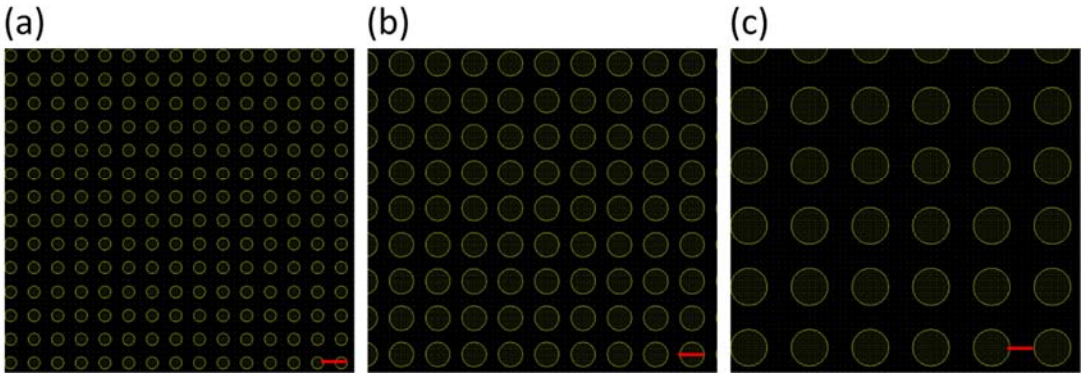

Figure 6.52 The designs of 100nm (a), 200nm (b), and 300nm (c) nanodisk patterns in diameter with a separation of 100nm, 100nm and 200nm, respectively. Scale bar is 200nm.

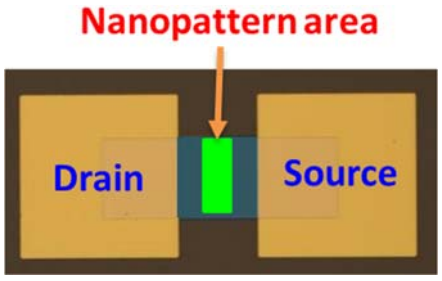

Figure 6.53 The schematic of the device that has the nanopattern area in the center of the active area.

When we consider both the number of nanopatterns and the area of a nanopattern, the spectral response ratio is supposed to be 2.5 (100nm) : 4.4 (200nm) : 3.6 (300nm).

Furthermore, when we also consider the loss intrinsic to larger Au nanodisk, the spectral response ratio of the plasmon FETs is 5.9 (100nm) : 4.0 (200nm) : 0.45 (300nm) when the nanopatterns are located in the center of the ZnO layer as shown in Figure 6.53. When the position of the patterned area is shifted from the center to closer to the source electrode, the spectral response increases around 10~15% depending on the pattern and the distance shifted. All things considered, the spectral response from 450nm to 1600nm spectrum was detected using the plasmon FET device.

Summary

We used silver to make nanostructure using the same thermal reflow method and the silver nanoparticles have the diameters between 10-100nm. The LSPR of the silver nanoparticles occurs at shorter wavelength than the case of gold nanoparticles. The spectral response of the silver nanoparticles can cover from 400nm to 500nm that the gold nanoparticles cannot cover.

It is too difficult to fabricate different size of gold NPs using a thermal reflow method with the different conditions such as thickness of metal and annealing temperature. We succeeded to control the nanoparticle size and shape using the Electron Beam Lithography. We changed the size and shape to get a red shift in spectral response. The nanostructures deposited on top of the thin film layer were not densely aggregated on the surface. This poor aggregation may cause weak adhesion of gold nanostructures to the film, consequently, hindering the electron transfer from metal to the layer. After annealing, the nanostructures have the better spectral response.

We increased the gold thickness up to 25nm to minimize the deformation of the nanopatterns and to get sharp plasmon resonance peak after annealing. Asymmetry patterns such as nanorods and nanowires have limited coupling to plane light source and the polarization dependence. So, we selected disk shaped patterns due to its reduced distortion and no polarization dependency. The patterns shrunk after the annealing process. For example, Au 200nm disk in diameter became 187nm in diameter and changed to more of ball shape. We found that the center of the disk is thicker than the edge of the disk pattern. To investigate how much gold-nanostructures expand their spectral response toward the IR regime, we fabricated plasmon FETs with diameter sizes of 100nm, 200nm, 300nm, and 400nm disk patterns and measured the spectral responses of the plasmon FETs. Furthermore, we checked the loss intrinsic to larger Au nanodisk, the spectral response ratio of the plasmon FETs is 5.9 (100nm) : 4.0 (200nm) : 0.45 (300nm). The 400nm nanostructures show very weak spectral response, 200 times less compared with the 200nm disk patterns

Also, the 200nm diameter gold nanodisk patterns was fabricated and the thermal reflow method was processed with the deposited 5nm silver. The spectral response has two resonance peaks by Ag NPs and Au nanodisks. The second peak increased 3 times compared with the Au 200nm disk patterns without Ag. The which is surrounded on the metal nanopatterns surrounded by the higher refractive index material can changed the plasmonic resonance to the longer wavelengths. We used Polymethyl Methacrylate (PMMA, n = 1.4893 at 620nm, 1.4849 at 790nm, and 1.4817 at 1050nm wavelength). The red-shift increased in longer wavelength.

Finally, we fabricated a plasmon FET to achieve a spectral response from 450nm to 1600nm in wavelength, by combining three patterns such as 100nm, 200nm and 300nm disk patterns in a plasmon FET.

Chapter 7: CONCLUSION AND FUTURE WORKS

Plasmon FET is a hybrid device using a thin film transistor and nanostructures to detect the resonant plasmonic energy. In this dissertation, we focused on an efficient plasmon induced hot electron energy conversion mechanism with the plasmon field effect transistor. The plasmon FET efficiently transfers plasmon induced hot electrons from the noble metal nanostructures such as gold and silver to the semiconductor such as ZnO and IGZO. The injected hot electrons to the ZnO channel increases the drain current. We investigate the effect of gold nanoparticle density and the position of plasmonic nanostructures because of the gradient of internal electric field between drain and source.

Both the experimental results and the simulation results confirm the density and the position effect to improve the hot electron collection. Successful fabrication and operation of the plasmon FET was demonstrated using an electron beam lithography (EBL) method. The fabrication process was optimized to convert optical signals to electrical signals for an ultra-wide spectral response (400nm - 1.6μm). A comprehensive spectral response study was performed and the fabricated plasmon FET was measured with various nanopatterns. Measurement results were compared with theoretical calculations. Finally, a visible to near infrared (NIR) detector was designed, fabricated, and measured. We can use the fabricated plasmon FET as an ultra-wide band detector from visible to near-IR wavelengths under normal, room temperature condition.

Plasmonic Nanostructures using Highly Doped Oxide Metals

Tailored metal plasmonic nanostructures were designed to have an efficient spectral response in the visible to near-IR (up to 1.6μm) wavelengths. Since the plasmonic loss in

gold is significant in the near-IR spectral range, we can design the plasmonic nanostructures using alternative materials such as ITO, Al doped ZnO (AZO) or Ga doped ZnO (GZO). The plasma frequency depends on the carrier concentration in the material. Semiconductors and conducting oxides have lower carrier concentrations than noble metals and the carrier concentration can be controlled depending on the growth (or deposition) condition.

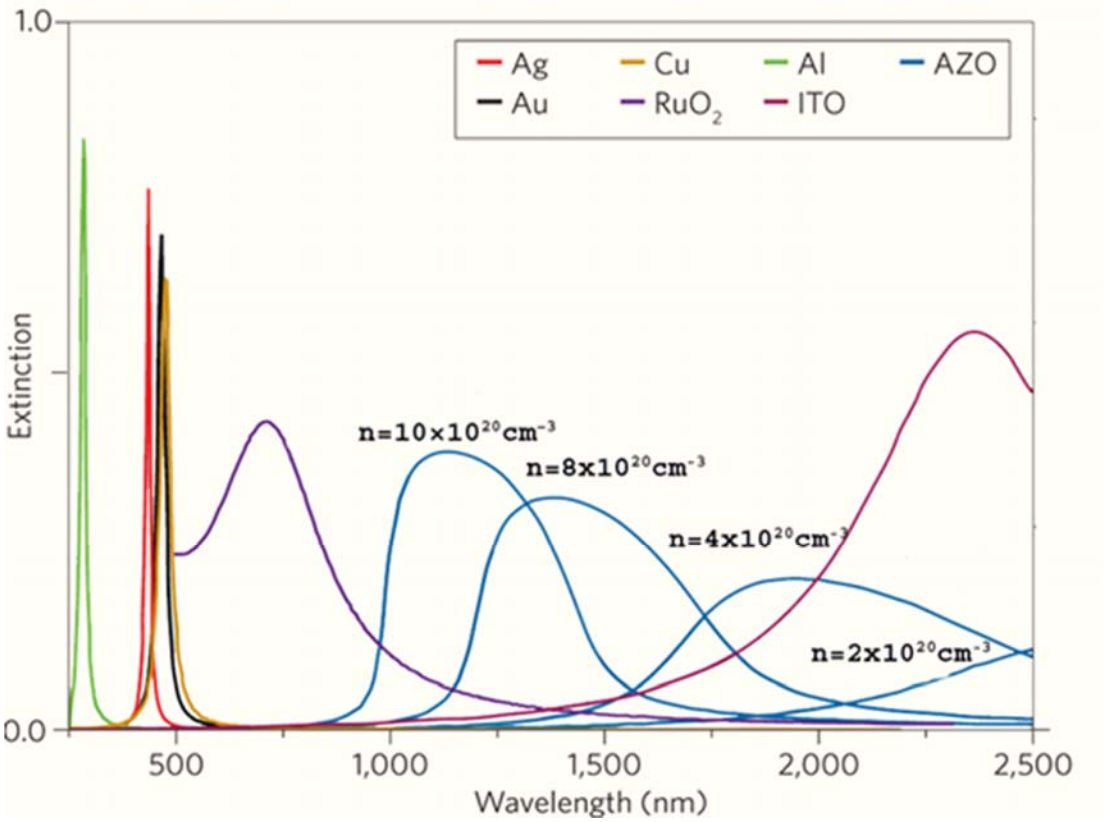

Figure 7.1 Optical extinction of metal (Al, Ag, Au and Cu) and conducting oxides (RuO2, AZO and ITO) plasmonic nanostructures. AZO shows tunable plasmonic absorption by changing its carrier concentration. The figure is reproduced from the reference [115].

Therefore, these materials are good candidates for the plasmonic nanostructure response in longer wavelengths since their lower plasma frequencies can move the plasmon resonance to the mid-IR range. For example, Aluminum doped ZnO (AZO) can have a plasmonic absorption range of 0.9 μm – 3 μm with a controlled carrier concentration range of 0.5–10 × 10^{20} cm^{-3}. And Ga-doped ZnO (GZO) can be tuned for plasmonic absorption up to 4.7 μm with a 1.14x10^{20} cm^{-3} carrier concentration as shown in Figure 7.1. Therefore, we will use three different materials (ITO, AZO and GZO) as an IR plasmonic antenna structure in Future works. Combining various sizes and geometries (such as a disk, rod, cross and so on), we expect even further extended IR plasmonic resonance using these proposed materials. In addition, we will use different dielectric host media to stretch the IR plasmonic spectrum to the targeted wavelength.

Integrated Device on a Si Substrate for an Ultra-Wide Spectral Response

In this paper, we presented the technique of lithography using EBL, with which we were able to fabricate structures as small as 25nm in diameter. EBL offers the best spatial resolution, allowing for various shapes and sizes, but EBL is a very expensive technique in comparison to other lithographic techniques such as the deep UV lithography (DUV) which has a similar spatial resolution as EBL. Therefore, we can use DUV to reduce fabrication costs in production. The active channel layers can be prepared on an un-doped Si substrate with a thermally grown SiO_2 layer to detect light up to 1100nm in wavelength without precise lithography. For absorption of larger wavelengths, we can fabricate larger nanopatterns or more than 200nm in diameter using DUV for detection in the NIR and IR regimes. This fabrication process entirely eliminates the need for EBL resulting in a low-cost and high yield batch.

Sensitive Bio-Sensor using Narrow Width at Half Maximum

Localized Surface Plasmon Resonance is a nanoscale phenomenon which presents strong resonance associated with noble metal nanostructures. Since LSPR is sensitive to the local refractive index changes, this sensitivity enables various sensing capabilities especially in biomedical applications such as target analyte binding to functionalized metal nanoparticles. The plasmon field effect transistor is a novel device which enables efficient detection and amplification of LSPR. The plasmon FET is capable of multiplexing and integration which is a solution for increased sensitivity and wide sensor dynamic range. We successfully demonstrated an antibody based sensor for a cancer biomarker with gold nanoparticles functionalized by a specific antibody. This novel antibody based sensor has several advantages such as extremely small size for integration and multiplexing, no need for complex optical geometry, and robust operation.

The gold nanoparticles employed in the first iteration of the plasmon FET used as a biosensor had a broad spectral response distribution and the Full Width at Half Maximum (FWHM) was around 200nm wide [69]. Various techniques have been proposed to enhance the performance of the SPR based sensor. One of the important factors that largely affect the performance of plasmonic sensing applications, such as LSPR biosensors, is the full-width at half-maximum (FWHM), the narrower the FWHM the higher the precision. Using EBL, 250,000 identical 100nm diameter Au disk nanopatterns can be incorporated in the plasmon FET resulting in an FWHM of just 25nm range due to the narrow distribution of particle sizes. The plasmon FET using EBL has a >87.5% narrower full-width at half-maximum than the previous device which used the thermal reflow method. With the 38% narrower FWHM, SPR sensors demonstrate a 22% higher sensitivity [116].

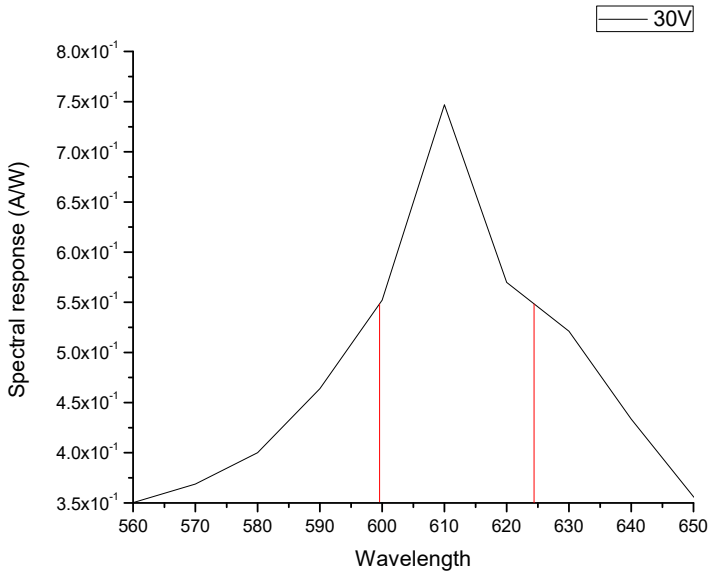

Figure 7.2 Spectral response (A/W) of plasmon FET with the 100nm diameter disk patterns at 30V gate bias.

REFERENCES

[1] T. A. Wertime, "Man's first encounters with metallurgy," *Science,* vol. 146, pp. 1664-1664, 1964.

[2] H. Bethe, "Theory of diffraction by small holes," *Physical Review,* vol. 66, p. 163, 1944.

[3] A. K. Azad and W. Zhang, "Resonant terahertz transmission in subwavelength metallic hole arrays of sub-skin-depth thickness," *Optics Letters,* vol. 30, pp. 2945-2947, 2005.

[4] U. Kreibig and M. Vollmer, "Theoretical considerations," in *Optical Properties of Metal Clusters*, ed: Springer, 1995, pp. 13-201.

[5] B. Y. Zheng, H. Zhao, A. Manjavacas, M. McClain, P. Nordlander, and N. J. Halas, "Distinguishing between plasmon-induced and photoexcited carriers in a device geometry," *Nature Communications,* vol. 6, 2015.

[6] M. L. Brongersma, N. J. Halas, and P. Nordlander, "Plasmon-induced hot carrier science and technology," *Nature Nanotechnology,* vol. 10, pp. 25-34, 2015.

[7] W. L. Barnes, A. Dereux, and T. W. Ebbesen, "Surface plasmon subwavelength optics," *Nature,* vol. 424, pp. 824-830, 2003.

[8] C. L. Haynes and R. P. Van Duyne, "Nanosphere lithography: a versatile nanofabrication tool for studies of size-dependent nanoparticle optics," ed: ACS Publications, 2001.

[9] U. Kreibig and M. Vollmer, *Optical properties of metal clusters* vol. 25: Springer Science & Business Media, 2013.

[10] C. Sönnichsen, S. Geier, N. Hecker, G. Von Plessen, J. Feldmann, H. Ditlbacher, *et al.*, "Spectroscopy of single metallic nanoparticles using total internal reflection microscopy," *Applied Physics Letters,* vol. 77, pp. 2949-2951, 2000.

[11] M. W. Klein, M. Wegener, N. Feth, and S. Linden, "Experiments on second-and third-harmonic generation from magnetic metamaterials," *Optics Express,* vol. 15, pp. 5238-5247, 2007.

[12] J. Henzie, M. H. Lee, and T. W. Odom, "Multiscale patterning of plasmonic metamaterials," *Nature Nanotechnology,* vol. 2, pp. 549-554, 2007.

[13] R. A. Pala, J. White, E. Barnard, J. Liu, and M. L. Brongersma, "Design of plasmonic thin-film solar cells with broadband absorption enhancements," *Advanced Materials,* vol. 21, pp. 3504-3509, 2009.

[14] V. E. Ferry, L. A. Sweatlock, D. Pacifici, and H. A. Atwater, "Plasmonic nanostructure design for efficient light coupling into solar cells," *Nano Letters,* vol. 8, pp. 4391-4397, 2008.

[15] A. Kabashin, P. Evans, S. Pastkovsky, W. Hendren, G. Wurtz, R. Atkinson*, et al.*, "Plasmonic nanorod metamaterials for biosensing," *Nature Materials,* vol. 8, pp. 867-871, 2009.

[16] S. Lal, S. Link, and N. J. Halas, "Nano-optics from sensing to waveguiding," *Nature Photonics,* vol. 1, pp. 641-648, 2007.

[17] X. Huang, I. H. El-Sayed, W. Qian, and M. A. El-Sayed, "Cancer cell imaging and photothermal therapy in the near-infrared region by using gold nanorods," *Journal of the American Chemical Society,* vol. 128, pp. 2115-2120, 2006.

[18] E. J. R. Vesseur, R. de Waele, M. Kuttge, and A. Polman, "Direct observation of plasmonic modes in Au nanowires using high-resolution cathodoluminescence spectroscopy," *Nano Letters,* vol. 7, pp. 2843-2846, 2007.

[19] J. Chen, M. Badioli, P. Alonso-González, S. Thongrattanasiri, F. Huth, J. Osmond*, et al.*, "Optical nano-imaging of gate-tunable graphene plasmons," *Nature,* vol. 487, pp. 77-81, 2012.

[20] Z. Fei, A. Rodin, G. Andreev, W. Bao, A. McLeod, M. Wagner*, et al.*, "Gate-tuning of graphene plasmons revealed by infrared nano-imaging," *Nature,* vol. 487, pp. 82-85, 2012.

[21] F. Wang and N. A. Melosh, "Plasmonic energy collection through hot carrier extraction," *Nano Letters,* vol. 11, pp. 5426-5430, 2011.

[22] Y. K. Lee, C. H. Jung, J. Park, H. Seo, G. A. Somorjai, and J. Y. Park, "Surface plasmon-driven hot electron flow probed with metal-semiconductor nanodiodes," *Nano Letters,* vol. 11, pp. 4251-4255, 2011.

[23] A. Sobhani, M. W. Knight, Y. Wang, B. Zheng, N. S. King, L. V. Brown*, et al.*, "Narrowband photodetection in the near-infrared with a plasmon-induced hot electron device," *Nature Communications,* vol. 4, p. 1643, 2013.

[24] G. L. Hansen, J. Schmit, and T. Casselman, "Energy gap versus alloy composition and temperature in Hg1− x Cd x Te," *Journal of Applied Physics,* vol. 53, pp. 7099-7101, 1982.

[25] D. Smith and C. Mailhiot, "Proposal for strained type II superlattice infrared detectors," *Journal of Applied Physics,* vol. 62, pp. 2545-2548, 1987.

[26] C. Grein, P. Young, and H. Ehrenreich, "Minority carrier lifetimes in ideal InGaSb/InAs superlattices," *Applied Physics Letters,* vol. 61, pp. 2905-2907, 1992.

[27] E. Youngdale, J. Meyer, C. Hoffman, F. Bartoli, C. Grein, P. Young*, et al.*, "Auger lifetime enhancement in InAs–Ga1− x In x Sb superlattices," *Applied Physics Letters,* vol. 64, pp. 3160-3162, 1994.

[28] L. J. Kozlowski, K. Vural, J. M. Arias, W. E. Tennant, and R. E. DeWames, "Performance of HgCdTe, InGaAs and quantum well GaAs/AlGaAs staring infrared focal plane arrays," in *Proc. SPIE*, 1997, pp. 2-13.

[29] W. Lu, L. Li, H. Zheng, W. Xu, and D. Xiong, "Development of an infrared detector: Quantum well infrared photodetector," *Science in China Series G: Physics, Mechanics and Astronomy,* vol. 52, pp. 969-977, 2009.

[30] N. K. Dhar, R. Dat, and A. K. Sood, "Advances in infrared detector array technology," in *Optoelectronics-Advanced Materials and Devices*, ed: InTech, 2013.

[31] A. Rogalski, *Infrared detectors*: CRC press, 2010.

[32] H. Shokri Kojori, J.-H. Yun, Y. Paik, J. Kim, W. A. Anderson, and S. J. Kim, "Plasmon Field Effect Transistor for Plasmon to Electric Conversion and Amplification," *Nano Letters,* vol. 16, pp. 250-254, 2016/01/13 2016.

[33] H. S. Kojori, "Plasmon field effect transistor: A novel sensing platform for biomedical applications," University of Miami, 2016.

[34] J. Jackson and N. Halas, "Silver nanoshells: variations in morphologies and optical properties," *The Journal of Physical Chemistry B,* vol. 105, pp. 2743-2746, 2001.

[35] M. W. Knight, H. Sobhani, P. Nordlander, and N. J. Halas, "Photodetection with active optical antennas," *Science,* vol. 332, pp. 702-704, 2011.

[36] Y. Nishijima, K. Ueno, Y. Yokota, K. Murakoshi, and H. Misawa, "Plasmon-assisted photocurrent generation from visible to near-infrared wavelength using a Au-nanorods/TiO2 electrode," *The Journal of Physical Chemistry Letters,* vol. 1, pp. 2031-2036, 2010.

[37] Q. Zhang, W. Li, C. Moran, J. Zeng, J. Chen, L.-P. Wen*, et al.*, "Seed-mediated synthesis of Ag nanocubes with controllable edge lengths in the range of 30–200 nm and comparison of their optical properties," *Journal of the American Chemical Society,* vol. 132, p. 11372, 2010.

[38] J. Zeng, S. Roberts, and Y. Xia, "Nanocrystal-Based Time–Temperature Indicators," *Chemistry–A European Journal,* vol. 16, pp. 12559-12563, 2010.

[39] L. J. Edgar, "Device for controlling electric current," ed: Google Patents, 1933.

[40] J. Lilienfeld, "US Patent# 1,745,175," *Method and Apparatus for Controlling Electric Currents, January,* vol. 28, 1930.

[41] J. Lilienfeld, "US Patent# 1,877,140," *Amplifier for Electric Currents, September,* vol. 13, 1932.

[42] O. Heil, "British Patent 439 457," *Application Filed,* vol. 4, 1935.

[43] R. G. Arns, "The other transistor: early history of the metal-oxide semiconductor field-effect transistor," *Engineering Science and Education Journal,* vol. 7, pp. 233-240, 1998.

[44] P. K. Weimer, "The TFT a new thin-film transistor," *Proceedings of the IRE,* vol. 50, pp. 1462-1469, 1962.

[45] L. Olsen, R. Bohara, and M. Urie, "Explanation for low-efficiency Cu2O Schottky-barrier solar cells," *Applied Physics Letters,* vol. 34, pp. 47-49, 1979.

[46] P. Weimer, "IRE-AICE Device Research Conference," ed: Stanford, CA, June, 1961.

[47] S. Cho, "Enhanced Optical and Electrical Properties of Organic Field Effect Transistor using Metal Nanoparticles," 2014.

[48] Y. Kuo, "Thin film transistor technology—Past, present, and future," *The Electrochemical Society Interface,* vol. 22, pp. 55-61, 2013.

[49] S. J. Fonash and G. Liu, "Low temperature crystallization and patterning of amorphous silicon films on electrically insulating substrates," ed: Google Patents, 1994.

[50] T. Sameshima, S. Usui, and M. Sekiya, "XeCl Excimer laser annealing used in the fabrication of poly-Si TFT's," *IEEE Electron Device Letters,* vol. 7, pp. 276-278, 1986.

[51] M. Mitani, T. Endo, Y. Taniguchi, T. Katou, S. Shimoto, T. Ohno, *et al.*, "Ultrahigh-performance polycrystalline silicon thin-film transistors on excimer-laser-processed pseudo-single-crystal films," *Japanese Journal of Applied Physics,* vol. 47, p. 8707, 2008.

[52] S. K. Hong, B. K. Kim, and Y. M. Ha, "41.1: Invited Paper: LTPS Technology for Improving the Uniformity of AMOLEDs," in *SID Symposium Digest of Technical Papers*, 2007, pp. 1366-1369.

[53] T. Kamiya, K. Nomura, and H. Hosono, "Present status of amorphous In–Ga–Zn–O thin-film transistors," *Science and Technology of Advanced Materials,* vol. 11, p. 044305, 2010.

[54] J. S. Park, W.-J. Maeng, H.-S. Kim, and J.-S. Park, "Review of recent developments in amorphous oxide semiconductor thin-film transistor devices," *Thin Solid Films,* vol. 520, pp. 1679-1693, 2012.

[55] K. Nomura, H. Ohta, A. Takagi, T. Kamiya, M. Hirano, and H. Hosono, "Room-temperature fabrication of transparent flexible thin-film transistors using amorphous oxide semiconductors," *Nature,* vol. 432, pp. 488-492, 2004.

[56] K. Takahashi, A. Yoshikawa, and A. Sandhu, *Wide bandgap semiconductors*: Springer, 2007.

[57] S. A. AHMED, "Prospects for Photovoltaic Conversion of Solar Energy," *Alternative Energy Sources,* p. 355, 2014.

[58] A. Facchetti and T. Marks, *Transparent electronics: from synthesis to applications*: John Wiley & Sons, 2010.

[59] D. Klimm, "Electronic materials with a wide band gap: recent developments," *IUCrJ,* vol. 1, pp. 281-290, 2014.

[60] R. Kirschman, *High-temperature electronics*: IEEE Press, 1999.

[61] B. Ozpineci and L. Tolbert, *Comparison of wide-bandgap semiconductors for power electronics applications*: Citeseer, 2004.

[62] R. Zia, J. A. Schuller, A. Chandran, and M. L. Brongersma, "Plasmonics: the next chip-scale technology," *Materials Today,* vol. 9, pp. 20-27, 2006.

[63] Z. Merali, "This 1,600-Year-Old Goblet Shows that the Romans Were Nanotechnology Pioneers (http://www.smithsonianmag.com)," *Smithsonian Magazine,* September, 2013.

[64] H. Hertz, "Ueber einen Einfluss des ultravioletten Lichtes auf die electrische Entladung," *Annalen der Physik,* vol. 267, pp. 983-1000, 1887.

[65] M. Planck, "Ueber das gesetz der energieverteilung im normalspectrum," *Annalen der Physik,* vol. 309, pp. 553-563, 1901.

[66] D. A. Neamen, *Semiconductor physics and devices*: McGraw-Hill Higher Education, 2003.

[67] O. Neumann, A. S. Urban, J. Day, S. Lal, P. Nordlander, and N. J. Halas, "Solar vapor generation enabled by nanoparticles," *Acs Nano,* vol. 7, pp. 42-49, 2012.

[68] Z. Fang, Y.-R. Zhen, O. Neumann, A. Polman, F. J. García de Abajo, P. Nordlander, *et al.*, "Evolution of light-induced vapor generation at a liquid-immersed metallic nanoparticle," *Nano Letters,* vol. 13, pp. 1736-1742, 2013.

[69] H. S. Kojori, Y. Ji, Y. Paik, A. B. Braunschweig, and S. J. Kim, "Monitoring interfacial lectin binding with nanomolar sensitivity using a plasmon field effect transistor," *Nanoscale,* vol. 8, pp. 17357-17364, 2016.

[70] K. Okamoto, I. Niki, A. Shvartser, Y. Narukawa, T. Mukai, and A. Scherer, "Surface-plasmon-enhanced light emitters based on InGaN quantum wells," *Nature Materials,* vol. 3, pp. 601-605, 2004.

[71] G. Baffou, R. Quidant, and C. Girard, "Heat generation in plasmonic nanostructures: Influence of morphology," *Applied Physics Letters,* vol. 94, p. 153109, 2009.

[72] S. Mukherjee, F. Libisch, N. Large, O. Neumann, L. V. Brown, J. Cheng, *et al.*, "Hot electrons do the impossible: plasmon-induced dissociation of H2 on Au," *Nano Letters,* vol. 13, pp. 240-247, 2012.

[73] F. Le, D. W. Brandl, Y. A. Urzhumov, H. Wang, J. Kundu, N. J. Halas, *et al.*, "Metallic nanoparticle arrays: a common substrate for both surface-enhanced Raman scattering and surface-enhanced infrared absorption," *ACS nano,* vol. 2, pp. 707-718, 2008.

[74] P. Mulvaney, "Surface plasmon spectroscopy of nanosized metal particles," *Langmuir,* vol. 12, pp. 788-800, 1996.

[75] S. A. Maier, *Plasmonics: fundamentals and applications*: Springer Science & Business Media, 2007.

[76] H. Raether, "Surface plasma oscillations as a tool for surface examinations," *Surface Science,* vol. 8, pp. 233-246, 1967.

[77] E. Kretschmann and H. Raether, "Notizen: radiative decay of non radiative surface plasmons excited by light," *Zeitschrift für Naturforschung A,* vol. 23, pp. 2135-2136, 1968.

[78] A. Otto, "Excitation of nonradiative surface plasma waves in silver by the method of frustrated total reflection," *Zeitschrift für Physik,* vol. 216, pp. 398-410, 1968.

[79] X. Li, D. Xiao, and Z. Zhang, "Landau damping of quantum plasmons in metal nanostructures," *New Journal of Physics,* vol. 15, p. 023011, 2013.

[80] K. Kliewer and R. Fuchs, "Collective electronic motion in a metallic slab," *Physical Review,* vol. 153, p. 498, 1967.

[81] E. A. Stern, "Plasma radiation by rough surfaces," *Physical Review Letters,* vol. 19, p. 1321, 1967.

[82] K. A. Willets and R. P. Van Duyne, "Localized surface plasmon resonance spectroscopy and sensing," *Annu. Rev. Phys. Chem.,* vol. 58, pp. 267-297, 2007.

[83] J. K. Jain and P. B. Allen, "Predicted Raman intensities for bulk and surface plasmons of a layered electron gas," *Physical Review Letters,* vol. 54, p. 947, 1985.

[84] X. Lu, M. Rycenga, S. E. Skrabalak, B. Wiley, and Y. Xia, "Chemical synthesis of novel plasmonic nanoparticles," *Annual Review of Physical Chemistry,* vol. 60, pp. 167-192, 2009.

[85] L. M. Liz-Marzán, "Tailoring surface plasmons through the morphology and assembly of metal nanoparticles," *Langmuir,* vol. 22, pp. 32-41, 2006.

[86] K. M. Mayer and J. H. Hafner, "Localized surface plasmon resonance sensors," *Chem. Rev.,* vol. 111, pp. 3828-3857, 2011.

[87] J. N. Anker, W. P. Hall, O. Lyandres, N. C. Shah, J. Zhao, and R. P. Van Duyne, "Biosensing with plasmonic nanosensors," *Nature Materials,* vol. 7, pp. 442-453, 2008.

[88] A. J. Haes and R. P. Van Duyne, "A unified view of propagating and localized surface plasmon resonance biosensors," *Analytical and Bioanalytical Chemistry,* vol. 379, pp. 920-930, 2004.

[89] S. A. Maier and H. A. Atwater, "Plasmonics: Localization and guiding of electromagnetic energy in metal/dielectric structures," *Journal of Applied Physics,* vol. 98, p. 10, 2005.

[90] K. L. Kelly, E. Coronado, L. L. Zhao, and G. C. Schatz, "The optical properties of metal nanoparticles: the influence of size, shape, and dielectric environment," *Journal of Physical Chemistry B-Condensed Phase,* vol. 107, pp. 668-677, 2003.

[91] K. Catchpole and A. Polman, "Plasmonic solar cells," *Optics Express,* vol. 16, pp. 21793-21800, 2008.

[92] G. A. Ozin, A. C. Arsenault, and L. Cademartiri, *Nanochemistry: a chemical approach to nanomaterials*: Royal Society of Chemistry, 2009.

[93] J. Pérez-Juste, I. Pastoriza-Santos, L. M. Liz-Marzán, and P. Mulvaney, "Gold nanorods: synthesis, characterization and applications," *Coordination Chemistry Reviews,* vol. 249, pp. 1870-1901, 2005.

[94] L. Genzel, T. Martin, and U. Kreibig, "Dielectric function and plasma resonances of small metal particles," *Zeitschrift für Physik B Condensed Matter,* vol. 21, pp. 339-346, 1975.

[95] S. Link and M. A. El-Sayed, "Spectral properties and relaxation dynamics of surface plasmon electronic oscillations in gold and silver nanodots and nanorods," ed: ACS Publications, 1999.

[96] M. Hu, J. Chen, Z.-Y. Li, L. Au, G. V. Hartland, X. Li*, et al.*, "Gold nanostructures: engineering their plasmonic properties for biomedical applications," *Chemical Society Reviews,* vol. 35, pp. 1084-1094, 2006.

[97] R. T. Tung, *et al.*,"The physics and chemistry of the Schottky barrier height," *Applied Physics Reviews,* vol. 1, p. 011304, 2014.

[98] D. A. Neaman, *Semiconductor physics and devices*: Irwin Chicago, 1992.

[99] N. Dasgupta and A. Dasgupta, *Semiconductor devices: modelling and technology*: PHI Learning Pvt. Ltd., 2004.

[100] A. Einstein, "The photoelectric effect," *Ann. Phys,* vol. 17, p. 4, 1905.

[101] C. Kittel, *Introduction to solid state* vol. 162: John Wiley & Sons, 1966.

[102] H. S. Kojori, S. Cho, R. Han, J.-H. Yun, J. Kim, and S. J. Kim, "Efficient hot electron collection, detection, and amplification in plasmon field-effect transistor," *Journal of Photonics for Energy,* vol. 6, pp. 042509-042509, 2016.

[103] V. L. Dalal, "Simple model for internal photoemission," *Journal of Applied Physics,* vol. 42, pp. 2274-2279, 1971.

[104] J. M. Mooney and J. Silverman, "The theory of hot-electron photoemission in Schottky-barrier IR detectors," *IEEE Transactions on Electron Devices,* vol. 32, pp. 33-39, 1985.

[105] S. J. Kim and J. Yun, "Plasmon field effect transistor," ed: Google Patents, 2016.

[106] H. Shokri Kojori, J.-H. Yun, Y. Paik, J. Kim, W. A. Anderson, and S. J. Kim, "Plasmon field effect transistor for plasmon to electric conversion and amplification," *Nano Letters,* vol. 16, pp. 250-254, 2015.

[107] Y. Taur and T. H. Ning, *Fundamentals of modern VLSI devices*: Cambridge University Press, 2013.

[108] S. M. Sze, *Semiconductor devices: physics and technology*: John Wiley & Sons, 2008.

[109] J. Wu, G. Xu, and J. Liu, "Plasmonic Graphene and Method of Making the Same," ed: Google Patents, 2012.

[110] J. Lin, H. Li, H. Zhang, and W. Chen, "Plasmonic enhancement of photocurrent in MoS2 field-effect-transistor," *Applied Physics Letters,* vol. 102, p. 203109, 2013.

[111] Microchem, *Spin speed curves for PMMA and copolymer resists*: ed, 2001.

[112] K. Brown and G. Tautfest, "Faraday-Cup Monitors for High-Energy Electron Beams," *Review of Scientific Instruments,* vol. 27, pp. 696-702, 1956.

[113] D. M. Sullivan, *Electromagnetic simulation using the FDTD method*: John Wiley & Sons, 2013.

[114] A. Manjavacas, J. G. Liu, V. Kulkarni, and P. Nordlander, "Plasmon-Induced Hot Carriers in Metallic Nanoparticles," *ACS Nano,* vol. 8, pp. 7630-7638, 2014/08/26 2014.

[115] C. Clavero, "Plasmon-induced hot-electron generation at nanoparticle/metal-oxide interfaces for photovoltaic and photocatalytic devices," *Nature Photonics,* vol. 8, pp. 95-103, 2014.

[116] P. K. Maharana, P. Padhy, and R. Jha, "On the field enhancement and performance of an ultra-stable SPR biosensor based on graphene," *IEEE Photonics Technology Letters,* vol. 25, pp. 2156-2159, 2013.